Journal of Nanomaterials

Advanced Nano/Microporous Materials for Energy Storage

Lead Guest Editor: Sami-Ullah Rather
Guest Editors: Jijeesh Ravi Nair and Faheem A Sheikh

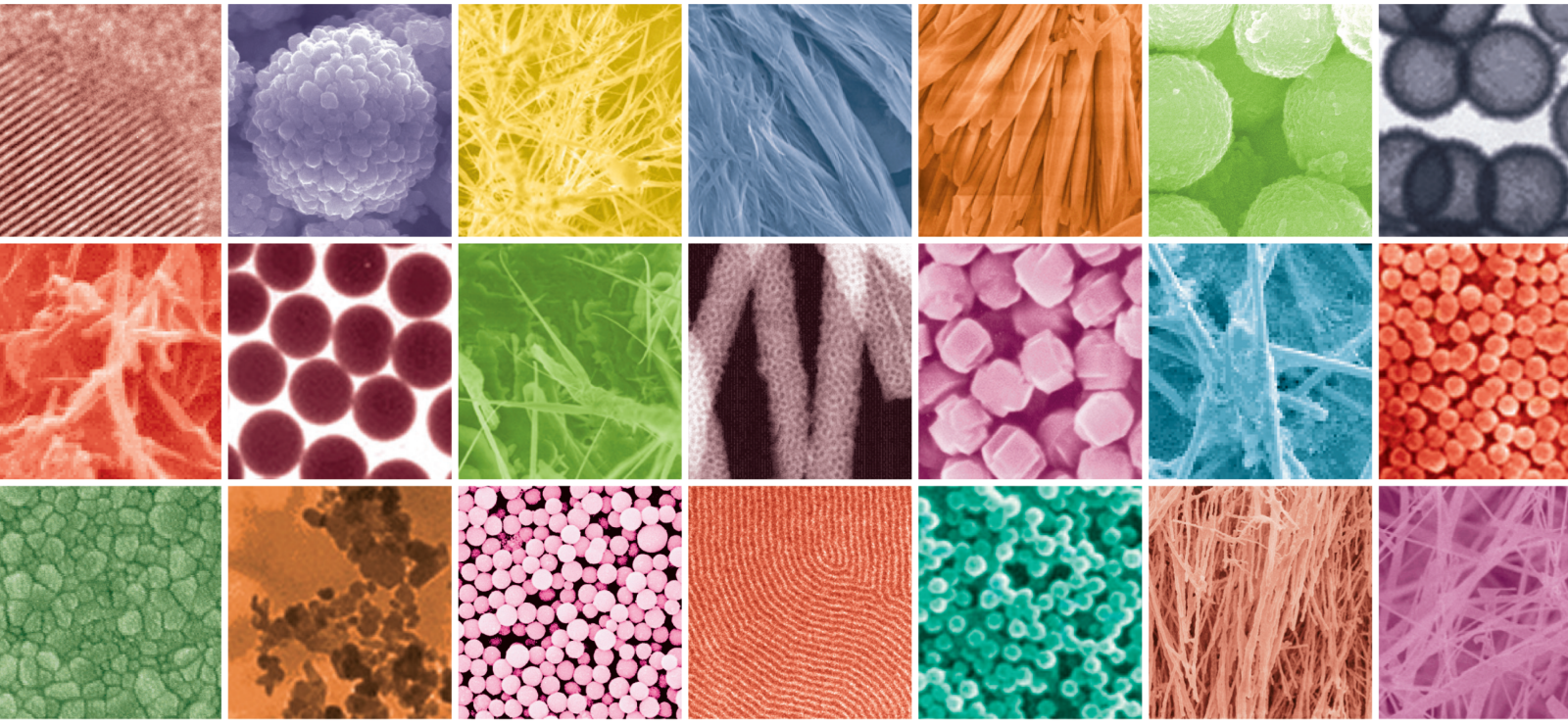

Advanced Nano/Microporous Materials for Energy Storage

Journal of Nanomaterials

Advanced Nano/Microporous Materials for Energy Storage

Lead Guest Editor: Sami-Ullah Rather
Guest Editors: Jijeesh Ravi Nair and Faheem A Sheikh

Contents

Hindawi
Journal of Nanomaterials
Volume 2022, Article ID 8739993, 17 pages
https://doi.org/10.1155/2022/8739993

Research Article

Sequential and/or Simultaneous Wet-Impregnation Impact on the Mesoporous Pt/Sn/Zn/γ-Al_2O_3 Catalysts for the Direct Ethane Dehydrogenation

Arshid M. Ali, Abdulrahim A. Zahrani, Muhammad A. Daous, Seetharamulu Podila, Majid Khalid Alshehri, Sami-ullah Rather, and Usman Saeed

Department of Chemical and Materials Engineering, Faculty of Engineering, King Abdulaziz University, Jeddah, Saudi Arabia

Correspondence should be addressed to Arshid M. Ali; arshid.mahmood.ali@gmail.com
and Sami-ullah Rather; rathersami@kau.edu.sa

Received 27 September 2021; Revised 6 January 2022; Accepted 28 January 2022; Published 23 February 2022

Academic Editor: Vincenzo Baglio

This study is aimed at investigating the impact of catalyst preparation's approach (either sequential and/or simultaneous wet impregnation) to a mesoporous series of Pt/A, Sn/A, PtSn/A, SnPt/A, (PtSn)/A, (PtSn)Zn/A, and (PtSnZn)/A catalysts for direct ethane dehydrogenation. The (PtSn)/A and (PtSnZn)/A had shown both higher initial specific activity (s^{-1}) and reaction rate constant K_d (h^{-1}) (13063.86 (s^{-1}) and 12489.69 (s^{-1}) and 0.09 (h^{-1}) and 0.06 (h^{-1})), respectively. The catalyst preparation approach had direct impact to the availability and dispersion of mesoporous particles of either active metal and/or promoter that influences either to hinder the C-C cleavage and/or to promote C-H bond cleavage in the dehydrogenation of ethane to ethene. The active metal component was present in the form of Pt, Pt^{+2}, Al^{+3}, Sn^{+4}, and Zn^{+2} states. The enhanced catalytic activity is attributed to the Pt_4Sn and PtZn formed phases in addition to highly dispersed mesoporous Pt particles. Based on the obtained results, the catalysts prepared by using simultaneous wet impregnation had shown higher catalytic activity and catalyst stability as to that of sequential wet impregnation.

1. Introduction

Ethylene is the main building blocks in process industry, and in the year 2021, its global production has surpassed 200 million tons per annum. The projected forecast of ethenes by the year 2025 is 290 million tons per annum. Olefins are more valuable compound than their predecessors, alkanes such as paraffin and ethane. Therefore, it is of industrial need to convert lower alkanes to respective alkenes. Multiple [1–46] have been reported for converting lower alkanes to their respective alkenes. Technologies like Catofins, fluidized bed reactor (FBD), UOP Oleflex, and STAR are seeking attention for propane dehydrogenation with trade-off reactor designs, catalyst type, regeneration mode, and % yield based on operating reaction temperature and pressure. However, aforementioned technologies are yet struggling to meet higher yield, catalyst stability, and life. Based on available literature, dehydrogenation was studied by using the following two approaches: oxidative and non-oxidative dehydrogenation [6, 12, 21, 25, 42, 47–55]. The low olefin selectivity and the formation of COX are major obstacles in ODH, whereas the NODH attained a better olefin yield. However, due to thermodynamic limitations, both technologies yet need to explore better options to enhance olefin yield with least undesired reaction products at reduced reaction temperature and pressure.

Usually, supported active metal/promoters were used in low alkane dehydrogenation. Based on initial literature assessment and known dehydrogenation literature for C1 to C4 alkanes, platinum [13, 20, 30, 31, 35, 51, 56–58] and chromium [37, 43, 49] are the commonly used catalyst. Each one of them has its own advantages and disadvantages. Pt has superior activation for C-H bond and low tendency towards C-C cleavage. It is highly stable and usually produces higher catalytic activity with low % loading in addition to environment friendly. However, sintering of Pt particles after frequent

Table 1: List of prepared catalyst by using either sequential and/or simultaneous wet impregnation.

Sr #	Catalyst composition	Brief to simultaneous/sequential	Notation
1	γ-Al_2O_3	-	A
2	1%Pt/γ-Al_2O_3	-	Pt/A
3	1%Sn/γ-Al_2O_3	-	Sn/A
4	1%Pt1%Sn/γ-Al_2O_3	*Sequential*: impregnation of Sn to Pt/γ-Al_2O_3 catalyst	PtSn/A
5	1%Sn1%Pt/γ-Al_2O_3	*Sequential*: impregnation of Pt to Sn/γ-Al_2O_3 catalyst	SnPt/A
6	1%Pt1%Sn/γ-Al_2O_3	Simultaneous impregnation of Pt and Sn to γ-Al_2O_3 support	(PtSn)/A
7	1%Pt1%Sn1%Zn/γ-Al_2O_3	*Sequential*: impregnation of Zn to (PtSn)/γ-Al_2O_3 catalyst	(PtSn)Zn/A
8	1%Pt1%Sn1%Zn/γ-Al_2O_3	Simultaneous impregnation of Pt, Sn, and Zn to γ-Al_2O_3 support	(PtSnZn)/A

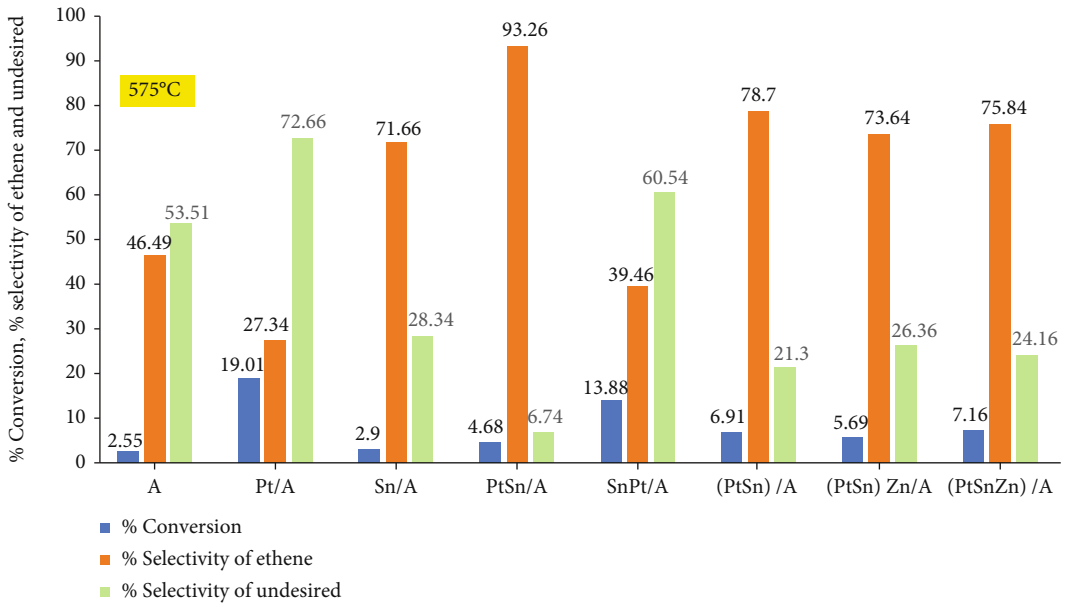

Figure 1: Catalytic activity comparisons of the support A and each of the freshly prepared Pt/A, Sn/A, PtSn/A, SnPt/A, (PtSn)/A, (PtSn)Zn/A, and (PtSnZn)/A catalysts at 575°C.

regeneration cycle can lead to decreased catalyst life, whereas the Cr metal has fair catalytic activity and selectivity dependent on Cr loading. However, Cr-based catalyst losses catalytic activity with each regeneration step due to decreased available surface area. In addition, it is environmentally toxic and has very little catalyst life in comparison to Pt metal. Therefore, many scientists and few commercial research and development organisation are yet inclined to use Pt as active metal for an efficient dehydrogenation catalyst for lower alkanes. In addition to active metal, the type and nature of the support of supported catalysts also played an important role. A crystalline framework arrangement with high surface area and uniform channel size is of acute importance. Based on available literature, the Pt-supported catalyst is preferred to meet current challenges of NODH.

Other than the selection of the best support, key aspect is to allow and/or control the formation of favorable phases of bi or multicomponent in the catalyst recipe. To address it, the catalyst preparation approach could play an important role to achieve the presence of more active phases. As of best knowledge of the authors, a very little scientific information on the comparison of the catalyst preparation approach such as sequential and/or simultaneous wet impregnation is available especially Pt-supported catalyst for NODH. Therefore, this study is aimed at preparing and comparing the catalytic activities of a methodologically prepared series of the catalysts (see Table 1) using either sequential and/or simultaneous wet impregnation. This approached has never been reported for lower alkane direct dehydrogenation. Such study shall shed an insight to the active metal dispersion and impact of preparation approach to form active phase between mono and/or binary active metal components.

2. Materials and Methods

The used chloride salts of platinum, tin, magnesium, calcium, and zinc were procured from Sigma-Aldrich. The list of used chemicals was Platinum(II) chloride (≥99.9% trace metals basis), Tin(II) chloride reagent grade (98%), Zinc chloride (99.999% trace metals basis), and deionized water. The catalyst support, γ-Al_2O_3 (SS-200), was obtained from BASF chemicals.

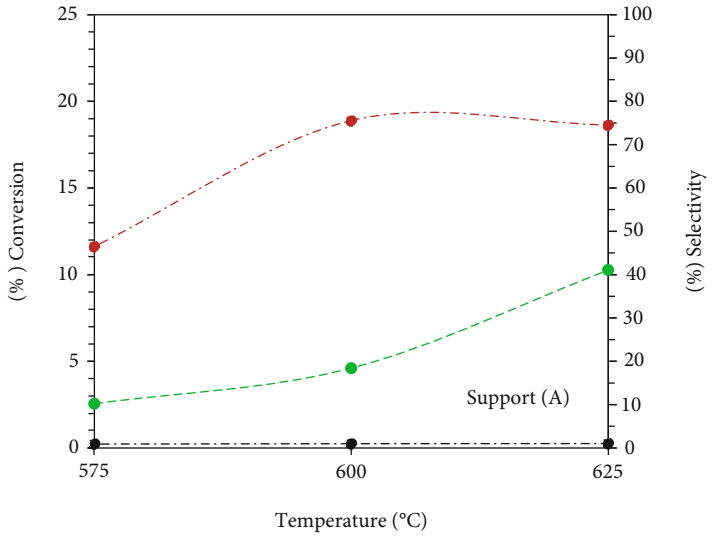

(a)

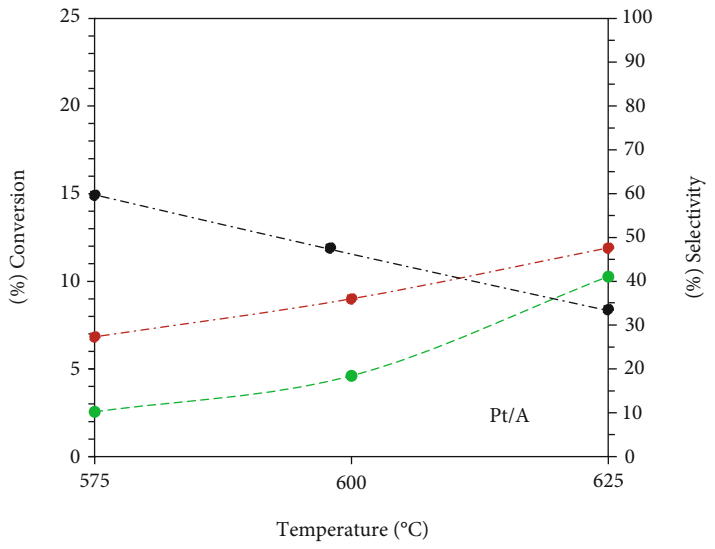

(b)

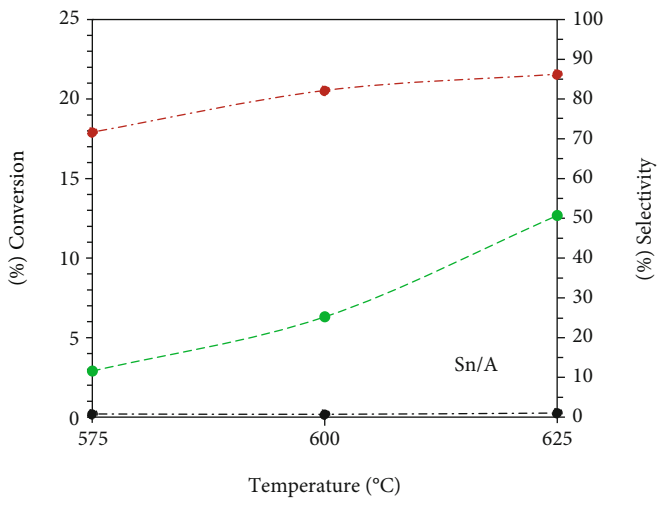

(c)

Figure 2: Continued.

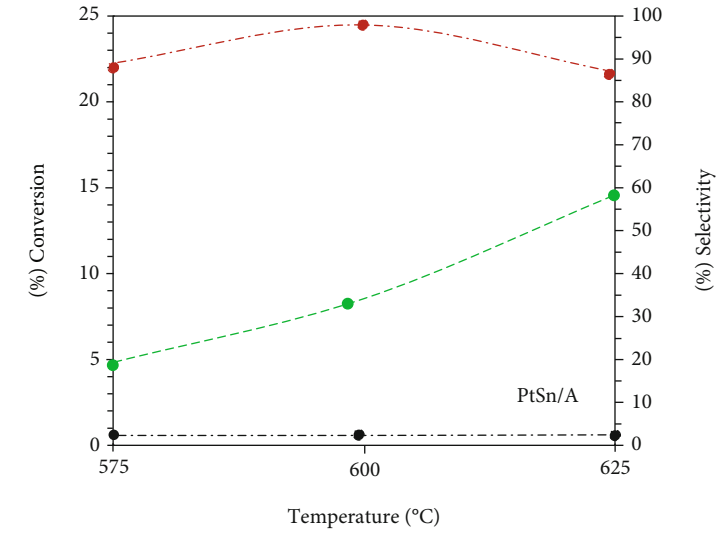

(d)

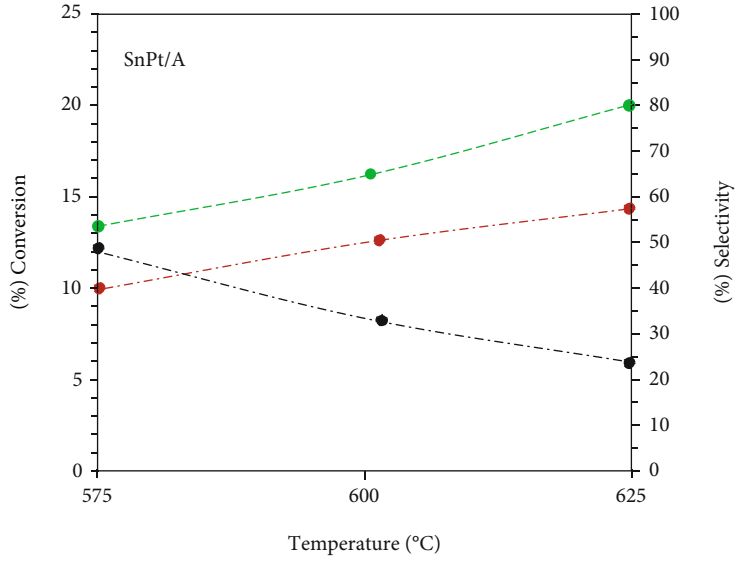

(e)

Figure 2: Continued.

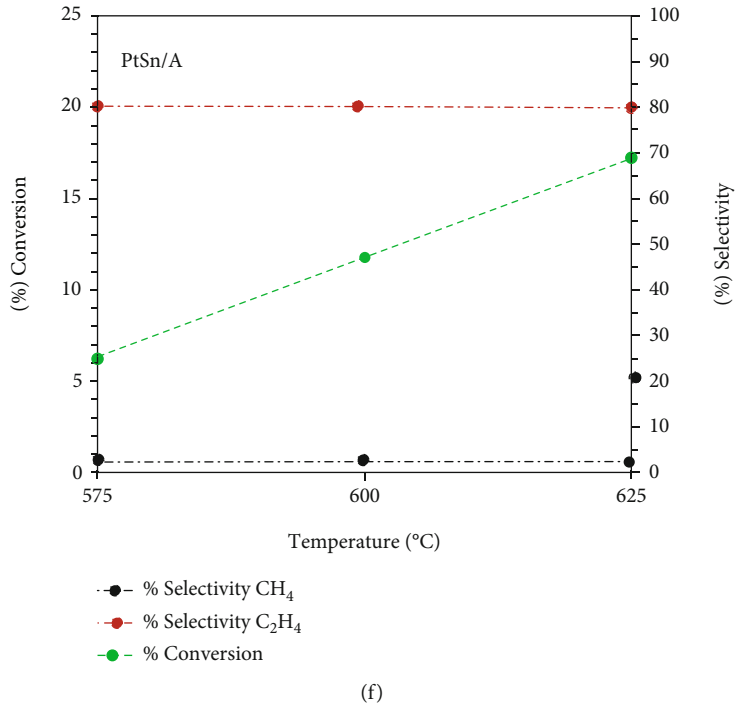

Figure 2: Effect of reaction temperature to the catalytic activity of the support A, Pt/A, Sn/A, PtSn/A, SnPt/A, and (PtSn)/A catalysts.

2.1. Catalyst Preparation. The catalyst support γ-Al_2O_3 pallets were crushed to sieve size of 300–600 mesh size by using the grinder (ERWEKA AR 402, TG2000) and were calcined at 650°C for 6 hours under static air. All the catalysts were prepared by using wet impregnation at 85°C for 5 hours. A precise amount of well-dried catalyst support and 1% active metal precursor stock solution were added to rotary evaporator to prepare a series of the catalyst by using sequential and/or simultaneous approach (see Table 1). The impregnated sludge was dried in a digitally controlled vacuum dryer at 110°C for 4 hours. The dried impregnated sludge was multiply rinsed with deionized water to remove any chloride residues. Finally, it was calcined for a time of 6 hours at 650°C under flowing air (100 ml/min) using a tube furnace. The calcined catalyst samples were converted into small tablets by using tablet press machine. At the end, the catalyst tablet was crushed to particle size of 125-250 μm.

2.2. Catalytic Activity. The catalytic activity of freshly prepared catalysts was tested in a PID Microactivity reactor (PID ENG & TECH) coupled with online gas chromatography (GC; 7890B-Agilent) containing both flame ionization and thermal conductivity detectors (FID and TCD). Both safety and absence of any leaks in PID Microactivity reactors were tested by using an inert gas nitrogen with a flow rate of 8.8 ml/min for 1 hour at 600°C. Before the catalytic run, the catalyst was reduced at 600°C. After the catalyst reduction, N_2 was used to purge any traces of unwanted gas/media. 0.5 g of reduced catalyst as loaded to the reactor and the catalytic activity of each catalyst was tested at three different temperatures 575°C, 600°C, and 625°C under flow rate of in the ratio of $N_2 : H_2 : C_2H_6 = 3 : 1 : 1$. The catalytic activity at each temperature is monitored and recorded for 2 hrs. The total reaction time was 6.7 hours. Throughout the reaction, the extent of conversion of ethane to ethylene and/or other unwanted products was measured by using GC.

2.3. Catalyst Characterization. Micrometer NOVA 2200e analyzer was used to measure the BET surface area and pore distribution by using N_2-physiosorption method. X-ray diffraction (XRD) was used to study the crystalline phase of both unused and used catalyst at 25°C with 2θ range of 20–120°C by using Equinox 1000 equipped with Co-kα radiation. A SPECS GmbH X-ray photoelectron spectroscopy was used to identify the oxidation states of the active metal by using dual nonmonochromatic X-ray source Al-Kα under 13.5 kV, 150 Watts of X-ray power. H_2-temperature programmed reduction was used to analyze the redox behavior of 0.6 g of spent catalyst from room temperature to 875°C with 15 ml/min flow of 5% H_2/N_2 gas. Quantachrome pulsar automatic chemisorption analyzer equipped with ThermoStar TM GSD 320 quad core mass spectrometer was used to study the NH_3-temperature programmed desorption for acid-base behavior and dispersion of active metal.

3. Results and Discussions

3.1. Catalytic Activity. PID Microactivity reactor was used to study the catalytic activity of the support A and each of the freshly prepared Pt/A, Sn/A, PtSn/A, SnPt/A, (PtSn)/A, (PtSn)Zn/A, and (PtSnZn)/A catalysts. The % conversion, % selectivity of ethene, and undesired reaction products obtained at 575°C are shown in Figure 1. For the reported value of catalytic activity, selectivity is the average of the values obtained during 2 hrs reaction with standard deviation of 0.01%.

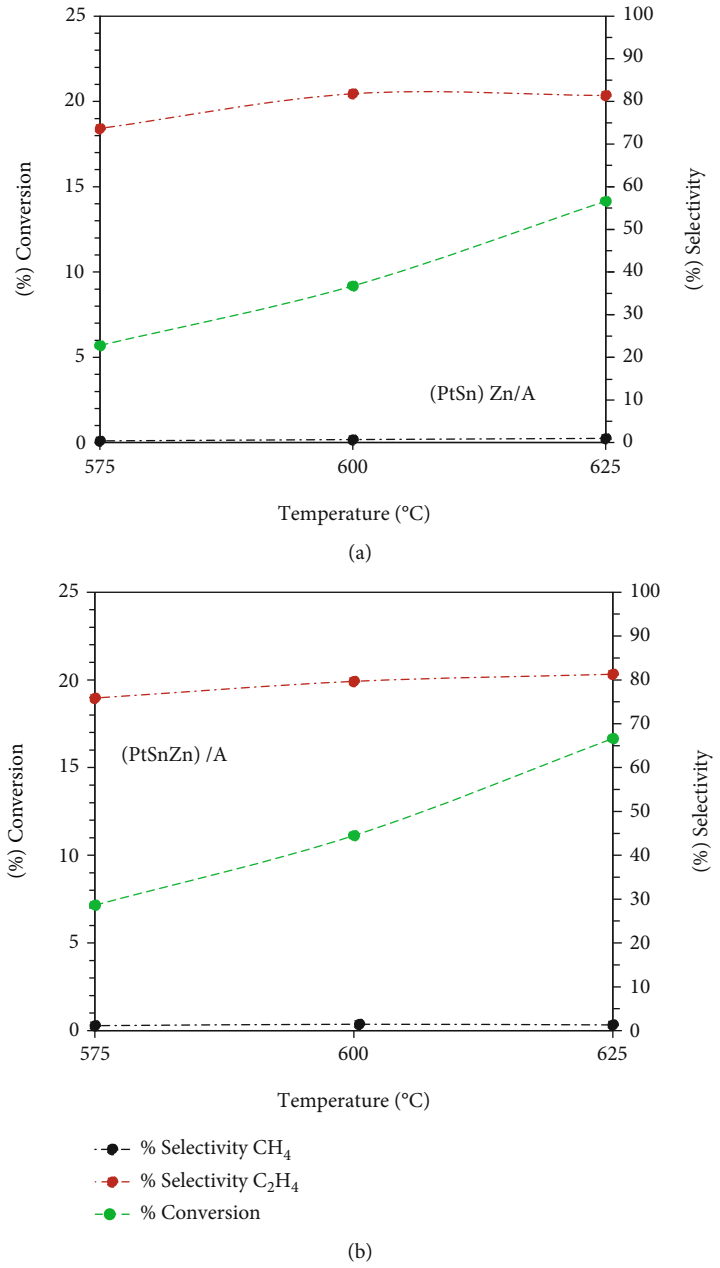

Figure 3: Effect of reaction temperature to the catalytic activity of the (PtSn)Zn/A and (PtSnZn)/A catalysts.

In the case of the catalyst support A, the % conversion of ethane, % selectivity of ethene, and % selectivity of the undesired reaction product were 2.55%, 46.49%, and 53.51%, respectively. Overall, the % selectivity of undesired reaction product is slightly higher as to that of % selectivity of desired product (ethene) with very little % conversion of ethane to ethene.

The Pt/A catalyst had shown 19.01% conversion, 27.34% ethene selectivity, and 72.66% selectivity of undesired reaction product. Overall, the Pt/A catalyst was more active as to that of the support A. However, it has shown very high % selectivity of undesired reaction products due to the Pt attack on C-C bond [59]. This led to higher cracking of ethane to methane and coke formation.

The Sn/A catalysts had shown 2.9% conversion, 71.66% ethene selectivity, and 28.34% selectivity of undesired reaction product. Overall, the Sn/A catalyst had shown lower % conversion in comparison to Pt/A catalyst. However, the Sn/A catalyst had shown reduced formation of undesired reaction products. This is because of the least ability of Sn in the catalyst composition to break C-C bonds and/or cracking [31]. In addition, the Sn has significantly assisted to reduce the acidic nature of the support [60].

The PtSn/A had shown 4.68% conversion of ethane with ethene % selectivity of 93.26% and 6.74% of undesired product selectivity. The PtSn/A catalyst had shown increased % conversion in comparison to the support and Sn/A catalyst. Also, the PtSn/A catalyst has shown the highest % selectivity

Table 2: A comparison of % conversion, % selectivity, and % yield of desired reaction product (ethene) at 575°C, 600°C, and 625°C.

Catalyst	% conversion Temperature (°C)			% selectivity Temperature (°C)			% yield Temperature (°C)		
	575	600	625	575	600	625	575	600	625
A	2.55	4.61	10.27	46.49	75.53	74.52	1.19	3.48	7.65
Pt/A	19.01	22.63	24.96	27.34	36.01	47.63	5.20	8.15	11.89
Sn/A	2.9	6.31	12.68	71.66	82.14	86.24	2.08	5.18	10.94
PtSn/A	4.68	7.73	12.69	93.26	98.5	92.12	4.36	7.61	11.69
SnPt/A	13.88	17.07	21.61	39.46	51.41	60.05	5.48	8.78	12.98
(PtSn)/A	6.91	11.78	16.63	78.7	78.60	78.26	5.44	9.26	13.01
(PtSn)Zn/A	5.69	9.18	14.15	73.64	81.81	81.39	4.19	7.51	11.52
(PtSnZn)/A	7.16	11.13	16.66	75.84	79.67	81.31	5.43	8.87	13.55

Table 3: Comparison of % metal, Pt/Sn and Pt/Zn ratio, % conversion, % selectivity, % yield, initial specific activity (s^{-1}), and reaction rate constant K_d (h^{-1}) for the reaction carried at 600°C.

Catalyst	Pt (% wt)	Sn (% wt)	Zn (% wt)	Pt/Sn	Pt/Zn	Conv. (%)	Sel. (%)	Yield (%)	Initial specific activity (s^{-1})	Reaction rate constant K_d (h^{-1})
(PtSn)/A	0.54	1.68	-	0.32	-	11.78	78.60	9.26	13063.86	0.09
(PtSnZn)/A	0.48	1.78	0.81	0.27	0.59	9.04	79.67	8.87	12489.69	0.06

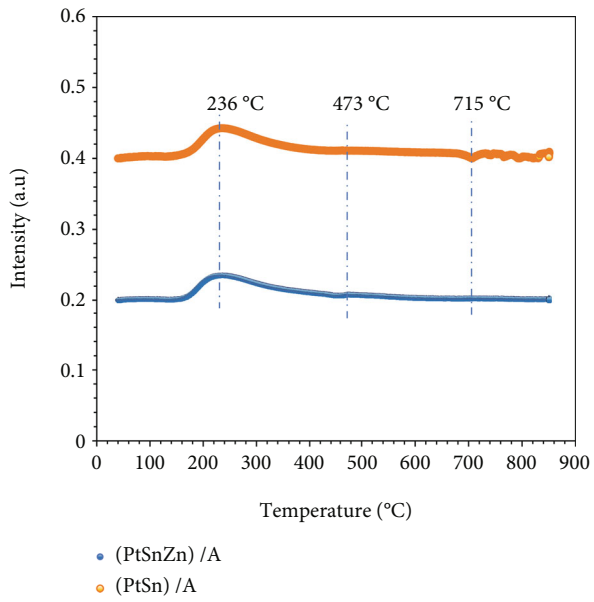

Figure 4: TPR analysis comparison between (PtSn)/A and (PtSnZn)/A catalyst.

of ethene in addition to least % selectivity of undesired reaction products. However, the % conversion of PtSn/A is lower than that of the Pt/A. This is because of the presence of Pt with Sn had reduced affinity to C-C bond—clear from the least % selectivity of undesired reaction product CH_4 (which can be only formed from the C-C bond cleavage in ethane molecule) [31, 60]. Overall, the PtSn/A has the highest % selectivity of ethene with least % selectivity of undesired reaction products.

The SnPt/A had shown 13.88% conversion of ethane to ethene with % selectivity of 39.46% and 60.54% of undesired product selectivity. In comparison, the SnPt/A catalyst had shown higher % conversion of ethane and % selectivity of undesired reaction products as to that of PtSn/A catalyst. This is because of highly dispersed mesoporous Pt particles at the outer surface of unhomogenized catalyst due to the sequential wet impregnation of Pt to Sn/A catalyst to obtain SnPt/A catalyst. The availability of highly dispersed mesoporous Pt in the unhomogenized catalyst led to the enhanced % conversion due to C-C cleavage rather due to C-H cleavage, mandatory for dehydrogenation of ethane [9, 34, 35, 37, 58, 59].

The (PtSn)/A catalyst exhibited 6.91% conversion of ethane, with ethene % selectivity of 78.7% and 21.3% of undesired product selectivity. The % of undesired reaction products, in the case of (PtSn)/A catalyst, was less than SnPt/A catalyst and higher as to that of PtSn/A catalyst. The (PtSn)/A, prepared by simultaneous wet impregnation of both Pt and Sn on the support A, has generated a better alloy between Pt and Sn due to which the individual impact of either Pt and/or Sn was reduced [33, 56]. That is why, the % conversion of (PtSn)/A is less as to that of either PtSn/A or SnPt/A due to trade of between cracking/C-C bond cleavage and the dehydrogenation.

The (PtSn)Zn/A catalyst exhibited 5.69% conversion of ethane, with ethene % selectivity of 73.64% and 26.36% of undesired product selectivity. These results showed that sequential addition of Zn to (PtSn)/A catalyst had not impacted much to the acidity of the catalyst support A due to which the (PtSn)Zn/A had shown lower % conversion as to that of (PtSn)/A catalyst. In parallel, the addition of the Zn to (PtSn)/A catalyst also led to the decreased C-C cleavage/cracking with enhanced dehydrogenation extent [37].

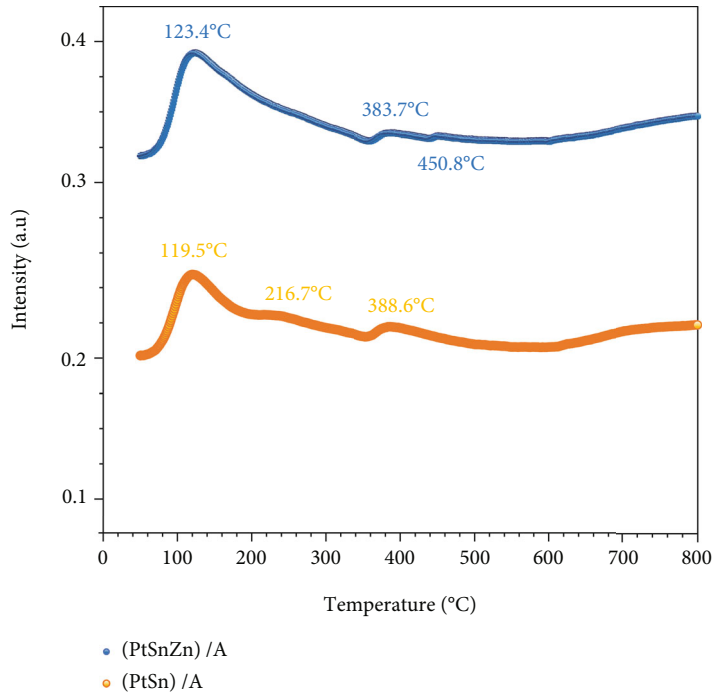

Figure 5: NH_3-TPD study comparison of (PtSn)/A and (PtSnZn)/A catalyst.

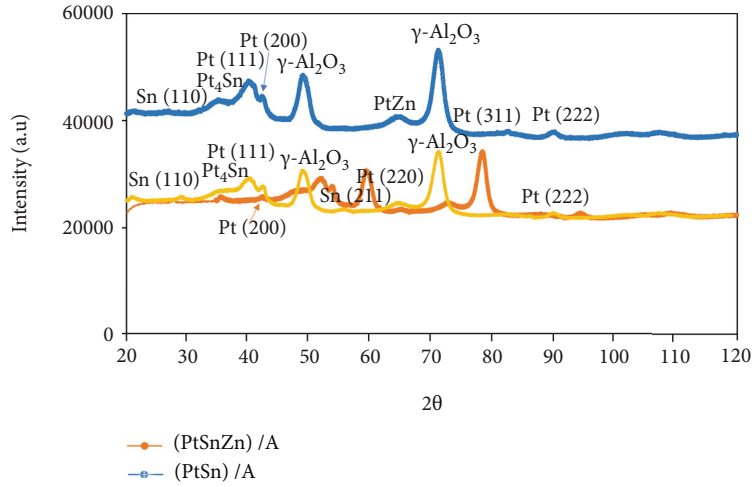

Figure 6: Comparison of XRD analysis of (PtSn)/A and (PtSnZn)/A catalysts.

Due to the favorable impact of Zn to (PtSn)/A catalyst, it was thought to prepare a (PtSnZn)/A catalyst by using the simultaneous impregnation of Pt, Sn, and Zn to the catalyst support. The (PtSnZn)/A catalyst exhibited 7.16% conversion of ethane, with ethene % selectivity of 75.84% and 24.16% of undesired product selectivity. The overall catalytic activity (in terms of % conversion, % selectivity of ethene, and undesired reaction products) of the (PtSnZn)/A catalyst is higher as to that of the (PtSn)Zn/A catalyst. This is clearly due to enhanced beneficial impacts of the simultaneous impregnation of Zn with Pt and Sn to the catalyst support which led to much better homogenized catalyst with better Pt-Sn/Sn-Zn/Pt-Zn alloy formation [31, 37, 60]. In addition, this catalyst preparation approach [2] led to significant decrease in C-C cleavage/cracking with higher dehydrogenation extent.

In general, the catalytic activity in terms of % conversion, % selectivity of ethene, and undesired reaction products is different either due to catalyst composition and/or catalyst preparation approach (sequential and/or simultaneous) within the single catalyst preparation method (wet impregnation).

3.2. Effect of Reaction Temperature. The effect of reaction temperature plays a significant role either to overall catalytic activity and/or stability of the catalyst. Therefore, the catalytic activity (in terms of % conversion, % selectivity of ethene, and undesired reaction product (ethane)) of all the

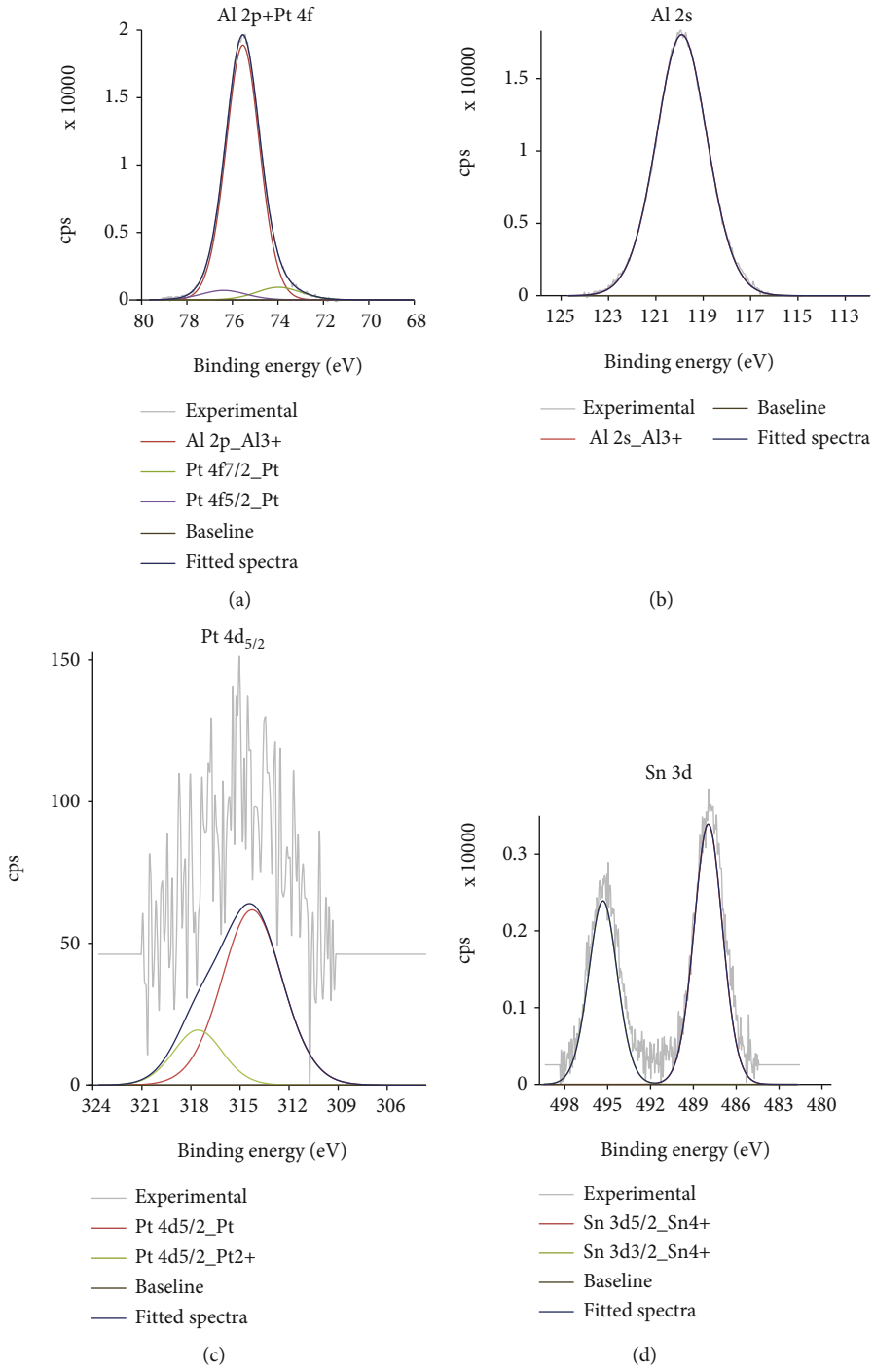

Figure 7: Continued.

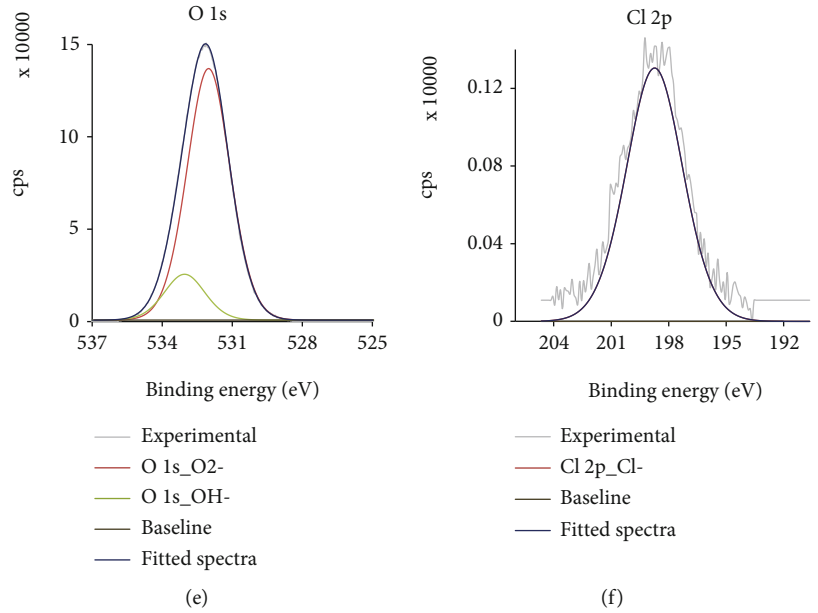

Figure 7: XPS analysis of (PtSn)/A. (a) The deconvoluted spectra of Al 2p+Pt4f. (b) The deconvoluted spectra of Al 2s. (c) The deconvoluted spectra of Pt 4d. (d) The deconvoluted spectra of Sn 3d. (e) The deconvoluted spectra of O 1s. (f) The deconvoluted spectra of Cl 2p.

catalysts was studied at three different reaction temperatures 575°C, 600°C, and 625°C. The effect of each reaction temperature is shown in Figures 2 and 3.

In general, % conversion increased with the increase in temperature for all the catalysts. However, the % selectivity of desired and undesired reaction product varies with the catalyst composition. For instance, the % selectivity of undesired reaction product (methane) at each studied reaction temperature (575°C, 600°C, and 625°C) was nearly remained constant for the support A and Sn/A, PtSn/A, (PtSn)/A, (PtSn)Zn/A, and (PtSnZn)/A catalysts (see Figures 2(a), 2(c), 2(d), 2(f), 3(a), and 3(b)). However, in the case of the Pt/A and SnPt/A catalysts, the % selectivity of methane (undesired reaction product) gradually decreased with the increase in reaction temperature (see Figures 2(b), 2(e), and 3(a)). This could be due to the freely available Pt mesoporous particles because it is well established that Pt has higher tendency to C-C bond cleavage [9, 34, 35, 37, 58, 59]. In other words, it is the least formation of potential active alloy phase(s) between Pt and Sn in the case of SnPt/A catalyst. Therefore, the catalyst preparation approach either sequential and/or simultaneous wet impregnation has direct influence to hinder the C-C and/or C-H bond cleavage in dehydrogenation.

In terms of % selectivity of the desired reaction product (ethane), it increased with the increase in reaction temperature for all the studied catalysts except the PtSn/A and (PtSn)/A catalysts. In the case of PtSn/A, the % selectivity of ethene first increases with the increase in the reaction temperature from 575°C to 600°C and then it decreased with the further reaction temperature increase from 600°C to 625°C (see Figure 2(d)), whereas in the case of the (PtSn)/A catalyst, the % selectivity of ethene remained almost constant with the increase in reaction temperature from 575°C to 625°C (see Figure 2(f)). In all other studied Pt/A, Sn/A, SnPt/A, (PtSn)Zn/A, and (PtSnZn)/A catalysts, the % selectivity of ethene increased with the increase in reaction temperature (see Figures 2(b), 2(c), 2(e), 3(a), and 3(b)). However, the extent of the increased % selectivity of ethane is different in each catalyst composition.

An overall comparison of % conversion, % selectivity, and % yield of desired reaction product (ethene) at 575°C, 600°C, and 625°C temperature is shown in Table 2. Among all the studied catalysts, the (PtSn)/A and (PtSnZn)/A showed maximum % yield of desired reaction product (ethene) at 575°C, 600°C, and 625°C, respectively. Both catalysts were prepared by using simultaneous wet impregnation.

Based on abovementioned findings, the initial specific activity (s^{-1}) and reaction rate constant K_d (h^{-1}) of the best (PtSn)/A and (PtSnZn)/A were calculated by using the following:

$$\text{Initial specific activity } \left(s^{-1}\right) = \frac{[\text{moles of the product/moles of Pt}]}{\text{time}},$$
$$\text{Reaction rate constant } K_d \left(h^{-1}\right) = \frac{[\ln(1 - x_{\text{end}})/x_{\text{end}}) - \ln(1 - x_{\text{start}})/x_{\text{start}})]}{\text{time}}, \quad (1)$$

where x_{end} and x_{start} are the conversion at the start and end of the reaction.

The summary of the results is shown in Table 3. In general, the catalyst preparation approach, either sequential and/or simultaneous wet impregnation, has direct link to the enhanced % selectivity and/or % yield of desired reaction product.

3.3. TPR Analysis. The TPR analysis is very useful to study the interaction of active metal with support and/or promoter. Based on the highest catalytic activity, in terms of

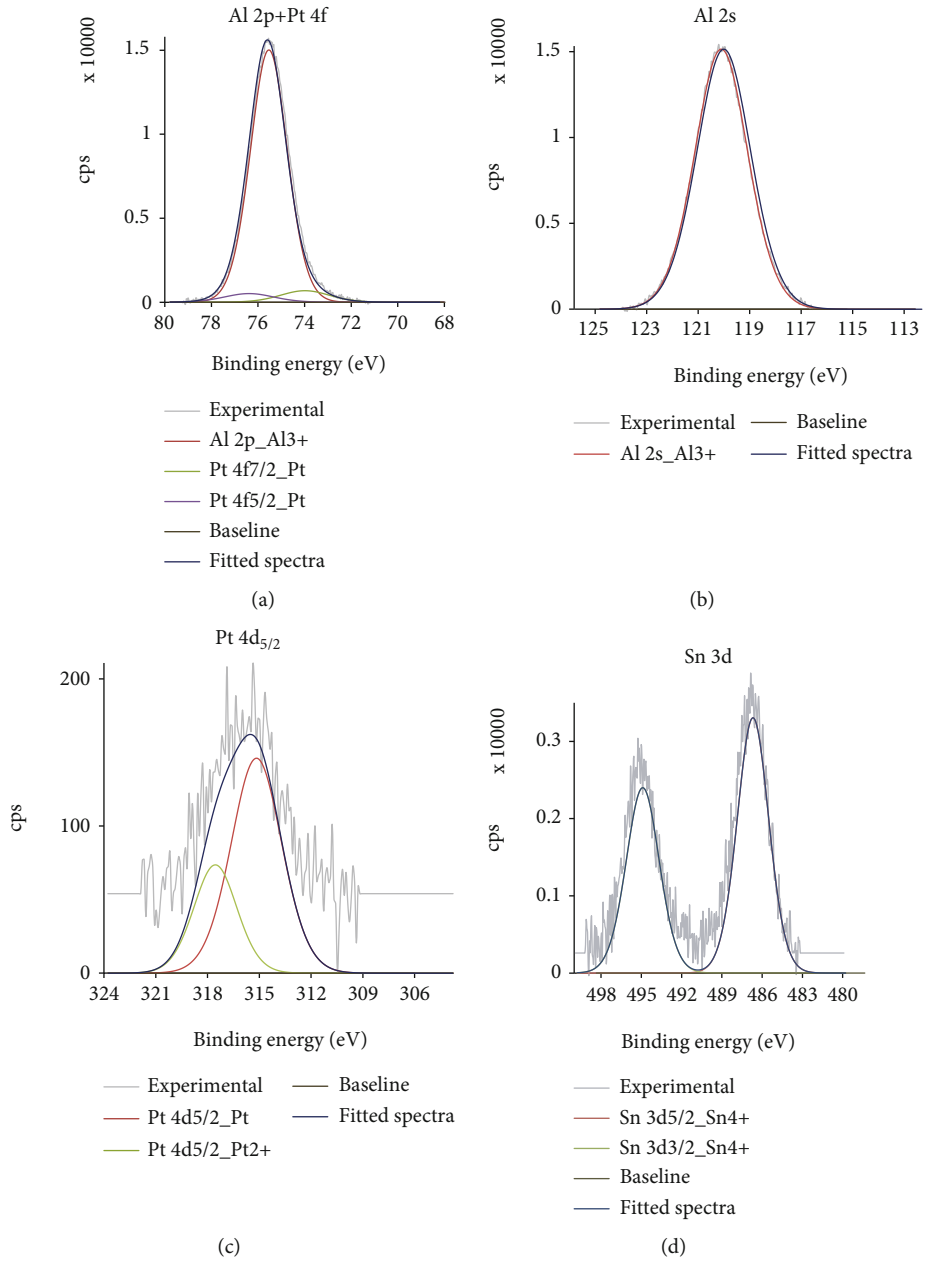

Figure 8: Continued.

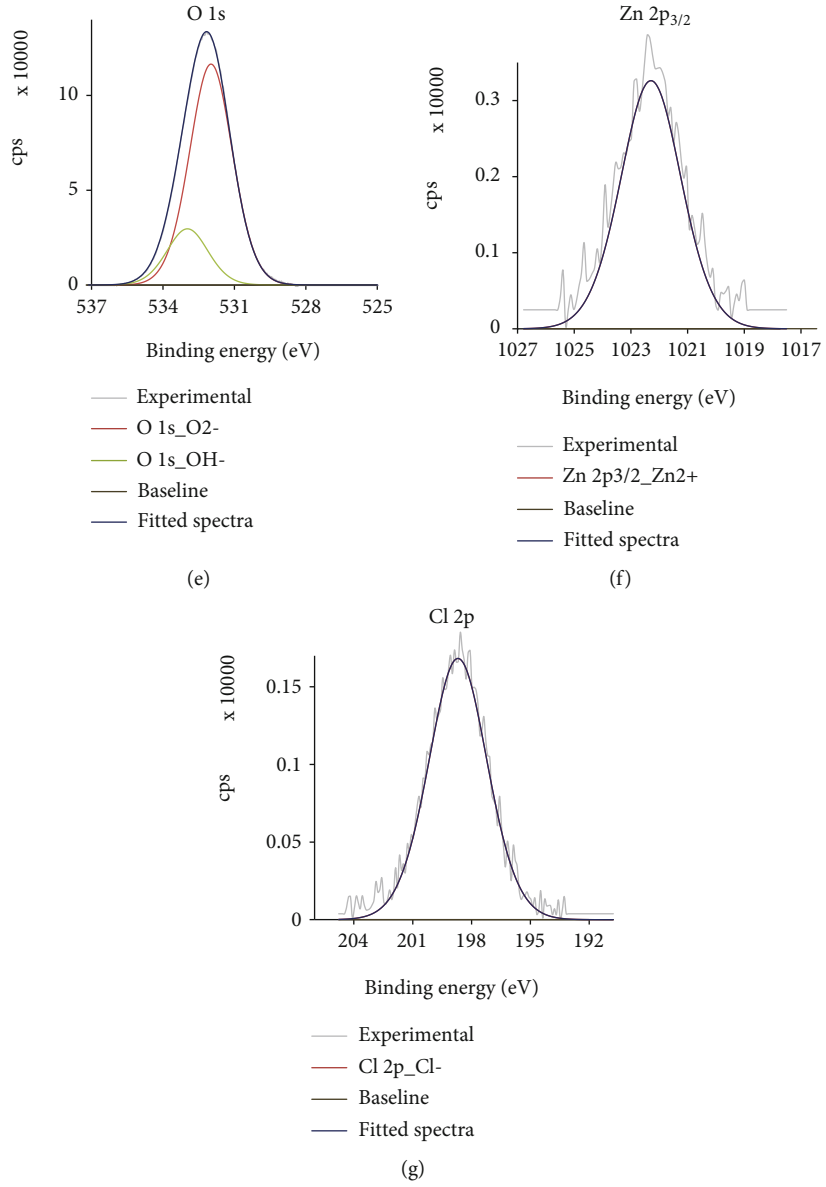

Figure 8: XPS analysis of (PtSnZn)/A. (a) The deconvoluted spectra of Al 2p+Pt4f. (b) The deconvoluted spectra of Al 2s. (c) The deconvoluted spectra of Pt 4d. (d) The deconvoluted spectra of Sn 3d. (e) The deconvoluted spectra of O 1s. (f) The deconvoluted spectra of Zn 2p. (g) The deconvoluted spectra of Cl 2p.

initial specific activity and reaction rate constant, the best (PtSn)/A and (PtSnZn)/A catalysts were analyzed by using TPR technique. The obtained results are shown in Figure 4. The (PtSn)/A catalyst exhibited comparatively intense and broader Pt peak at 236°C as to that of (PtSnZn)A catalyst at the same temperature. This peak belonged to Pt [61]. The slightly higher intensity of Pt peak, in (PtSn)/A catalyst, showed that it required more H_2 consumption to reduce Pt-O surface as to that of (PtSnZn)/A. This showed that dispersion of Pt mesoporous particles in (PtSn)/A catalyst is higher in comparison to (PtSnZn)/A catalyst. Due to better dispersion of Pt mesoporous particles, the (PtSn)/A catalyst had higher initial specific activity (13063.86 s^{-1}) and reaction rate constant K_d (h^{-1}) as to that of (PtSnZn)/A catalyst which had less initial specific activity and reaction constant (12489.69 s^{-1} and K_d (h^{-1}) of 0.06, respectively). In addition, the (PtSnZn)/A exhibited a minor peak at 473°C. This peak belonged to Zn [62]. The intensity of this peak showed very little dispersion of Zn mesoporous particle, and the presence of Zn with active metal Pt did not contribute much to enhance the overall catalytic activity of (PtSnZn)/A in terms of both initial specific activity and reaction rate constant.

3.4. NH_3-TPD Study. The catalytic activity of a supported catalyst depends on both catalyst preparation method and the surface acidity of the catalyst support (the acid-base behavior) which has direct impact to the dispersion of the active metal and/or promoter. To access such impact to the catalytic activity, both (PtSn)/A and (PtSnZn)/A catalysts were

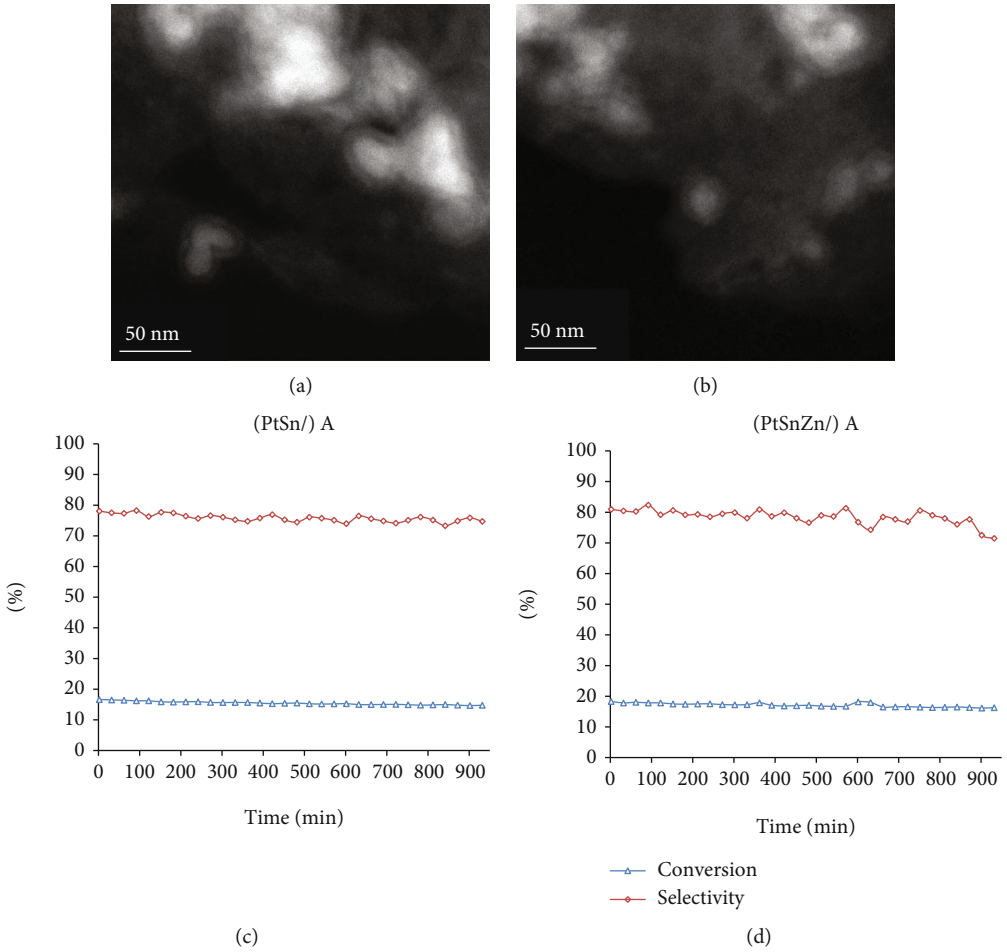

Figure 9: Comparison of TEM analysis and catalyst stability tests.

characterized by using NH_3-TPD technique. The obtained result is shown in Figure 5. Both (PtSn)/A and (PtSnZn)A exhibited different TPD curves. In the case of (PtSn)/A, the peak intensities are slightly less as to that of the peaks in (PtSnZn)/A catalyst. The low TPD peak intensity in (PtSn)/A corresponds to ammonia desorption from comparatively bit strong acidic sites. The slightly high intensity peaks of (PtSnZn)/A correspond to comparatively weak acidic sites. The extent of either weak and/or strong acid sites [63, 64] reflected to the unequal dispersion of the active metal Pt in each catalyst. Based on the results, the dispersion of Pt in (PtSn)/A was better as to that in (PtSnZn)/A catalyst. This leads to enhanced catalytic activity of (PtSn)/A both in terms of initial specific activity and reaction rate constant. However, the simultaneous addition of Zn, Sn, and Pt to the support leads to an overall decreased formation of undesired reaction products. Therefore, the presence of Zn in the catalyst's recipe increased the catalyst stability by suppressing the formation of undesired reaction products. Though, the overall catalytic activity of (PtSnZn)A is less as to that of (PtSn)/A. This could be attributed to active oxidation state(s) of metal, Pt/Sn, and/or Pt/Zn ratio, in addition to the formed Pt_xSn_y, Pt_xZn_y, and $Pt_xSn_yZn_z$ phases.

3.5. XRD Analysis. To investigate potential formation of Pt-Sn, Pt-Zn, and Pt-Sn-Zn phases in addition to the crystal orientation, both (PtSn)/A and (PtSnZn)/A catalysts were analyzed by using XRD analysis and results are shown in Figure 6.

The diffraction patterns of the (PtSnZn)/A catalyst exhibited Sn(110), Pt_4Sn, Pt(111), Pt(200), PtZn, Pt(311), and Pt(222) peaks in addition to the support γ-Al_2O_3 peaks [65, 66]. Among all the peaks attributed to the Pt, the Pt(111), Pt(311), and Pt(222) were the prominent as to that of Pt(200). A very less intense trace of Sn(110) and Pt_4Sn was also present in addition to PtZn peak in the (PtSnZn)/A catalyst. The (PtSn)/A had Sn(110), Pt_4Sn, Pt(111), Pt(200), Sn(211), Pt(220), and Pt(222) peaks in addition to γ-Al_2O_3 peaks. Among all the Pt peak, the Pt(111) and Pt(222) were the prominent in comparison to Pt(200) and Pt(220) peaks. Among Sn peaks, the Sn(110) was the prominent as to that of Sn(211) peak. In comparison, the Pt(220) and Pt (311) peaks were not found in both (PtSn)/A and (PtSnZn)A catalysts. The Pt(220) was identified in (PtSn)/A catalyst only, and the Pt(311) peak was present in the (PtSnZn)/A catalyst only. In addition, the (PtSnZn)/A exhibited a weak PtZn peak.

In brief, the different catalytic activity of (PtSn)/A and (PtSnZn)/A is attributed to the Pt_4Sn and PtZn phases in addition highly dispersed mesoporous Pt particles. Based on higher catalytic activity of (PtSn)/A catalyst, the presence

of Pt_4Sn phase is more beneficial as to that of PtZn phase. The formation of Pt_4Sn phase is attributed to the natural tendency of Pt towards Sn. Usually, the higher Pt/Sn ratio led to increased reaction rate.

3.6. XPS Analysis. To assess the metal ration and possible oxidation state of each active metal and surface chemical composition, both (PtSn)/A and (PtSnZn)/A catalysts were analyzed by using XPS. The results are shown in Figures 7 and 8.

The complete survey spectrum of (PtSn)/A catalyst exhibited Al 2p (73.64 eV), Al 2s (119.09 eV), Pt $4f_{5/2}$ (75.24 eV), Pt $4f_{7/2}$ (71.74 eV), Pt $4d_{5/2}$ (314.03 eV), Pt $4d_{5/2}$ (317.53 eV), Sn $3d_{5/2}$ (486.84 eV), and Sn $3d_{3/2}$ (494.99 eV) in addition to the O 1s and Cl 2p peaks. The deconvoluted Al 2p (73.64 eV) and Al 2s (119.09 eV) peaks of Al showed the presence of Al^{+3}, whereas the deconvoluted Pt $4d_{5/2}$ (314.03 eV) and Pt $4d_{5/2}$ (317.53 eV) peaks of Pt indicated the presence of Pt and Pt^{+2}, respectively. Finally, the Sn was present in the form of Sn^{+4} indicated by the deconvoluted Sn $3d_{5/2}$ (486.84 eV) and Sn $3d_{3/2}$ (317.53 eV) peaks of Sn. In summary, the active metal component of the (PtSn)/A catalyst was present in the form of Pt, Pt^{+2}, Al^{+3}, and Sn^{+4} ions. In addition, the Pt mesoporous particles were well dispersed within the support (see Figure 7(a); deconvolution exhibited the presence of both Al 2p and Pt 4f).

The (PtSnZn)/A had shown Al 2p (73.67 eV), Al 2s (119.07 eV), Pt $4f_{5/2}$ (75.21 eV), Pt $4f_{7/2}$ (71.77 eV), Pt $4d_{5/2}$ (314.09 eV), Pt $4d_{5/2}$ (317.55 eV), Sn $3d_{5/2}$ (486.81 eV), Sn $3d_{3/2}$ (494.93 eV), and Zn $2p_{3/2}$ (1021.77 eV) in addition to the O 1s and Cl 2p peaks. The deconvoluted Al 2p (73.67 eV) and Al 2s (119.07 eV) peaks of Al in the case of (PtSnZn)/A catalyst showed the presence of Al^{+3}. Similarly, the deconvoluted Pt $4d_{5/2}$ (314.09 eV) and Pt $4d_{5/2}$ (317.55 eV) peaks of Pt in the case of (PtSnZn)/A catalyst indicated the presence of Pt and Pt^{+2}, respectively. The Sn was present in the form of Sn^{+4} indicated by the deconvoluted Sn $3d_{5/2}$ (486.81 eV) and Sn $3d_{3/2}$ (494.93 eV) peaks of Sn in the (PtSnZn)/A catalyst. Finally, the Zn was present in the form of Zn^{+2} as indicated in the Zn $2p_{3/2}$ (1021.77 eV) peak of Zn in the (PtSnZn)/A catalyst. Furthermore, both Pt 4f and Al2p were present together (see Figure 8(a)) in the (PtSnZn)/A catalyst like the (PtSn)/A catalyst. In summary, the active metal component of the (PtSnZn)/A catalyst was present in the form of Pt, Pt^{+2}, Al^{+3}, Sn^{+4}, and Zn^{+2} states.

These XPS results were consistent as to that of XRD analysis. Both results indicated the presence of Pt_4Sn and PtZn. Overall, the extent of the formation of Pt_4Sn in the (PtSn)/A catalyst was more as to that in the (PtSnZn)/A catalyst because of the higher Pt/Sn ration in (PtSn)A catalyst (see Table 3).

The TEM analysis of best active catalysts ((PtSn)/A and (PtSnZn)/A) is shown in Figures 9(a) and 9(b). Both the catalysts had shown a random active metal distribution up to almost similar extent. In comparison, the (PtSn)/A catalyst has better and comparatively uniform Pt particle distribution surrounded by Sn within the proximity (see Figure 9(a)). However, in the (PtSnZn)/A catalyst, the Pt particles were in the close proximity to Sn as to that of Zn (see Figures 9(a) and 9(b)).

A comparison of the (PtSn)/A and (PtSnZn)/A catalyst's stability test is shown in Figures 9(c) and 9(d) for the first cycle. Both the catalysts had shown a fairly very good stability over a cycle run of 15 hours. However, the stability of (PtSn)/A was slightly better than that of the (PtSnZn)/A catalyst. The slight variation in C2H4 selectivity in the case of (PtSnZn)/A is attributed to the presence of Zn which may had led to the formation of coking either near or in the surrounding vicinity of Pt particles.

4. Conclusions

A series of Pt/A, Sn/A, PtSn/A, SnPt/A, (PtSn)/A, (PtSn)Zn/A, and (PtSnZn)/A catalysts were prepared by using either sequential and/or simultaneous wet impregnation (see Table 1) to study the impact of catalyst preparation approach to the catalytic activity, selectivity, and yield in direct ethane dehydrogenation. Among all the studied catalysts, the (PtSn)/A and (PtSnZn)/A had shown higher initial specific activity (s^{-1}) and reaction rate constant K_d (h^{-1}) (13063.86 (s^{-1}) and 12489.69 (s^{-1}) and 0.09 (h^{-1}) and 0.06 (h^{-1})), respectively. Based on the obtained results, the catalysts prepared by using simultaneous wet impregnation had shown higher catalytic activity as to that of sequential wet impregnation. The catalyst preparation approach had direct/indirect impact to the availability and dispersion of mesoporous particles of active metal and/or promoter in the catalyst. This led to influence either to hinder the C-C cleavage and/or to promote C-H bond cleavage in the dehydrogenation of ethane to ethene. Among all studied catalysts, the (PtSn)/A had shown better catalyst stability for an experimental cycle run of 15 hours. With the increase in reaction temperature, both % conversion and % selectivity of desired reaction product were increased. The active metal component was present in the form of Pt, Pt^{+2}, Al^{+3}, Sn^{+4}, and Zn^{+2} states. The enhanced catalytic activity is attributed to the Pt_4Sn and PtZn formed phases in addition to highly dispersed mesoporous Pt particles.

Data Availability

All the data is included in the manuscript.

Conflicts of Interest

The authors declare that they have no conflicts of interest.

Acknowledgments

This project was funded by the Deanship of Scientific Research (DSR) at King Abdulaziz University, Jeddah, under grant no. G:58-135-1442. The authors, therefore, acknowledge with thanks DSR for technical and financial support.

References

[1] S. Arndt, T. Otremba, U. Simon, M. Yildiz, H. Schubert, and R. Schomäcker, "$Mn–Na_2WO_4/SiO_2$ as catalyst for the

oxidative coupling of methane. What is really known?," *Applied Catalysis A: General*, vol. 425-426, pp. 53–61, 2012.

[2] A. Cimino and F. S. Stone, "Oxide solid solutions as catalysts," in *Advances in Catalysis*, pp. 141–306, Academic Press, 2002.

[3] J. A. C. Dias and J. M. Assaf, "Influence of calcium content in Ni/CaO/γ-Al_2O_3 catalysts for CO_2-reforming of methane," *Catalysis Today*, vol. 85, no. 1, pp. 59–68, 2003.

[4] J. I. Gutiérrez-Ortiz, B. de Rivas, R. López-Fonseca, S. Martín, and J. R. González-Velasco, "Structure of Mn–Zr mixed oxides catalysts and their catalytic performance in the gas-phase oxidation of chlorocarbons," *Chemosphere*, vol. 68, no. 6, pp. 1004–1012, 2007.

[5] M. S. Lee, J. Y. Lee, D.-W. Lee, D. J. Moon, and K.-Y. Lee, "The effect of Zn addition into NiFe2O4 catalyst for high-temperature shift reaction of natural gas reformate assuming no external steam addition," *International Journal of Hydrogen Energy*, vol. 37, no. 15, pp. 11218–11226, 2012.

[6] C. Resini, M. Panizza, L. Arrighi et al., "A study of the reaction pathway upon propane oxidation over V–K/Al2O3 catalysts," *Chemical Engineering Journal*, vol. 89, no. 1–3, pp. 75–87, 2002.

[7] J. Wu, S. Mallikarjun Sharada, C. Ho, A. W. Hauser, M. Head-Gordon, and A. T. Bell, "Ethane and propane dehydrogenation over PtIr/Mg(Al)O," *Applied Catalysis A: General*, vol. 506, pp. 25–32, 2015.

[8] Y. Xu, H. Sang, K. Wang, and X. Wang, "Catalytic dehydrogenation of isobutane in the presence of hydrogen over Cs-modified Ni2P supported on active carbon," *Applied Surface Science*, vol. 316, pp. 163–170, 2014.

[9] G. Aguilar-Ríos, P. Salas, M. A. Valenzuela, H. Armendáriz, J. A. Wang, and J. Salmones, "Propane dehydrogenation activity of Pt and Pt–Sn catalysts supported on magnesium aluminate: influence of steam and hydrogen," *Catalysis Letters*, vol. 60, no. 1-2, pp. 21–25, 1999.

[10] G. Aguilar-Ríos, M. Valenzuela, P. Salas et al., "Hydrogen interactions and catalytic properties of platinum-tin supported on zinc aluminate," *Applied Catalysis A, General*, vol. 127, no. 1-2, pp. 65–75, 1995.

[11] F. M. Ashmawy, "Catalytic dehydrogenation of propane on chromia, palladium and platinum supported catalysts," *Journal of Biochemical Toxicology*, vol. 27, no. 1, pp. 137–142, 1977.

[12] A. Ates, C. Hardacre, and A. Goguet, "Oxidative dehydrogenation of propane with N2O over Fe-ZSM-5 and Fe–SiO2: influence of the iron species and acid sites," *Applied Catalysis A: General*, vol. 441-442, pp. 30–41, 2012.

[13] K. G. Azzam, G. Jacobs, W. D. Shafer, and B. H. Davis, "Dehydrogenation of propane over Pt/KL catalyst: investigating the role of L-zeolite structure on catalyst performance using isotope labeling," *Applied Catalysis A: General*, vol. 390, no. 1–2, pp. 264–270, 2010.

[14] L. Bai, Y. Zhou, Y. Zhang, H. Liu, and M. Tang, "Influence of calcium addition on catalytic properties of PtSn/ZSM-5 catalyst for propane dehydrogenation," *Catalysis Letters*, vol. 129, no. 3-4, pp. 449–456, 2009.

[15] O. A. Bariås, A. Holmen, and E. A. Blekkan, "Propane dehydrogenation over supported platinum catalysts: effect of tin as a promoter," *Catalysis Today*, vol. 24, no. 3, pp. 361–364, 1995.

[16] M. M. Bhasin, J. H. McCain, B. V. Vora, T. Imai, and P. R. Pujadó, "Dehydrogenation and oxydehydrogenation of paraffins to olefins," *Applied Catalysis A: General*, vol. 221, no. 1-2, pp. 397–419, 2001.

[17] Y.-L. Bi, K.-J. Zhen, R. X. Valenzuela, M.-J. Jia, and V. Cortés Corberán, "Oxidative dehydrogenation of isobutane over LaBaSm oxide catalyst: influence of the addition of CO2 in the feed," *Catalysis Today*, vol. 61, no. 1-4, pp. 369–375, 2000.

[18] P. Biloen, "Catalytic dehydrogenation of propane to propene over platinum and platinum-gold alloys," *Journal of Catalysis*, vol. 50, no. 1, pp. 77–86, 1977.

[19] S. A. Bocanegra, A. A. Castro, A. Guerrero-Ruíz, O. A. Scelza, and S. R. de Miguel, "Characteristics of the metallic phase of Pt/Al2O3 and Na-doped Pt/Al2O3 catalysts for light paraffins dehydrogenation," *Chemical Engineering Journal*, vol. 118, no. 3, pp. 161–166, 2006.

[20] S. A. Bocanegra, S. R. de Miguel, I. Borbath, J. L. Margitfalvi, and O. A. Scelza, "Behavior of bimetallic PtSn/Al2O3 catalysts prepared by controlled surface reactions in the selective dehydrogenation of butane," *Journal of Molecular Catalysis A: Chemical*, vol. 301, no. 1–2, pp. 52–60, 2009.

[21] F. Cavani, C. Comuzzi, G. Dolcetti et al., "Oxidative dehydrogenation of isobutane to isobutene: Dawson-type heteropolyoxoanions as stable and selective heterogeneous catalysts," *Journal of Catalysis*, vol. 160, no. 2, pp. 317–321, 1996.

[22] M. Chen, J. Xu, F. Su et al., "Dehydrogenation of propane over spinel-type gallia–alumina solid solution catalysts," *Journal of Catalysis*, vol. 256, no. 2, pp. 293–300, 2008.

[23] R. D. Cortright, J. M. Hill, and J. A. Dumesic, "Selective dehydrogenation of isobutane over supported Pt/Sn catalysts," *Catalysis Today*, vol. 55, no. 3, pp. 213–223, 2000.

[24] N. O. Elbashir, S. M. Al-Zahrani, A. E. Abasaeed, and M. Abdulwahed, "Alumina-supported chromium-based mixed-oxide catalysts in oxidative dehydrogenation of isobutane to isobutene," *Chemical Engineering and Processing: Process Intensification*, vol. 42, no. 10, pp. 817–823, 2003.

[25] M. E. Harlin, V. M. Niemi, and A. O. I. Krause, "Alumina-supported vanadium oxide in the dehydrogenation of butanes," *Journal of Catalysis*, vol. 195, no. 1, pp. 67–78, 2000.

[26] E. L. Jablonski, A. A. Castro, O. A. Scelza, and S. R. de Miguel, "Effect of Ga addition to Pt/Al2O3 on the activity, selectivity and deactivation in the propane dehydrogenation," *Applied Catalysis A: General*, vol. 183, no. 1, pp. 189–198, 1999.

[27] S. B. Kogan and M. Herskowitz, "Selective propane dehydrogenation to propylene on novel bimetallic catalysts," *Catalysis Communications*, vol. 2, no. 5, pp. 179–185, 2001.

[28] S. B. Kogan, H. Schramm, and M. Herskowitz, "Dehydrogenation of propane on modified Pt/θ-alumina performance in hydrogen and steam environment," *Applied Catalysis A: General*, vol. 208, no. 1-2, pp. 185–191, 2001.

[29] D. I. Kondarides, K. Tomishige, Y. Nagasawa, U. Lee, and Y. Iwasawa, "Characterization and performance of a [PtMo6]MgO catalyst for alkane-to-alkene conversion," *Journal of Molecular Catalysis A: Chemical*, vol. 111, no. 1-2, pp. 145–165, 1996.

[30] M.-H. Lee, B. M. Nagaraja, P. Natarajan et al., "Effect of potassium addition on bimetallic PtSn/θ-Al2O3 catalyst for dehydrogenation of propane to propylene," *Research on Chemical Intermediates*, vol. 42, no. 1, pp. 123–140, 2016.

[31] Q. Li, Z. Sui, X. Zhou, and D. Chen, "Kinetics of propane dehydrogenation over Pt–Sn/Al2O3 catalyst," *Applied Catalysis A: General*, vol. 398, no. 1-2, pp. 18–26, 2011.

[32] Y. Li, Z. Zhang, J. Wang, C. Ma, H. Yang, and Z. Hao, "Direct dehydrogenation of isobutane to isobutene over carbon

catalysts," *Chinese Journal of Catalysis*, vol. 36, no. 8, pp. 1214–1222, 2015.

[33] J. Llorca, N. Homs, J. León, J. Sales, J. L. G. Fierro, and P. Ramirez de la Piscina, "Supported Pt–Sn catalysts highly selective for isobutane dehydrogenation: preparation, characterization and catalytic behavior," *Applied Catalysis A: General*, vol. 189, no. 1, pp. 77–86, 1999.

[34] M. P. Lobera, C. Téllez, J. Herguido, and M. Menéndez, "Transient kinetic modelling of propane dehydrogenation over a Pt–Sn–K/Al2O3 catalyst," *Applied Catalysis A: General*, vol. 349, no. 1-2, pp. 156–164, 2008.

[35] S. Luo, N. Wu, B. Zhou, S.-b. He, J.-s. Qiu, and C.-l. Sun, "Effect of alumina support on the performance of Pt- Sn-K/γ-Al_2O_3 catalyst in the dehydrogenation of isobutane," *Journal of Fuel Chemistry and Technology*, vol. 41, no. 12, pp. 1481–1487, 2013.

[36] Z. Ma, Y. Mo, J. Li, C. An, and X. Liu, "Optimization of PtSnK/Al2O3 isobutane dehydrogenation catalyst prepared by an impregnation-reduction method," *Journal of Natural Gas Science and Engineering*, vol. 27, Part 2, pp. 1035–1042, 2015.

[37] M. Ohta, Y. Ikeda, and A. Igarashi, "Preparation and characterization of Pt/ZnO-Cr_2O_3 catalyst for low-temperature dehydrogenation of isobutane," *Applied Catalysis A: General*, vol. 258, no. 2, pp. 153–158, 2004.

[38] M. Ohta, Y. Ikeda, and A. Igarashi, "Additive effect of Sn in Pt–Sn/ZnO–Cr_2O_3 catalyst for low-temperature dehydrogenation of isobutane," *Applied Catalysis A: General*, vol. 266, no. 2, pp. 229–233, 2004.

[39] G. J. Siri, G. R. Bertolini, M. L. Casella, and O. A. Ferretti, "PtSn/γ-Al2O3 isobutane dehydrogenation catalysts: the effect of alkaline metals addition," *Materials Letters*, vol. 59, no. 18, pp. 2319–2324, 2005.

[40] G. J. Siri, M. L. Casella, G. F. Santori, and O. A. Ferretti, "Tin/platinum on alumina as catalyst for dehydrogenation of isobutane. Influence of the preparation procedure and of the addition of lithium on the catalytic properties," *Industrial & Engineering Chemistry Research*, vol. 36, no. 11, pp. 4821–4826, 1997.

[41] Y. Takita, X. Qing, A. Takami, H. Nishiguchi, and K. Nagaoka, "Oxidative dehydrogenation of isobutane to isobutene III: reaction mechanism over CePO4 catalyst," *Applied Catalysis A: General*, vol. 296, no. 1, pp. 63–69, 2005.

[42] Y.-P. Tian, P. Bai, S.-M. Liu, X.-M. Liu, and Z.-F. Yan, "VOx–K2O/γ-Al2O3 catalyst for nonoxidative dehydrogenation of isobutane," *Fuel Processing Technology*, vol. 151, pp. 31–39, 2016.

[43] N. V. Vernikovskaya, I. G. Savin, V. N. Kashkin et al., "Dehydrogenation of propane–isobutane mixture in a fluidized bed reactor over Cr2O3/Al2O3 catalyst: experimental studies and mathematical modelling," *Chemical Engineering Journal*, vol. 176-177, pp. 158–164, 2011.

[44] V. P. Vislovskiy, N. T. Shamilov, A. M. Sardarly et al., "Oxidative conversion of isobutane to isobutene over V-Sb-Ni oxide catalysts," *Applied Catalysis A: General*, vol. 250, no. 1, pp. 143–150, 2003.

[45] B. V. Vora, "Development of dehydrogenation catalysts and processes," *Topics in Catalysis*, vol. 55, no. 19-20, pp. 1297–1308, 2012.

[46] H. F. Abbas and W. M. A. Wan Daud, "Hydrogen production by methane decomposition: a review," *International Journal of Hydrogen Energy*, vol. 35, no. 3, pp. 1160–1190, 2010.

[47] V. Iannazzo, G. Neri, S. Galvagno, M. Di Serio, R. Tesser, and E. Santacesaria, "Oxidative dehydrogenation of isobutane over V_2O_5-based catalysts prepared by grafting vanadyl alkoxides on TiO_2·SiO_2 supports," *Applied Catalysis A: General*, vol. 246, no. 1, pp. 49–68, 2003.

[48] G. A. Martin and C. Mirodatos, "Surface chemistry in the oxidative coupling of methane," *Fuel Processing Technology*, vol. 42, no. 2–3, pp. 179–215, 1995.

[49] P. Moriceau, B. Grzybowska, Y. Barbaux, G. Wrobel, and G. Hecquet, "Oxidative dehydrogenation of isobutane on Cr–Ce–O oxide:: I. Effect of the preparation method and of the Cr content," *Applied Catalysis A: General*, vol. 168, no. 2, pp. 269–277, 1998.

[50] F. Sala and F. Trifiró, "Relationship between structure and activity of antimony mixed oxides in 1-butene oxidation," *Journal of Catalysis*, vol. 41, no. 1, pp. 1–13, 1976.

[51] J. C. Serrano-Ruiz, A. Sepulveda-Escribano, and F. Rodriguez-Reinoso, "Bimetallic PtSn/C catalysts promoted by ceria: application in the nonoxidative dehydrogenation of isobutane," *Journal of Catalysis*, vol. 246, no. 1, pp. 158–165, 2007.

[52] H. Shimada, T. Akazawa, N.-O. Ikenaga, and T. Suzuki, "Dehydrogenation of isobutane to isobutene with iron-loaded activated carbon catalyst," *Applied Catalysis A: General*, vol. 168, no. 2, pp. 243–250, 1998.

[53] T. Otroshchenko, J. Radnik, M. Schneider, U. Rodemerck, D. Linke, and E. V. Kondratenko, "Bulk binary ZrO2-based oxides as highly active alternative-type catalysts for non-oxidative isobutane dehydrogenation," *Chemical Communications*, vol. 52, no. 52, pp. 8164–8167, 2016.

[54] U. Rodemerck, E. V. Kondratenko, T. Otroshchenko, and D. Linke, "Unexpectedly high activity of bare alumina for non-oxidative isobutane dehydrogenation," *Chemical Communications*, vol. 52, no. 82, pp. 12222–12225, 2016.

[55] U. Rodemerck, S. Sokolov, M. Stoyanova, U. Bentrup, D. Linke, and E. V. Kondratenko, "Influence of support and kind of VOx species on isobutene selectivity and coke deposition in non-oxidative dehydrogenation of isobutane," *Journal of Catalysis*, vol. 338, pp. 174–183, 2016.

[56] J. Nam and F. E. Celik, "Effect of tin in the bulk of platinum–tin alloys for ethane dehydrogenation," *Topics in Catalysis*, vol. 63, no. 7-8, pp. 700–713, 2020.

[57] Q. Zhang, K. Zhang, S. Zhang et al., "Ga3+-stabilized Pt in PtSn-Mg(Ga)(Al)O catalyst for promoting ethane dehydrogenation," *Journal of Catalysis*, vol. 368, pp. 79–88, 2018.

[58] A. M. Ali, A. A. Zahrani, M. A. Daous, M. U. S. Podila, and L. A. Petrov, "Highly active and selective PtSnM1/gamma-Al2O3 catalyst for direct propane dehydrogenation," *Journal of the Chemical Society of Pakistan*, vol. 43, no. 3, pp. 342–360, 2021.

[59] F. M. Li, H. Q. Yang, T. Y. Ju, X. Y. Li, and C. W. Hu, "Activation of propane C-H and C-C bonds by gas-phase Pt atom: a theoretical study," *International Journal of Molecular Sciences*, vol. 13, no. 7, pp. 9278–9297, 2012.

[60] S.-U. Lee, Y.-J. Lee, S.-J. Kwon, J.-R. Kim, and S.-Y. Jeong, "Pt-Sn supported on beta zeolite with enhanced activity and stability for propane dehydrogenation," *Catalysts*, vol. 11, no. 1, p. 25, 2021.

[61] P. D. Zgolicz, V. I. Rodríguez, I. M. J. Vilella, S. R. de Miguel, and O. A. Scelza, "Catalytic performance in selective hydrogenation of citral of bimetallic Pt–Sn catalysts supported on

MgAl2O4 and γ-Al2O3," *Applied Catalysis A: General*, vol. 392, no. 1-2, pp. 208–217, 2011.

[62] F. Lin, R. Delmelle, T. Vinodkumar, B. M. Reddy, A. Wokaun, and I. Alxneit, "Correlation between the structural characteristics, oxygen storage capacities and catalytic activities of dual-phase Zn-modified ceria nanocrystals," *Catalysis Science & Technology*, vol. 5, no. 7, pp. 3556–3567, 2015.

[63] D. Guillaume, S. Gautier, I. Despujol, F. Alario, and P. Beccat, "Characterization of acid sites on γ-alumina and chlorinated γ-alumina by 31P NMR of adsorbed trimethylphosphine," *Catalysis Letters*, vol. 43, no. 3-4, pp. 213–218, 1997.

[64] W. Kania and K. Jurczyk, "Acid-base properties of modified γ-alumina," *Applied Catalysis*, vol. 34, pp. 1–12, 1987.

[65] S. Bing-Jian, K.-W. Wang, C.-J. Tseng, C.-H. Wang, and Y.-J. Hsueh, "Synthesis and catalytic property of PtSn/C toward the ethanol oxidation reaction," *International Journal of Electrochemical Science*, vol. 7, no. 6, pp. 5246–5255, 2012.

[66] A. Bonesi, W. E. Triaca, and A. M. C. Luna, "Nanocatalysts for ethanol oxidation. Synthesis and characterisation," *Portugaliae Electrochimica Acta*, vol. 27, no. 3, pp. 193–201, 2009.

Hindawi
Journal of Nanomaterials
Volume 2022, Article ID 3855582, 13 pages
https://doi.org/10.1155/2022/3855582

Research Article

Functional Properties of Donor (Al) and Acceptor (Cu) Codoped High Dielectric Constant ZnO Nanoparticles

Huma Tariq and Fahad Azad

School of Natural Sciences (SNS), National University of Sciences and Technology (NUST), 44000 Islamabad, Pakistan

Correspondence should be addressed to Fahad Azad; fahad.azad@sns.nust.edu.pk

Received 9 September 2021; Revised 5 December 2021; Accepted 14 December 2021; Published 13 January 2022

Academic Editor: Sami-Ullah Rather

In this work, we have synthesized donor-acceptor (Al-Cu) codoped ZnO nanoparticles with a doping concentration of 0%, 0.25%, 0.5%, and 0.75% by coprecipitation method. The synthesized samples were then annealed at 350°C and 600°C. All the samples showed wurtzite structure of ZnO with no secondary phase. The increase in doping concentration led to deterioration of crystalline quality, while improved crystallinity was observed at higher annealing temperature. The morphological study of these samples showed good grain-to-grain contact with less isolated pores. These samples were further characterized by impedance spectroscopy for analyzing dielectric properties. The values of the real part of dielectric constant and tangent loss showed decreasing trend with frequency. The appearance of semicircular arcs in the impedance complex plane plots indicates contribution of grains and grain boundaries and presence of different relaxation processes. 0.5% Al and Cu codoped ZnO showed the best dielectric response with a high value of dielectric constant and low tangent loss.

1. Introduction

Energy is the crucial element for worldwide development. Oil price fluctuation, depletion of fossil fuel resources, and practical challenges in controlling environmental pollution have made renewable energy the most promising option. However, the high cost and unsteady nature of power production from these sources limit the use of renewable energy as a primary source. Therefore, the production of economical and efficient energy storage devices is crucial for using renewable energy for steady supply of power. Therefore, materials with high dielectric constant are becoming a continuous source of attraction due to their application in high energy storage applications. Extensive research has been carried out on ferroelectric-based materials and nonferroelectric like $CaCu_3Ti4O_{12}$ [1–5], to achieve high permittivity. However, frequency and temperature dependence of permittivity and high tangent loss have restricted their use in device miniaturization and high-frequency applications [1, 6, 7]. For the realization of high dielectric constant, one of the following phenomena must exist in the host material such as hopping charge transport, ferroelectricity, interface effects, metal insulator transition, or surface barrier layer capacitance (SBLC). In ceramic materials, colossal permittivity (CP) phenomena are attributed to internal barrier layer capacitance (IBLC) [8, 9], due to planar defects like twin and grain boundaries. Recently, a defect engineering approach was employed for the realization of high dielectric constant in oxide-based materials. The localization of carriers (electrons or holes) into substitutional defects and disorders like amorphous structure has been found responsible for CP. Moreover, hopping of localized defect state lowers tangent loss in these materials. Recently, frequency- and temperature-independent CP and low dielectric loss were achieved in In and Nb codoped TiO_2 ceramic system. Donor (Nb) and acceptor (In) substitution in TiO_2 created local delocalized electron, consequently defect dipole-type clusters [4]. These electron-pinned defect dipoles were argued to be the reason for observed CP. Following this donor-acceptor substitution approach, there have been many reports in which CP with low dielectric loss has been achieved [9–11]. Efforts are still being made to fabricate CP materials with low dielectric losses, as no practical solution has yet been found for temperature and frequency stable

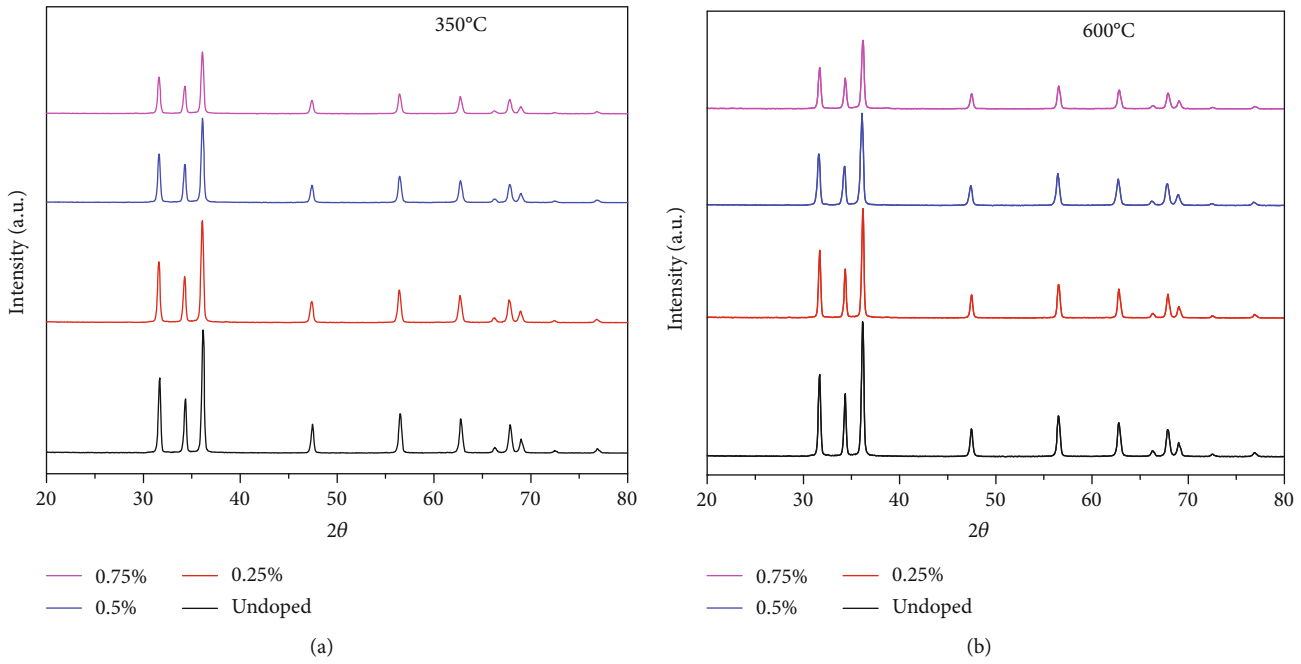

Figure 1: X-ray diffraction analysis of pristine and Al and Cu codoped ZnO with various doping concentrations annealed at (a) 350°C and (b) 600°C.

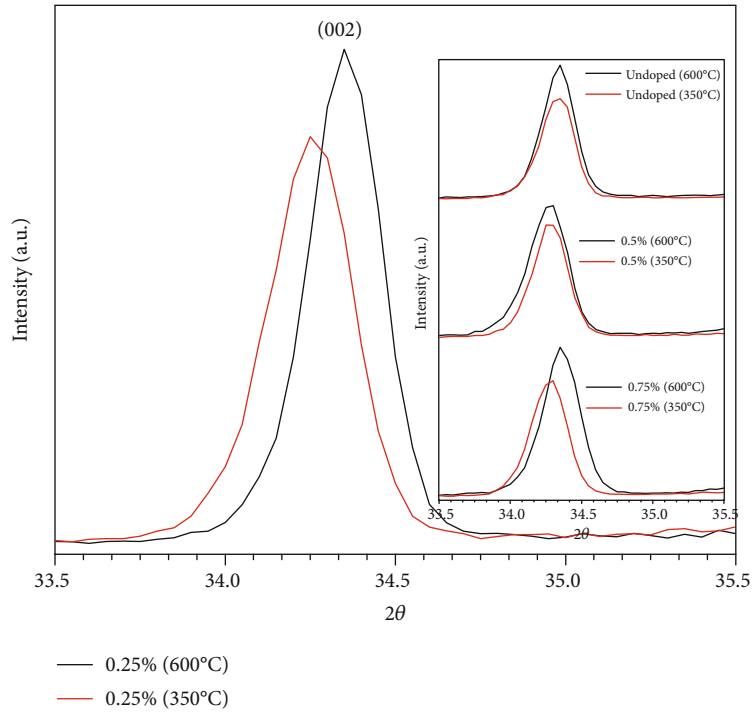

Figure 2: (002) diffraction peak of pristine and Al and Cu codoped ZnO (0.25%, 0.5%, and 0.75% annealed at 350°C and 600°C.

permittivity and dielectric loss [12, 13]. In this work, we have followed a similar approach by codoping Al (donor) and Cu (acceptor) in a wide-bandgap ZnO host. We synthesized Al and Cu codoped ZnO ($(Al_{0.5}Cu_{0.5})_xZn_{1-x}O$) samples with $x = 0.25$ %, 0.50%, and 0.75%. X-ray diffraction (XRD) and scanning electron microscopy (SEM) were employed to characterize structural and morphological properties of the synthesized samples. The Williamson-Hall method was used to plot size-strain graphs. The bandgap energies of the synthesized samples were calculated using diffused reflectance spectroscopy (DRS). Impedance spectroscopy (IS) was carried out to study dielectric properties of these samples. We found that 0.5% Al and Cu codoped ZnO showed relatively better results with high dielectric constant and low tangent loss.

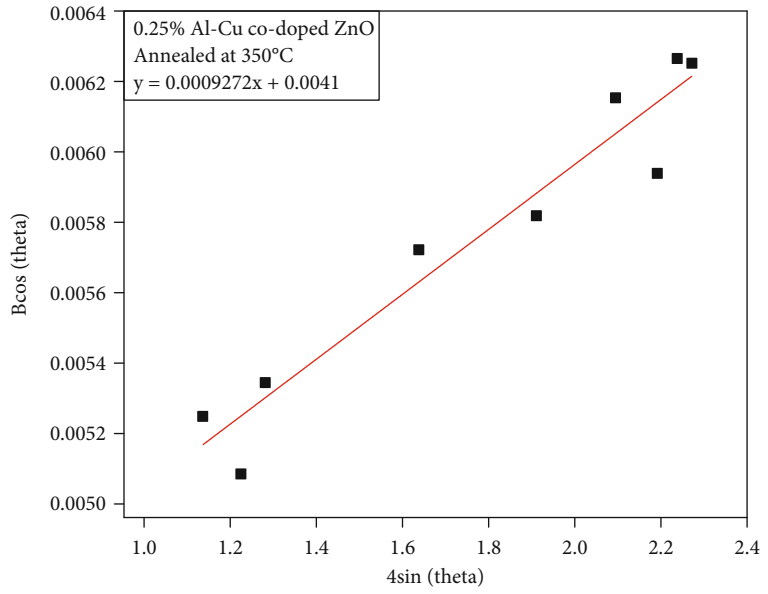

(a)

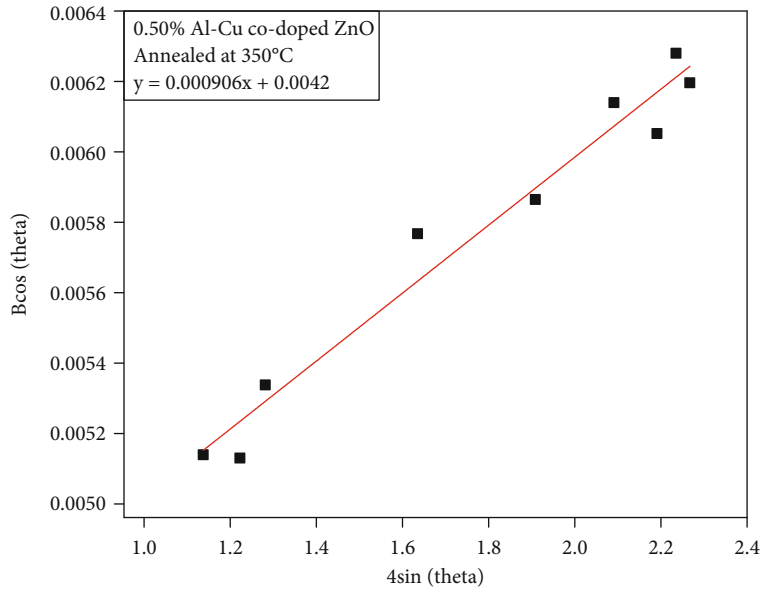

(b)

Figure 3: Continued.

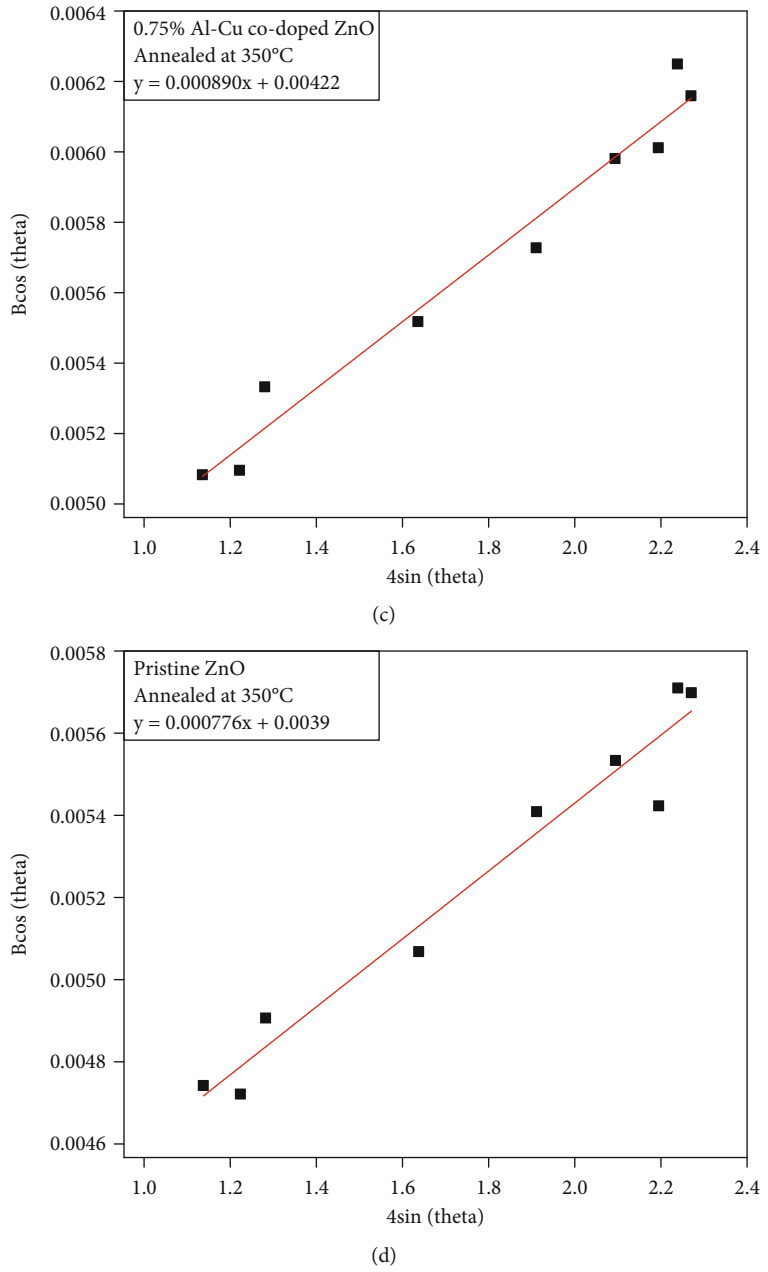

Figure 3: WH plots of (a) 0.25%, (b) 0.5%, (c) 0.75% Al and Cu codoped ZnO, and (d) pristine ZnO annealed at 350°C.

2. Experimental Setup

Pristine and Al and Cu codoped ZnO with varied doping concentration were prepared using coprecipitation method. All the precursors were purchased from Sigma-Aldrich and used without any further purification. To synthesize undoped ZnO, 1 M aqueous solution of zinc nitrate ($Zn(NO_3)_2{\cdot}6H_2O$) was prepared in a beaker. 2 M aq. NaOH solution was prepared separately in another beaker and added dropwise in the above solution at room temperature under constant stirring until pH 7 was achieved [14]. The solution was kept stirring for 30 minutes after adding NaOH solution. The obtained precipitates were washed seven times with deionized water and then collected by centrifugation. The following composition of $Al_{0.5x}Cu_{0.5x}Zn_{1-x}O$ with $x = 0.25$, 0.50, and 0.75 mol was synthesized using the same method. Stoichiometric ratios of $Zn(NO_3)_2{\cdot}6H_2O$, $Al(NO_3)_3{\cdot}9H_2O$, and anhydrous $CuSO_4$ were dissolved in deionized water to prepare homogenous solution. The obtained product was dried in an oven for 24 hours at 70°C and then annealed at 350°C and 600°C for 4 hours. The samples which were grown at higher pH showed development of secondary phase; therefore, all the samples were prepared in neutral phase.

An X-ray diffractometer (model: Bruker D8) at an incident wavelength of 1.5406 Å was used to study structural properties. A scanning electron microscope (model: TESCAN VEGA-3) was employed for the morphological study

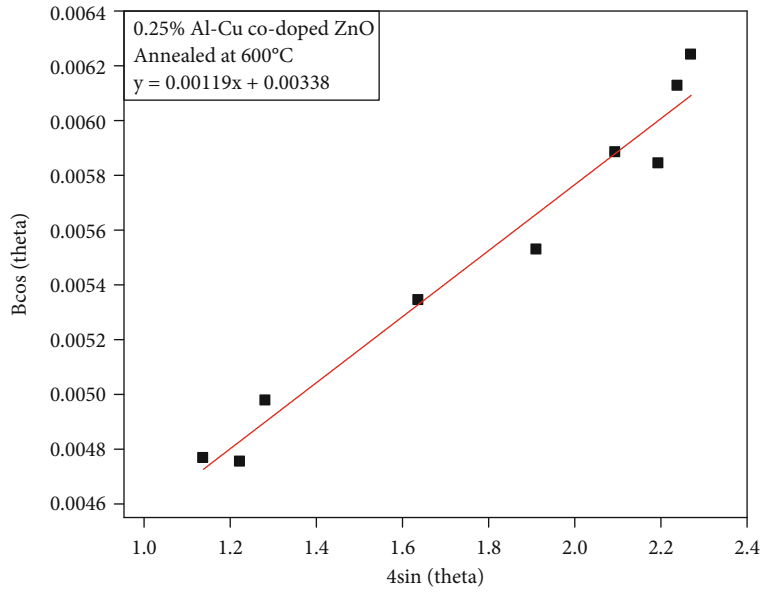

(a)

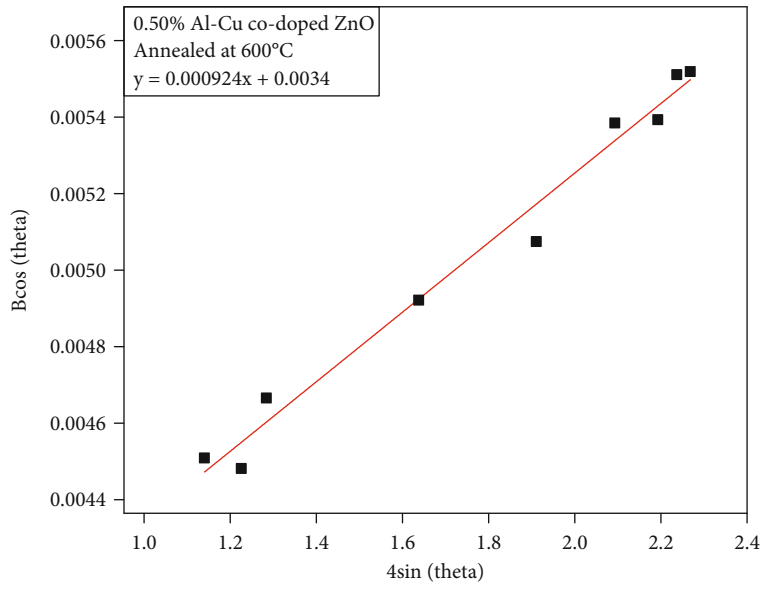

(b)

Figure 4: Continued.

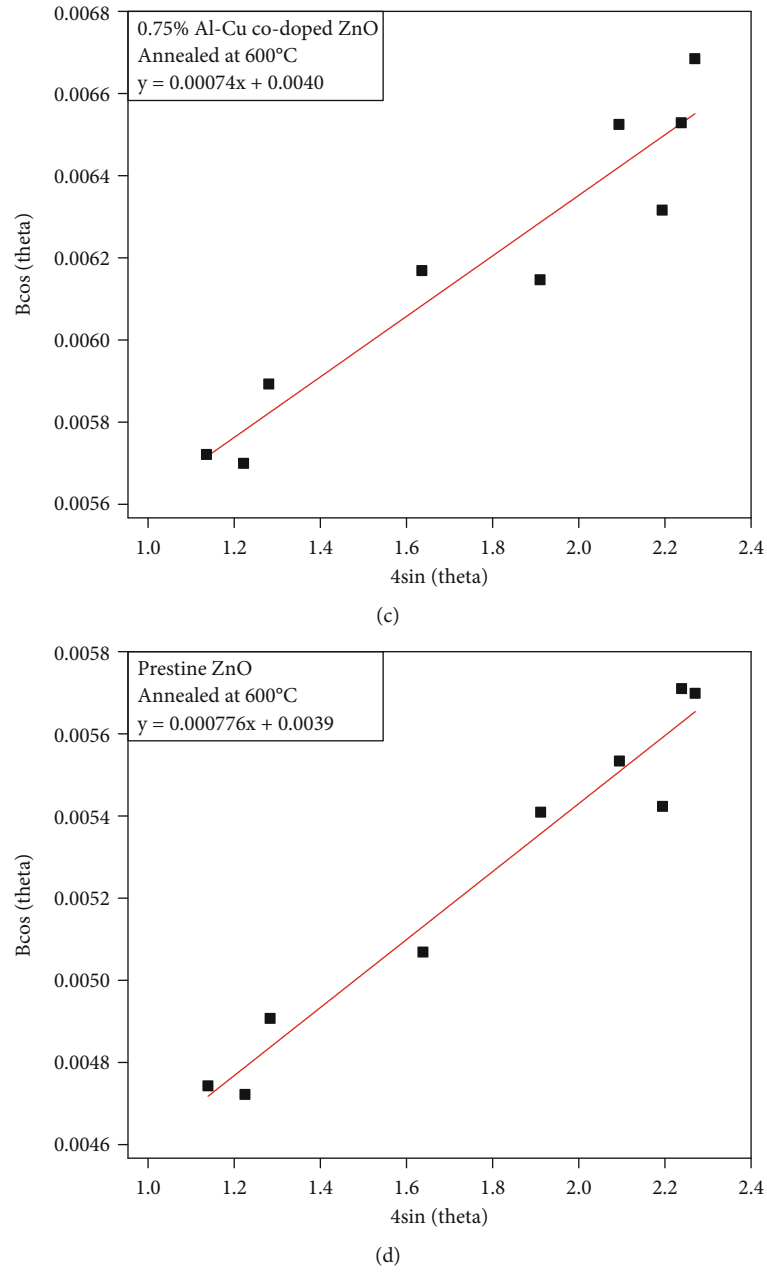

Figure 4: WH plots of (a) 0.25%, (b) 0.5%, (c) 0.75% Al and Cu codoped ZnO, and (d) pristine ZnO annealed at 600°C.

Table 1: Crystallite size (D), strain (ε), dislocation density (δ), and lattice parameters (a, c) of pristine and Al and Cu codoped ZnO (0.25%, 0.5%, and 0.75%) annealed at 350°C and 600°C.

Sample name	Annealed at 350°C					Annealed at 600°C				
	D (nm)	Strain (ε)	δ (nm^{-2})	a (Å)	c (Å)	D (nm)	Strain (ε)	δ (nm^{-2})	a (Å)	c (Å)
Pristine ZnO	35.53	1.76E-03	7.92E-04	3.34	5.46	45.53	2.17E-03	4.82E-04	3.31	5.43
0.25% codoped ZnO	33.80	0.90E-03	8.75E-04	3.25	5.31	41.06	1.19E-03	5.93E-04	3.23	5.29
0.50% codoped ZnO	33.00	0.90E-03	9.18E-04	3.19	5.21	40.76	0.92E-03	6.01E-04	3.19	5.21
0.75% codoped ZnO	32.84	0.89E-03	9.27E-04	3.16	5.11	34.65	0.74E-03	8.32E-04	3.12	5.07

of the synthesized samples; compositional analysis was carried out using the attached EDX assembly. Bandgap analysis of the samples was carried out by diffused reflectance spectroscopy (model: lambda 365). Room temperature impedance spectroscopy was performed in frequency range 1-10^7 Hz using an Alpha-N Analyzer (Novocontrol, Germany). Samples were fixed into a sample holder by binding copper wires on both sides using silver paint. AC signal of

0.5 V was applied on all the samples. WINDETA software was used for interfacing experimental setup of the analyzer with the computer for data acquisition.

3. Results and Analysis

X-ray diffraction patterns of pristine and Al and Cu codoped samples at a doping concentration of 0.25%, 0.5%, and 0.75% annealed at 350°C and 600°C are shown in Figure 1. All the samples show a hexagonal wurtzite structure of ZnO. The peaks could be indexed as (100), (002), (101), (102), (110), (103), (200), (112), (201), (204), and (202) in accordance with JCPDF-01-079-0208. No unidentified diffraction peak related to any secondary phase was observed in all the diffraction patterns. All the samples showed a well-defined peak profile with reasonable intensity that indicates good crystalline quality. A decrease in the peak intensity was observed with increase in doping concentration at both annealing temperatures which shows deterioration of crystallinity with increase in doping concentration [15, 16].

Figure 2 shows (002) peak profile of 0.25% Al and Cu codoped ZnO sample annealed at 350°C and 600°C. The graph shows an increase in the peak intensity and decrease in full width at half maximum (FWHM) with increase in annealing temperature. Furthermore, a shift in the peak position of (002) peak was also observed with annealing temperature. Similar effects were also observed in other samples, and data is shown in the inset of Figure 2. The increase in peak intensity along with decreased FWHM indicates improvement of crystallinity upon annealing at higher temperature [17]. This enhancement of crystalline quality is due to grain growth at high temperature. The shift of (002) diffraction peak towards higher angle with annealing (at higher temperature) is linked with the change in microstrain [18]. This phenomenon was also reported in pristine and other doped nanoparticles of ZnO [17]. This change in microstrain might be associated with decreased lattice parameters due to formation of oxygen vacancy at higher annealing temperature [17] because of doping. Felemban et al. [19] also reported that isolated oxygen vacancy introduces contraction of both lattice parameters. Furthermore, ZnO nanoparticles have different defects that reportedly happen to disappear when the sample is annealed at high temperature resulting to the shrinkage of lattice parameters [20]. Therefore, it might be inferred that an increase in annealing temperature leads to varied defect chemistry (in doped samples) that reduces the lattice strain and corresponding lattice parameter.

The Williamson-Hall (WH) method was used to analyze crystallite size (D) and microstrain of pristine ZnO and Al and Cu codoped ZnO at various doping concentrations and annealing temperatures (Figures 3(a)–3(d) and Figures 4(a)–4(d)). The crystallite size (D), microstrain, dislocation density, and lattice parameters of these samples are shown in Table 1. The D value of the samples decreases with increase in doping concentration at each annealing temperature; the maximum D value was obtained for pristine ZnO [21]. An increase in the D value was observed with annealing temperature in pristine and codoped samples at a fixed doping concentration. The dislocation density was found to increase with doping concentration at a fixed annealing temperature and decrease with increase in annealing temperature at a fixed doping concentration. Furthermore, shrinkage of lattice parameters was observed with doping concentration at a fixed annealing temperature in these samples which indicates reduction of cell volume [22]. This decrease of D-value, increase of dislocation density, and shrinkage of lattice parameters with doping concentration indicate deterioration of crystalline quality due to lattice mismatch [23], whereas increase of D-value and decrease of dislocation density at fixed doping concentration with

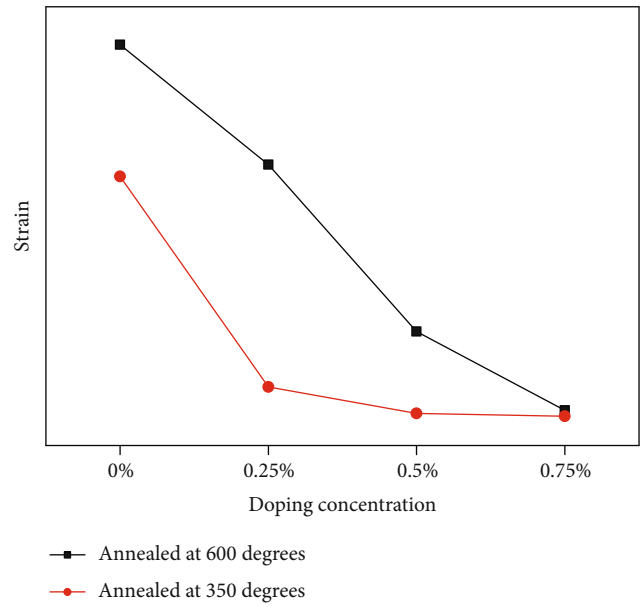

Figure 5: Trend of microstrain as a function of doping concentration of Al and Cu codoped ZnO annealed at 350°C and 600°C.

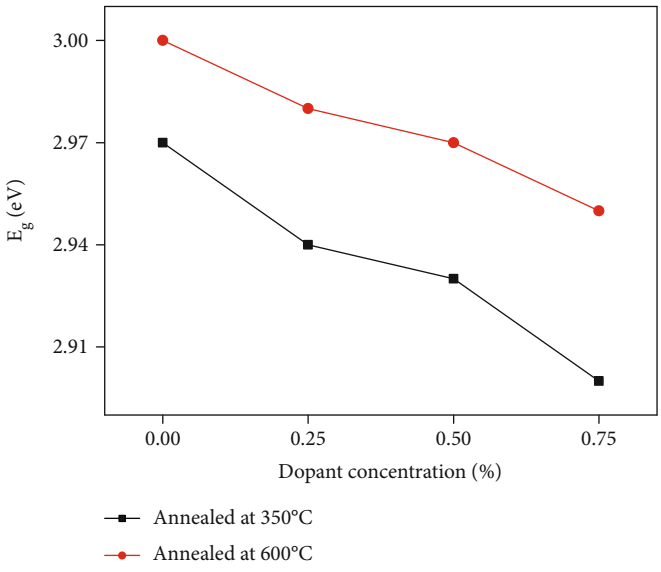

Figure 6: Bandgap energy of Al and Cu codoped ZnO (0%, 0.25%, 0.5%, and 0.75%) annealed at 350°C and 600°C.

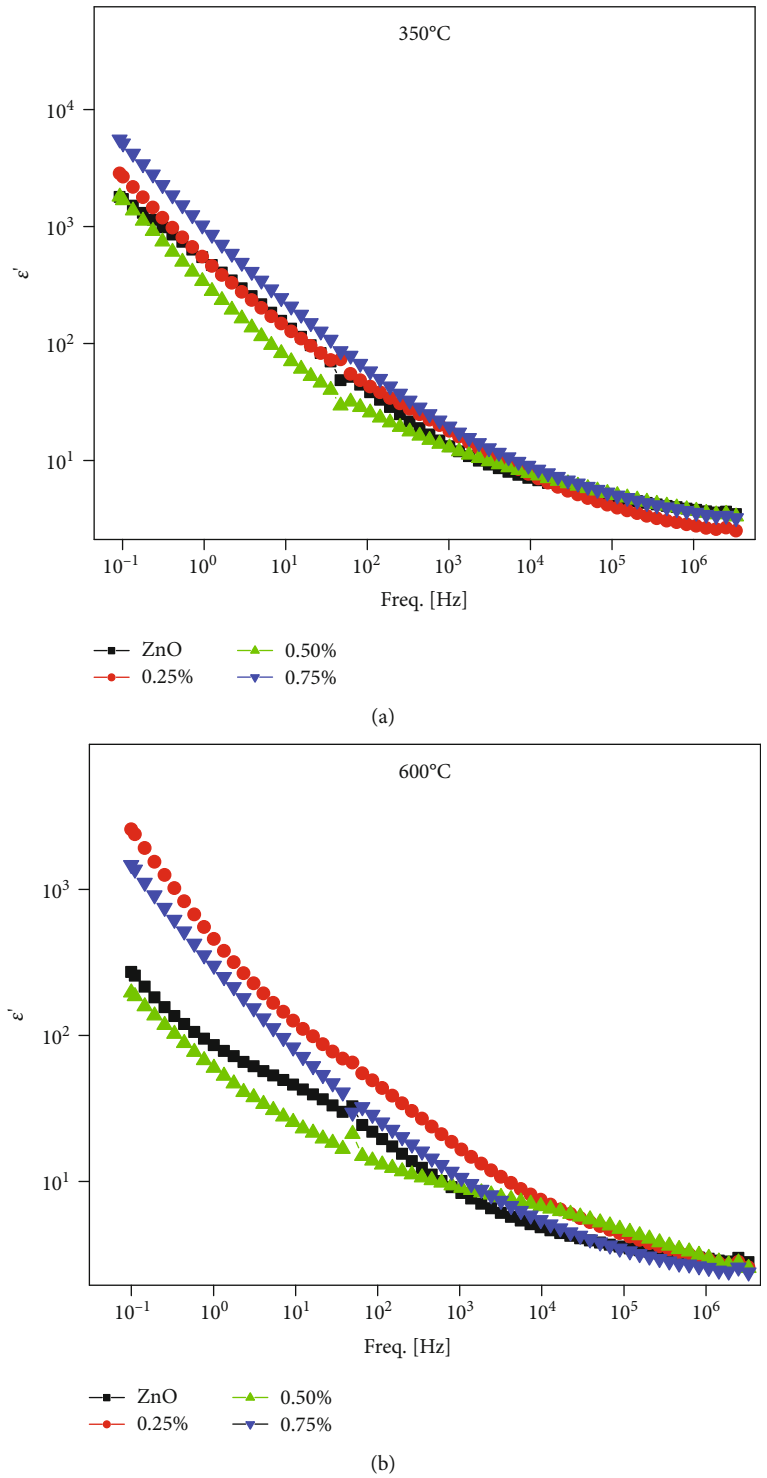

Figure 7: Dielectric constant of Al and Cu codoped ZnO (0%, 0.25%, 0.5%, and 0.75%) annealed at (a) 350°C and (b) 600°C.

annealing temperature specify improvement of the crystalline quality [24]. These results are in accordance with the intensity data explained above.

The data of microstrain as a function of doping concentration and annealing temperature is also presented in Figure 5. An increase in the microstrain was observed when the samples were annealed at 600°C as compared to when annealed at 350°C. Both the series of samples have lesser microstrain as compared to pristine ZnO (0%). A decrease in the value of microstrain was observed with the doping concentration at 600°C; however, the value of microstrain does not show appreciable dependence on doping concentration at 350°C. This decrease in the microstrain might be linked with varied defect chemistry of the samples with

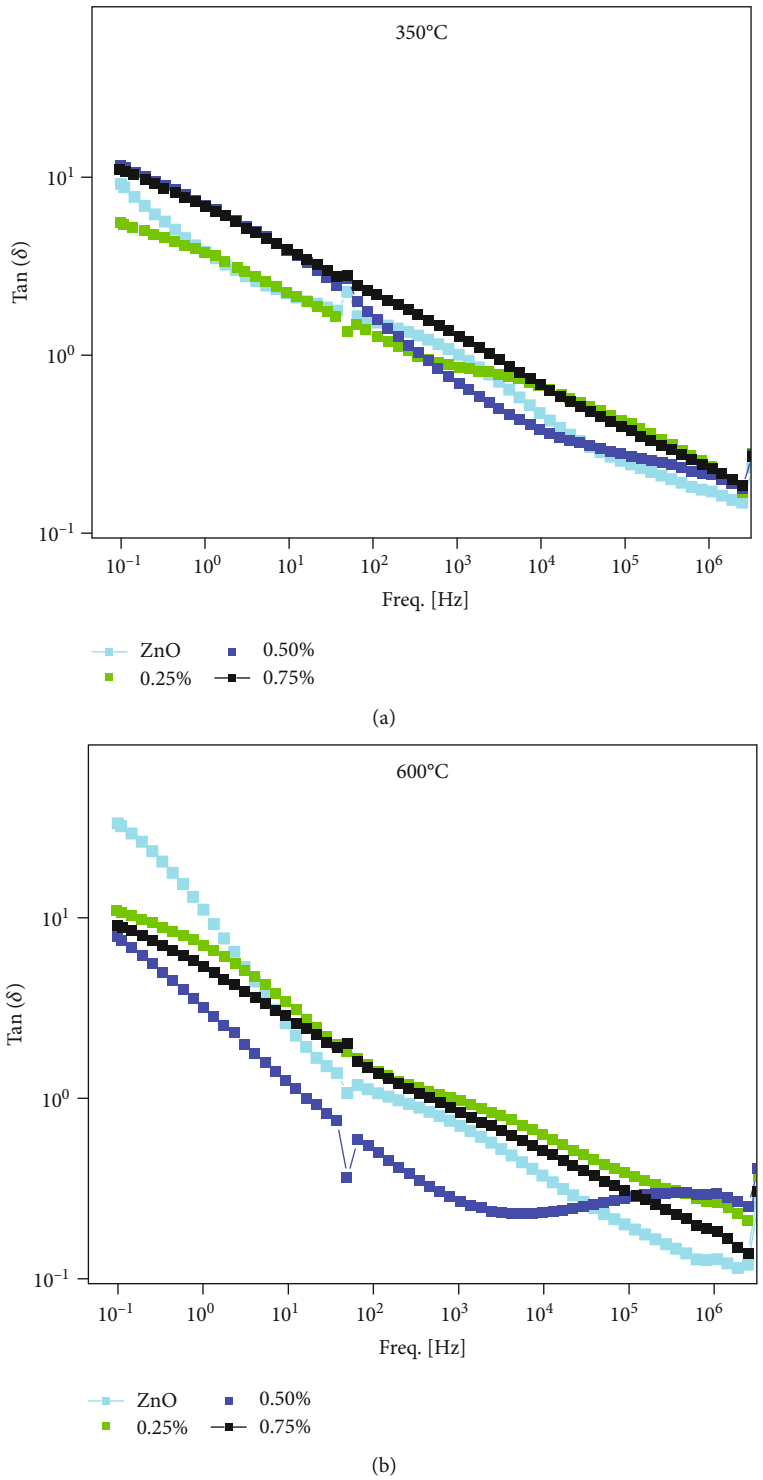

Figure 8: Tangent loss as a function of frequency for Al and Cu codoped ZnO (0%, 0.25%, 0.5%, and 0.75%) annealed at (a) 350°C and (b) 600°C.

doping at different temperatures [24]. Furthermore, all the samples showed positive values of microstrain which is indicative of intrinsic tensile strain [25].

The bandgap energy (E_g) of all samples was calculated using diffused reflectance spectroscopy. Figure 6 shows the bandgap of Al and Cu codoped ZnO at different annealing temperatures and doping concentrations. There is a visible decrease in the bandgap due to the increase in doping concentration at both annealing temperatures, while an increase in the bandgap was observed at a fixed doping concentration with increasing annealing temperature. The doping of an element in a semiconductor host generates localized state within the bandgap of the host. The donor impurities often create these localized states near conduction band edge and

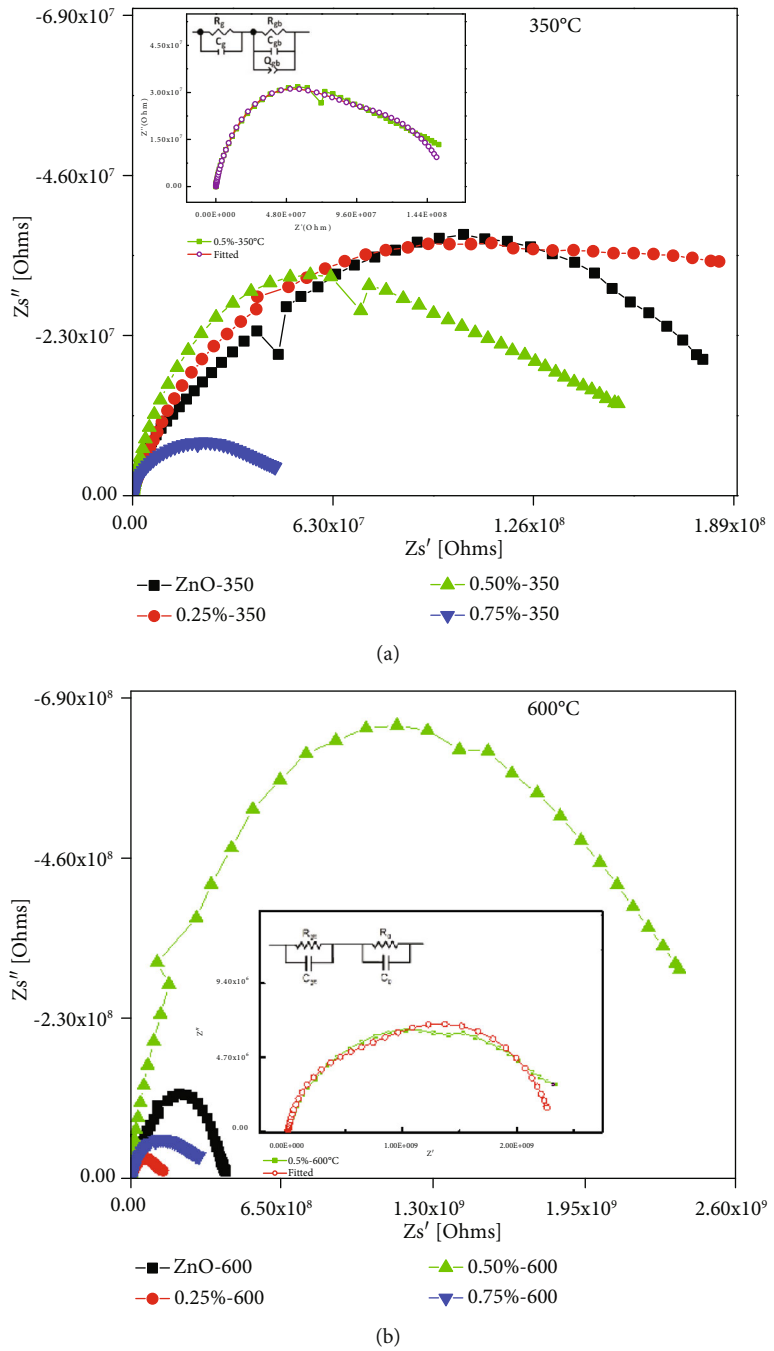

Figure 9: Nyquist plots of Al and Cu codoped ZnO (0%, 0.25%, 0.5%, and 0.75%) annealed at (a) 350°C and (b) 600°C.

acceptor impurity near valence band edge. The increase in doping concentration of donor and acceptor impurity raises the number of these localized states which results in continuum impurity band formation above valence band edge and below conduction band edge [26]. The bandgap narrowing in these samples with doping might be due to creation of these localized states in the bandgap near the conduction band and valence band edge, respectively [24]. Hence, bandgap decreases with an increase in doping concentration. The increase in bandgap with annealing has been linked with the increase of crystallite size upon annealing at higher temperatures [27]. The energy levels in semiconductors are dependent on the degree of structural order–disorder in the lattice [28]. Therefore, the increase of structural organization in nanoceramic leads to a reduction of the intermediary energy levels which consequently increases E_g.

Impedance spectroscopy was performed on these samples. Figures 7(a) and 7(b) show the real part of dielectric constant (ε') as a function of frequency at annealing temperature of 350°C and 600°C, respectively. All the doped and pristine ZnO samples at both annealing temperatures showed relatively high value of ε' at low frequencies which

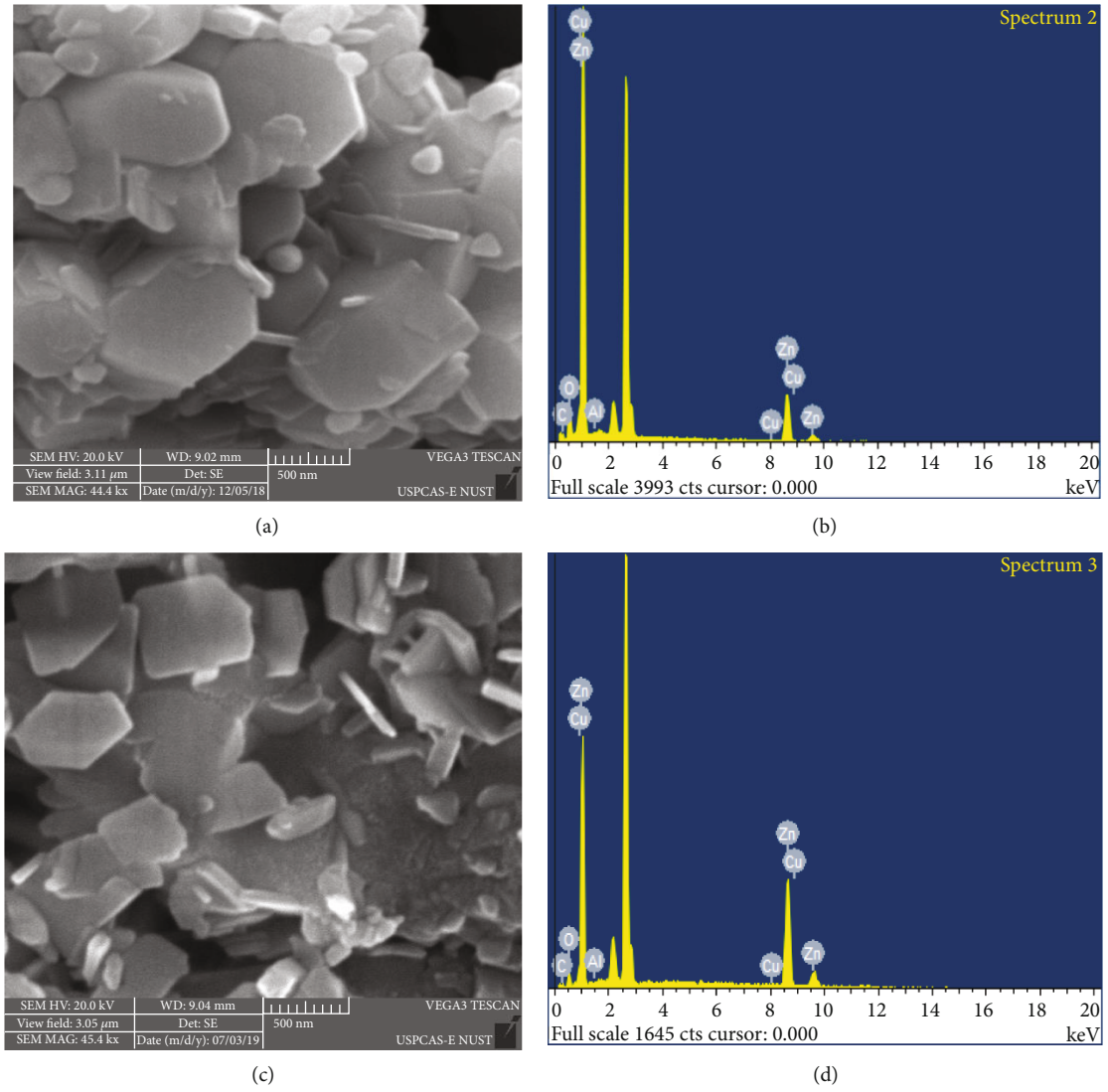

Figure 10: (a, c) Show SEM micrographs of 0.5% Al and Cu codoped ZnO annealed at 600°C and 350°C, respectively. EDX spectrum of 0.5% Al and Cu codoped ZnO annealed at 600°C and 350°C is shown in (b) and (d), respectively.

decreases with increase in frequency. The decrease in ε' with respect to frequency can be attributed to the lagging of carriers as they find it difficult to reach the grain boundaries [29]. This mechanism is common in metal oxides and referred as frequency dispersion. The Maxwell-Wagner interfacial model is used to explain the dielectric behavior of transparent metal oxides as they are composed of conducting grains differentiated by less-conducting grain boundaries. When a field is applied at lower frequencies, the charge carriers could easily pass through the grains, but at grain boundaries, they accumulate. This process is defined as high interfacial polarization which leads to high dielectric constant [30]. At high frequencies, these charge carriers fail to respond to applied frequency which results in the diminishment of interfacial polarization. The only types of polarization that sustain high applied AC frequency are electronic and ionic polarization. Therefore, a reduction in the value of ε' with frequency was observed.

Tangent loss of pristine and the codoped ZnO at both annealing temperatures was also studied. The data is shown in Figures 8(a) and 8(b). In all the samples, tangent loss was found to be decreasing as the frequency was increased. This decrease in tangent loss with frequency is attributed to the release of space charges trapped at grain boundaries [30]. The trend of tangent loss with frequency can be explained by Koop's theory. 0.5% Al and Cu codoped ZnO which was annealed at 600°C showed the most balanced results with low dielectric loss and high dielectric constant. The value of tangent loss at 100 Hz was found to be 0.53 which further reduced and became constant in the frequency range above 10^3 Hz.

Figures 9(a) and 9(b) show complex impedance plane plots of pristine and Al and Cu codoped ZnO samples at an annealing temperature of 350°C and 600°C. The inset in each figure shows the best fitted simulated results of the equivalent circuit along with experimental data. Straight

lines along real and imaginary axis show pure resistive and pure capacitive behavior, respectively [31]. A parallel combination of resistance (R) and capacitance (C) makes a semicircle. Therefore, two RC parallel circuits connected in series describe contribution of two semicircles: one in the lower and other in the higher frequency range, in the Nyquist plot (Figures 9(a) and 9(b)) of these samples indicating two types of relaxation processes. In metal oxide, the grain boundaries are highly resistive because of the nonstoichiometric distribution of oxygen, spin charge reflection, and dangling bonds. These highly resistive layers have large capacitance due to their very thin size [32]. Therefore, high resistance and high capacitance of grain boundaries lead to a higher time constant [18]. Thus, the semicircle at low-frequency range corresponds to grain boundaries and that at higher frequency shows contribution due to grains in each sample. The electrode contribution was not observed in any of these samples.

To investigate morphology, grain growth, and porosity in 0.5% Al and Cu codoped ZnO samples annealed at 350°C and 600°C, detailed high-resolution scanning electron microscopy (SEM) was performed as shown in Figures 10(a) and 10(c). SEM surface micrographs confirm that substitution did not cause any prominent change in the microstructure of the sample. Annealing at high temperature leads to the formation of large structures at the cost of diffusion of tiny particles into surrounding particles. The pores between particles are difficult to escape during annealing process. Beyond the critical porosity values, pores start to be connected to one another thereby forming continuous paths and turn into open pores. The increased number of open pores is associated with decreased amount of grain-to-grain connection. The SEM micrograph demonstrates very good grain-to-grain contact with a minimum number of isolated pores [33]. This indicates the presence of isolated closed pores dispersed in ceramic bulk. The intimate contact, in the SEM images, between ZnO grains should produce promising electron transportation properties in the sample.

To find out the possible existence of metal cluster and foreign elements at grain and grain boundaries, we have also done energy-dispersive X-ray (EDX) spectroscopy analysis at different areas of grain and grain boundaries of all the annealed ZnO samples (Figures 10(b) and 10(d)). The EDX analysis on the sintered samples reveals only zinc and oxygen atoms belonging to the native ZnO matrix. The dust-like particles on the surface of each micrograph also belong to the ZnO and have nothing to do with impurity atoms. Within the detection limit of EDX, we could not observe any foreign atom or metal clustering at grains and grain borders of all pristine samples of ZnO annealed at different temperatures.

4. Conclusion

In summary, pristine and Cu and Al codoped ZnO nanoparticles were synthesized using the coprecipitation method to investigate the effect of doping and annealing temperature on the structural, morphological, and dielectric properties. XRD results showed that all the samples have a wurtzite structure with no secondary phase. The increase in doping concentration led to deterioration in crystalline quality, while annealing at high temperature improved crystallinity. The microstrain in the lattice decreased with doping due to varied defect chemistry. Bandgap narrowing was noticed in these samples upon doping due to the generation of localized defect level inside the bandgap, whereas the samples annealed at higher temperature showed bandgap widening due to reduction in intermediate level because of enhanced structural organization. Dielectric characterization of the samples disclosed interfacial polarization at lower frequencies which diminshes at higher frequencies. The appearance of semicircular arcs in the impedance complex plane plots confirmed the contribution of grains and grain boundaries and presence of different relaxation processes in these samples. Adding both donor and acceptor ion simultaneously in ZnO resulted in the decreased dielectric loss of sample materials. However, 0.5% Al, Cu codoped ZnO annealed at 600°C showed the most balanced results with low dielectric loss and high dielectric constant. Furthermore, SEM results confirmed good grain-to-grain contact with a minimum number of isolated pores. This study has provided a unique way to tailor dielectric properties of ZnO which has remarkable application in next-generation supercapacitors for energy storage applications.

Data Availability

The corresponding author should be contacted to get data. The contact details of the corresponding author are as follows: Dr. Fahad Azad, School of Natural Sciences, National University of Sciences and Technology, Islamabad, Pakistan (fahad.azad@sns.nust.edu.pk).

Additional Points

(i) Impedance analysis of donor (Al)/acceptor (Cu) codoped ZnO nanoparticles, (ii) effect of thermal annealing on the structural and dielectric properties (350–600°C), and (iii) optimized concentration of donor and acceptor doping found useful for superior dielectric properties.

Conflicts of Interest

The authors declare that they have no conflicts of interest.

Acknowledgments

We would like to thank Dr. Muhammad Younas (late) who died of COVID-19. His help in the data collection and result interpretation is highly appreciated.

References

[1] M. Buscaglia, M. Viviani, V. Vuscaglia et al., "High dielectric constant and frozen macroscopic polarization in dense nanocrystallineBaTiO3ceramics," *Physical Review B*, vol. 73, no. 6, article 064114, 2006.

[2] J. Wu, C.-W. Nan, Y. Lin, and Y. Deng, "Giant Dielectric Permittivity Observed in Li and Ti Doped NiO," *Physical Review Letters*, vol. 89, no. 21, article 217601, 2002.

[3] M. A. Subramanian, D. Li, N. Duan, B. A. Reisner, and A. W. Sleight, "High Dielectric Constant in ACu3Ti4O12 and ACu3-Ti3FeO12 Phases," *Journal of Solid State Chemistry*, vol. 151, no. 2, pp. 323–325, 2000.

[4] W. Hu, Y. Liu, R. L. Withers et al., "Electron-pinned defect-dipoles for high-performance colossal permittivity materials," *Nature Materials*, vol. 12, no. 9, pp. 821–826, 2013.

[5] S. Sarkar, P. K. Jana, and B. K. Chaudhuri, "Colossal internal barrier layer capacitance effect in polycrystalline copper (II) oxide," *Applied Physics Letters*, vol. 92, no. 2, article 022905, 2008.

[6] H. Ogihara, C. A. Randal, and S. Troiler-McKinstry, "High-energy density capacitors utilizing 0.7 BaTiO3–0.3 BiScO3-Ceramics," *Journal of the American Ceramic Society*, vol. 92, no. 8, pp. 1719–1724, 2009.

[7] C. C. Homes, T. Vogt, S. M. Shapiro, S. Wakimoto, and A. P. Ramirez, "Optical response of high-dielectric-constant perovskite-related oxide," *Science*, vol. 293, no. 5530, pp. 673–676, 2001.

[8] S. Krohns, P. Lunkenheimer, S. Meissner et al., "The route to resource-efficient novel materials," *Nature Materials*, vol. 10, no. 12, pp. 899–901, 2011.

[9] J. Dumas, C. Schlenker, J. Marcus, and R. Buder, "Nonlinear Conductivity and Noise in the Quasi One-Dimensional Blue BronzeK0.30MoO3," *Physical Review Letters*, vol. 50, no. 10, pp. 757–760, 1983.

[10] Y. Q. Wu, X. Zhao, J. L. Zhang, W. B. Su, and J. Liu, "Huge low-frequency dielectric response of (Nb,In)-doped TiO2ceramics," *Applied Physics Letters*, vol. 107, no. 24, article 242904, 2015.

[11] J. L. Li, F. Li, Y. Y. Zhuang et al., "Microstructure and dielectric properties of (Nb + In) co-doped rutile TiO2ceramics," *Journal of Applied Physics*, vol. 116, no. 7, article 074105, 2014.

[12] C. J. Raj, G. Paramesh, B. S. Prakash, K. R. S. P. Meher, and K. B. R. Varma, "Origin of giant dielectric constant and conductivity behavior in Zn1−xMgxO (0≤x≤ 0.1) ceramics," *Materials Research Bulletin*, vol. 74, pp. 1–8, 2016.

[13] D. Huang, Z. Liu, Y. Li, and Y. Liu, "Colossal permittivity and dielectric relaxation of (Li, In) Co-doped ZnO ceramics," *Journal of Alloys and Compounds*, vol. 698, pp. 200–206, 2017.

[14] X. H. Li, L. Xu, L. Liu et al., "High pressure treated ZnO ceramics towards giant dielectric constants," *Journal of Materials Chemistry A*, vol. 2, no. 39, pp. 16740–16745, 2014.

[15] C. Luo, L. P. Ho, F. Azad et al., "Sb-related defects in Sb-doped ZnO thin film grown by pulsed laser deposition," *Journal of Applied Physics*, vol. 123, no. 16, p. 161525, 2018.

[16] M. Pal, U. Pal, J. Jiménez, and F. Pérez-Rodríguez, "Effects of crystallization and dopant concentration on the emission behavior of TiO2:Eu nanophosphors," *Nanoscale Research Letters*, vol. 7, no. 1, p. 1, 2012.

[17] V. Kumar, N. Singh, R. Mehra, A. Kapoor, L. Purohit, and H. Swart, "Role of film thickness on the properties of ZnO thin films grown by sol-gel method," *Thin Solid Films*, vol. 539, pp. 161–165, 2013.

[18] R. R. Hake, "UPPER-CRITICAL-FIELD LIMITS FOR BULK TYPE-II SUPERCONDUCTORS," *Applied Physics Letters*, vol. 10, no. 6, pp. 189–192, 1967.

[19] N. Felemban, O. M. Aldossary, and V. E. Lembessis, "Atomic mirrors for aΛ-type three-level atom," *J Phys B At Mol Opt Phys*, vol. 47, no. 18, article 185005, 2014.

[20] M. Acosta-Humánez, L. Montes-Vides, and O. Almanza-Montero, "Sol-gel synthesis of zinc oxide nanoparticle at three different temperatures and its characterization via XRD, IR and EPR," *Dyna (Medellin)*, vol. 83, no. 195, pp. 224–228, 2016.

[21] F. Mikailzade, H. Türkan, F. Önal, M. Zarbali, A. Göktaş, and A. Tumbul, "Structural and magnetic properties of polycrystalline Zn1−xMnxO films synthesized on glass and p-type Si substrates using Sol–Gel technique," *Applied Physics A: Materials Science & Processing*, vol. 127, no. 6 article 408, 2021.

[22] W. S. Ni, Y. J. Lin, C. J. Liu, Y. W. Yang, and L. Horng, "Luminescence, structural and ferromagnetic properties of Zn1 −xMnxSy films for different manganese contents," *Journal of Alloys and Compounds*, vol. 556, pp. 178–181, 2013.

[23] X. Guo, Y. Liu, Y. Yang et al., "Effective visible-light excited charge separation in all-solid-state Ag bridged BiVO4/ ZnIn2S4 core-shell structure Z-scheme nanocomposites for boosting photocatalytic organics degradation," *Journal of Alloys and Compounds*, vol. 887, article 161389, 2021.

[24] S. Thakur, N. Sharma, A. Varkia, and J. Kumar, "Structural and optical properties of copper doped ZnO nanoparticles and thin films," *Advances in Applied Science Research*, vol. 5, no. 4, p. 18, 2014.

[25] A. Tumbul, A. Göktaş, M. Z. Zarbali, and F. Aslan, "Structural, morphological and optical properties of the vacuum-free processed CZTS thin film absorbers," *Mater Res Express*, vol. 5, no. 6, article 066408, 2018.

[26] S. S. Kushvaha, M. S. Kumar, M. Maheshwari, A. K. Shukla, P. Pal, and K. K. Maurya, "Structural and electronic properties of epitaxial GaN layer grown on sapphire (0001) using laser molecular beam epitaxy," *Mater. Res. Exp.*, vol. 1, no. 3, article 035903, 2014.

[27] A. Goktas, F. Aslan, and A. Tumbul, "Nanostructured Cu-doped ZnS polycrystalline thin films produced by a wet chemical route: the influences of Cu doping and film thickness on the structural, optical and electrical properties," *Journal of Sol-Gel Science and Technology*, vol. 75, no. 1, pp. 45–53, 2015.

[28] J. Dai, Z. Suo, Z. Li, and S. Gao, "Effect of Cu/Al doping on electronic structure and optical properties of ZnO," *Results in Physics*, vol. 15, article 102649, 2019.

[29] R. Muccillo, E. N. S. Muccillo, and M. Kleitz, "Densification and enhancement of the grain boundary conductivity of gadolinium-doped barium cerate by ultra fast flash grain welding," *Journal of the European Ceramic Society*, vol. 32, no. 10, pp. 2311–2316, 2012.

[30] R. Muccillo, "Impedance spectroscopy analysis of zirconia:8 mol% yttria solid electrolytes with graphite pore former," *Journal of Materials Research*, vol. 24, no. 5, pp. 1780–1784, 2009.

[31] A. S. Kavasoglu, N. Kavasoglu, and S. Oktik, "Simulation for capacitance correction from Nyquist plot of complex impedance- voltage characteristics," *Electronics Letters*, vol. 52, no. 6, pp. 990–996, 2008.

[32] M. Younas, L. L. Zou, M. S. S. C. Nadeem et al., "Impedance analysis of secondary phases in a Co-implanted ZnO single crystal," *Physical Chemistry Chemical Physics*, vol. 16, no. 30, pp. 16030–16038, 2014.

[33] T. Pralhad and K. Rajendrakumar, "Study of freeze-dried quercetin–cyclodextrin binary systems by DSC, FT-IR, X-ray diffraction and SEM analysis," *Journal of pharmaceutical and biomedical analysis*, vol. 34, no. 2, p. 333, 2004.

Hindawi
Journal of Nanomaterials
Volume 2021, Article ID 9410074, 12 pages
https://doi.org/10.1155/2021/9410074

Research Article

Doped Nanostructured Manganese Ferrites: Synthesis, Characterization, and Magnetic Properties

Sami-ullah Rather,[1] **Usman Saeed**,[1] **Abdulrahim Ahmad Al-Zahrani**,[1] **Hisham S. Bamufleh**,[1] **Hesham Abdulhamed Alhumade**,[1] **Aqeel Ahmad Taimoor**,[1] **O. M. Lemine**,[2] **Arshid Mahmood Ali**,[1] **Belal Al Zaitone**,[1] **and Muhammad Mahmud Alam**[1]

[1]*Department of Chemical and Materials Engineering, King Abdulaziz University, P.O. Box 80204 Jeddah 21589, Saudi Arabia*
[2]*Physics Department, College of Sciences, Imam Mohammad Ibn Saud Islamic University (IMSIU), Riyadh, Saudi Arabia*

Correspondence should be addressed to Sami-ullah Rather; rathersami@kau.edu.sa

Received 23 August 2021; Revised 24 November 2021; Accepted 30 November 2021; Published 24 December 2021

Academic Editor: Filippo Giubileo

Nanocrystalline aluminum-doped manganese ferrite was synthesized by facile thermal treatment method. Nanostructure-doped ferrite with crystalline size that ranged between 3.71 and 6.35 nm was characterized via X-ray diffraction (XRD), scanning electron microscopy (SEM), X-ray photoelectron spectroscopy (XPS), and vibrating-sample magnetometry (VSM). The Scherrer and Williamson-Hall hypothesis techniques were utilized to determine lattice constants and strain. Various types of structural properties including octahedral and tetrahedral site radius, bond lengths and angles, hopping parameter, oxygen positional parameters, site bonds, and edge lengths were determined from XRD spectrum analysis. Discrepancy in the hypothetically expected angle indicates improvement of A-B superexchange intercommunication. Furthermore, magnetic-hysteresis (M-H) and XPS analysis support the claim of enhancement. The presence of the ionic nature of iron and manganese in ferrite is Fe^{II}, Fe^{III}, Mn^{II}, and Mn^{IV} as revealed by the results of XPS. Moreover, XPS assists in an excellent way to understand the properties such as configuration, chemical nature, and average inversion degree of doped ferrite samples. The spin noncollinearity and exquisite interaction amid the sublattice are responsible for the decrease in the saturation and remnant magnetization determined from the hysteresis loop at ambient temperature with maximum magnetic field of 1.8 T.

1. Introduction

The transition metal-oriented nanoferrites which consist of unique structural, electrical, thermal, and magnetic characteristics are utilized for various types of engineering and biomedical applications. Nanostructure ferrites are used in different types of biological applications such as X-ray diagnosis, drug delivery, hyperthermia, and magnetic resonance imaging (MRI) [1–4]. Moreover, nanocrystalline spinel ferrites possess a variety of characteristics which are applied in the field of electromagnetic interference (EMI), circuit-based electronic, pigments, sensors, radar systems, motors, and inductors [5–12]. Manganese ferrite ($MnFe_2O_4$) nanoparticles (NPs) with other ferrites are considered as a crucial tool for biomedical applications particularly for enhancing efficiency of magnetic resonance imaging, hyperthermia, and drug delivery [13]. The properties such as facile preparation, proper saturation magnetization, inflated Curie temperature, high coercivity, and redundant anisotropic constant make manganese NPs an exceptional contender for biological applications [14, 15].

Generally spinel-based ferrites are represented by the specification AB_2O_4, where A and B indicates divalent and trivalent cations. Ferrites exhibit different types of unit cell with eight formula units in each cell. The oxygen anions with larger size and metal cations with smaller size occupies face-centered cubic (fcc) and interstitial sites, respectively. The magnetite (Fe_3O_4), a form of iron oxide is the primary building block of most of the ferrites [16]. The $(M^{2+}{}_{1-\delta}Fe^{3+}{}_{\delta})[M^{2+}{}_{\delta}Fe^{3+}{}_{2-\delta}]O_4$ formula provides general information

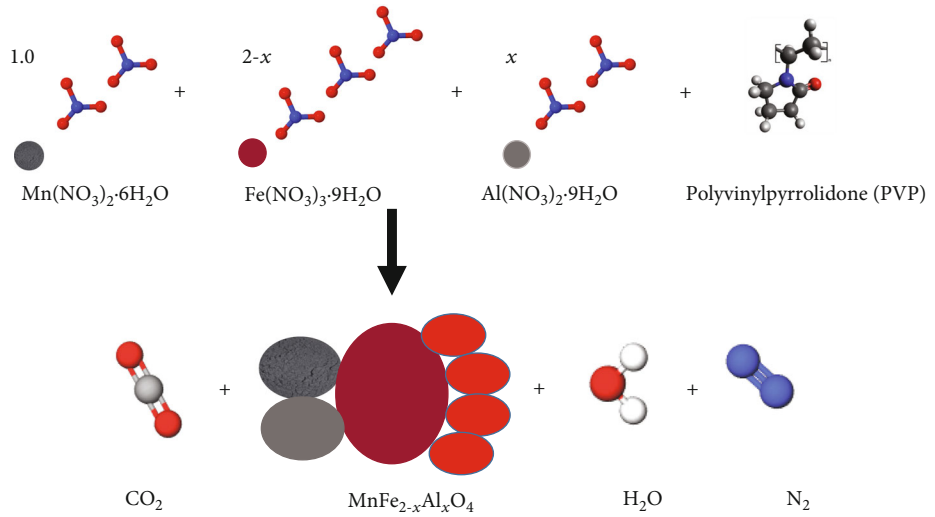

Figure 1: Schematic design of the reaction arrangement of the synthesis of $MnFe_{2-x}Al_xO_4$.

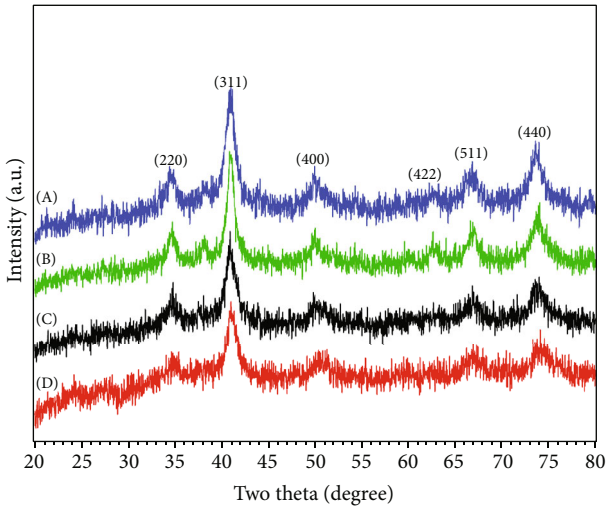

Figure 2: XRD patterns of $MnFe_{2-x}Al_xO_4$. Profiles a, b, c, and d refer to Al content of $x = 0.0$, 0.3, 0.6, and 0.9, respectively.

related to sites and degree of inversion (δ). The () and [] bracket represents tetrahedral and octahedral sections and "δ" furnishes ferrite nature in terms of whether the structure is normal, inverse or random. When $\delta = 0$, the formula is expressed as $(M^{2+})[Fe_2{}^{3+}]O_4$, and the ferrite is called normal spinel ferrite. When $\delta = 1$, the formula is expressed as $(Fe^{3+})[M^{2+}Fe^{3+}]O_4$, and the ferrite is called inverse spinel ferrite. When $0 < \delta < 1$, such as $\delta = 0.3$, 0.6, or 0.9, the ferrite is called as mixed spinel ferrite. When $\delta = 0.3$, the formula is expressed as $(M_{0.7}{}^{2+}Fe_{0.3}{}^{3+})[M_{0.3}{}^{2+}Fe_{1.7}{}^{3+}]O_4{}^{2-}$ [17]. Zinc ferrite ($ZnFe_2O_4$), a normal spinel, where Zn^{2+} cations represent as tetrahedral site and Fe^{3+} cations as octahedral sites leads to the formula as $(Zn^{2+})[Fe_2{}^{3+}]O_4$ [18]. Cobalt ferrite ($CoFe_2O_4$) is an inverse ferrite, where Co^{2+} prefers octahedral and Fe^{3+} prefers uniform placement in octahedral and tetrahedral sites [19]. Manganese ferrite ($MnFe_2O_4$) is a mixed ferrite, where Mn^{2+} and Fe^{3+} prefer both tetrahedral and octahedral bonding sites [20]. Structural, magnetic, and optical characteristics of ferrites depends upon tetrahedral and octahedral sites occupied by divalent and trivalent cations [21, 22]. Furthermore, particle size distribution (PSD) also affects optical and magnetic characteristics of spinel ferrites [23, 24].

Ferrite nanoparticles bearing new unique characteristics are prepared by different routes which include high-energy ball milling, solvothermal, coprecipitation, sol-gel method, thermal decomposition, hydrothermal, microemulsion, electrochemical, and laser ablation method [25–33]. It was reported that the crystal structure, size, and magnetic properties of ferrites including manganese ferrite are influenced by calcinations, reaction duration, capping reagent, and pH [34–36]. The preparation methods including thermal decomposition, microemulsion, and coprecipitation affect crystal structure and magnetic properties of ferrites as reported by Gyergyek et al. [37]. Furthermore, it was also reported that different types of the preparation method change cation distribution, composition, and crystallinity among tetrahedral and octahedral sites [37–39]. The lattice parameter and average strain of cobalt ferrites vary with doping of erbium. Furthermore, this variation is due to a large size of Er^{3+} cations as compared to Fe^{3+} ions [40]. Incorporation of Mg into $ZnFe_2O_4$ significantly affects the rearrangement of cation distribution at tetrahedral and octahedral sites [41]. The crystal size of nickel-cobalt spinel changes upon doping of rare-earth metals. Moreover, variation in crystal size is because of blocking of crystal expansion by large size metals. The crystal size and surface area of ferrite are influenced by changing the variation of different types of metals such as La, Zn, Cd, and Ni [27, 40–44].

In this research work, the preparation of mixed spinel ferrite $MnFe_{2-x}Al_xO_4$ $(0 \le x \le 0.9)$ with $(x) = 0.0, 0.3, 0.6,$ and 0.9 via a thermal method in association with capping agent polyvinylpyrrolidone is presented in detail. For mixed doped manganese spinel ferrite preparation, thermal disintegration route was chosen because of distinct accomplishments such as environmental acceptance, cheap, and

Table 1: XRD parameters of $MnFe_{2-x}Al_xO_4$ ($x = 0.0, 0.3, 0.6,$ and 0.9).

Sample name	Lattice parameter a (Å)	Cell volume V $(Å)^3$	Bulk density ρ_m (gm/cm^3)	X-ray density ρ_{x-ray} (gm/cm^3)	Porosity (%)	Crystal size (nm)
$MnFe_2O_4$	8.515	617.380	2.998	4.962	39.580	6.35
$MnAl_{0.3}Fe_{1.7}O_4$	8.512	613.910	2.885	4.775	39.581	5.99
$MnAl_{0.6}Fe_{1.4}O_4$	8.499	605.170	2.772	4.589	39.583	4.47
$MnAl_{0.9}Fe_{1.1}O_4$	8.458	601.120	2.660	4.403	39.586	3.71

persistent reproducibility; however, this process has a few drawbacks which include shape discrepancy and cluster of particles. Detailed characterization analysis of crystal structural parameter, nanostructure morphology, and quantitative assessment and magnetization characteristics of purified and Al-doped manganese mixed ferrite were also reported in this research work.

2. Experimental

2.1. Synthesis. Analytical precursors were used for the synthesis of pure and Al-doped manganese ferrite $MnFe_{2-x}Al_xO_4$ ($x = 0.0, 0.3, 0.6,$ and 0.9) without repeating purification: polyvinylpyrrolidone (PVP) (Alfa Aesar), iron (III) nitrate nonahydrate [$Fe(NO_3)_3{\cdot}9H_2O$] (min. 98%, Sigma-Aldrich), manganese (II) nitrate hexahydrate [$Mn(NO_3)_2{\cdot}6H_2O$] (min. 98%, Sigma-Aldrich), and aluminum nitrate nonahydrate [$Al(NO_3)_3{\cdot}9H_2O$] (min. 98%, Sigma-Aldrich).

In a thermal synthesis process of $MnFe_2O_4$, a solution containing 0.2 mmol (0.0808 g) $Fe(NO_3)_3{\cdot}9H_2O$ and 0.1 mmol (0.0179 g) $Mn(NO_3)_2{\cdot}6H_2O$ was vigorously stirred for 2 h, followed by inclusion of capping agent (PVP) solution. The capping agent solution was synthesized by adding 0.1 g of PVP into 50 ml of deionized water (DI) at 90°C. The mixed solution was vigorously stirred for 2 h at room temperature (RT). The pH of the above solution was determined by litmus paper which was followed by drying at 80°C for 24 h. The dried orange-colored sample was converted into powder and calcinated at 500°C for 4 h to eliminated PVP in order to form pristine $MnFe_2O_4$. A similar method was executed for the preparation of $MnFe_{2-x}Al_xO_4$ ($x = 0.3, 0.6,$ and 0.9). For clarity, hereafter, the Al-doped $MnFe_2O_4$ are referred to as $MnFe_{1.7}Al_{0.3}O_4$, $MnFe_{1.4}Al_{0.6}O_4$, and $MnFe_{1.1}Al_{0.9}O_4$. A graphic reaction design for the synthesis of $MnFe_{2-x}Al_xO_4$ is presented in Figure 1.

2.2. Characterization. Structure of pristine and doped ferrite was determined by the XRD spectrum. The XRD spectrum was achieved using an INEL CPS 180 XRD Equinox 1000 diffractometer assembled with Co-Kα1 emission ($\lambda = 1.789$ Å) and regulated at 40 kV and 30 mA. The analysis was managed in the 2θ range of 10-80° at RT. The nanostructure behavior of samples was investigated by SEM. A wafer-delicate carbon film captivated inner side of a copper framework was used to install nanoparticles present in an ethanol solution. The XPS was operated by employing the SPEC GmbH (Germany) spectrometer at RT. The instrument is assembled with X-ray-bearing dual anode origin SPECS XR-50 Mg-Kα (hn = 1283.6 eV) in the presence of lift-off angle of photoelectrons of 90°. The ferrite samples were converted into pellets, before shifting to a high vacuum chamber. The vacuum was managed at 5×10^{-9} bar, during the operation. In order to perform surface quantification of the ferrite sample, a detailed operating method was employed containing high-resolution spectrum of O1s and C1s. To achieve a high quality XPS spectrum, calibration of the BE scale was performed by BE of C1s peak at 284.6 eV. The Lake Shore 7400 magnetometer VSM that was equipped with a 1.8 Tesla magnet was utilized to determine magnetic properties of ferrite samples at RT. The hysteresis loop of ferrite samples was obtained by plotting magnetization verses magnetic field. Furthermore, to measure remnant magnetization (Mr), saturation magnetization (Ms), and coercivity, magnetic hysteresis loops were utilized.

3. Results and Discussion

Powder XRD pattern results of $MnFe_{2-x}Al_xO_4$ ($0 \le x \le 0.9$) are presented in Figure 2, and profiles a, b, c, and d refer to the content of $x = 0.0, 0.3, 0.6$ and 0.9, respectively. The visibly strong peaks were found between 10 and 80°. The strong peaks shown in Figure 2 are contemplations from the (111), (220), (311), (222), (400), (422), (511), (440), (620), (533), and (444) planes of purified and Al-doped ferrites. All these prominent peaks are associated to Bragg's contemplation of cubic ferrite with space group Fd3m. The nonexistence of other oxide peaks suggests that precursor is free from impurity. The inflation of Al content produces broadened diffraction peaks and simultaneously decreases intensity, which indicates development of nanostructured ferrites. The strong main peak (311) refers to crystallinity of the structure of ferrites. The decrease in crystallite size as the Al content elevates is shown in Table 1. The full width at half-maximum is utilized in the Scherer equation (Equation (1)) to determine crystal size (D). The main peak in the XRD spectrum was employed to calculate crystal size.

$$D = \frac{(0.9\,\lambda)}{(\beta_{hkl}\,Cos\theta)}. \quad (1)$$

X-ray wavelength, FWHM in radians, and Bragg's angle, respectively, refer to λ, β, and θ.

Table 1 shows average crystal size data calculated from Equation (1) and was found to be 6.35, 5.99, 4.47, and 3.71 nm. The capping agent PVP was employed during the synthesis process to avert agglomeration of ferrite particles.

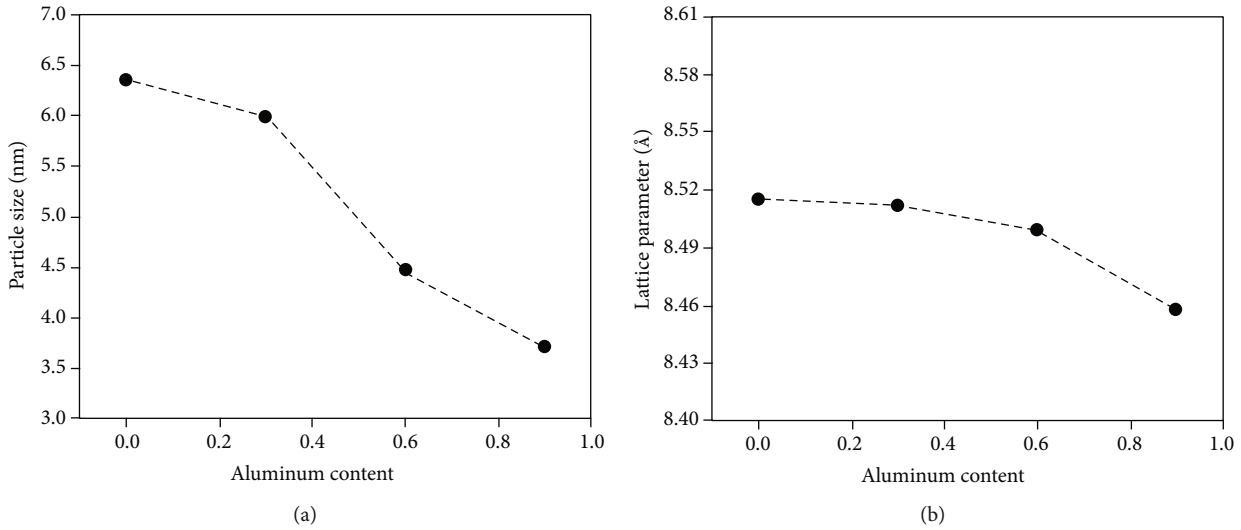

Figure 3: Left and right panel presents alteration in the particle size and lattice parameter with the Al content (x) in manganese ferrite.

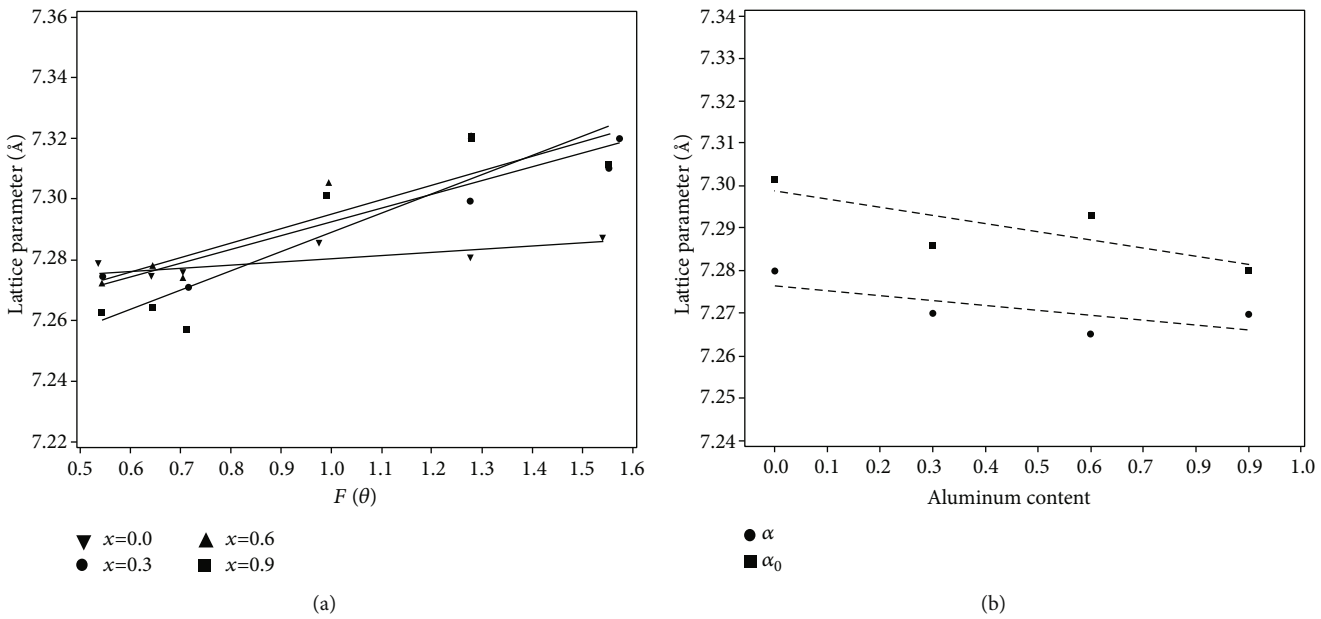

Figure 4: (a) The Nelson-Riley representation for $MnFe_{2-x}Al_xO_4$ and (b) the interactions of the theoretical and experimental lattice constants for $MnFe_{2-x}Al_xO_4$ ($x = 0.0, 0.3, 0.6$, and 0.9).

The absence of PVP creates aggregation of particles owing to high energy of small particles as reported in the Ostwald ripening process [45]. Table 1 confirms the variation in lattice parameter, X-ray density, bulk density, cell volume, and porosity as the content of nonmagnetic Al changes. Furthermore, increasing Al concentration decreases lattice constant parameters, density, and particle size as shown in Figure 3. Dessai et al. also observed that increasing nonmagnetic Al^{3+} content in manganese ferrite decreases lattice parameter and density [46].

The Nelson-Riley function $F(\theta)$ for each reflection of $MnFe_{2-x}Al_xO_4$ was calculated by using the following relation:

$$F(\theta) = \frac{1}{2}\left(\frac{\cos^2\theta}{\sin\theta} + \frac{\cos^2\theta}{\theta}\right). \quad (2)$$

Figure 4(a) shows Nelson-Riley function of nanocrystalline $MnFe_{2-x}Al_xO_4$. Diffraction angle from 10 to 80° was utilized to determine lattice parameters "a_o" by extrapolating $F(\theta)$. True lattice value "a_o" and average value "a" variation is shown in Figure 4(b). It is visible from Figure 4(b) that little disparity between true value lattice constant "a_o" and the

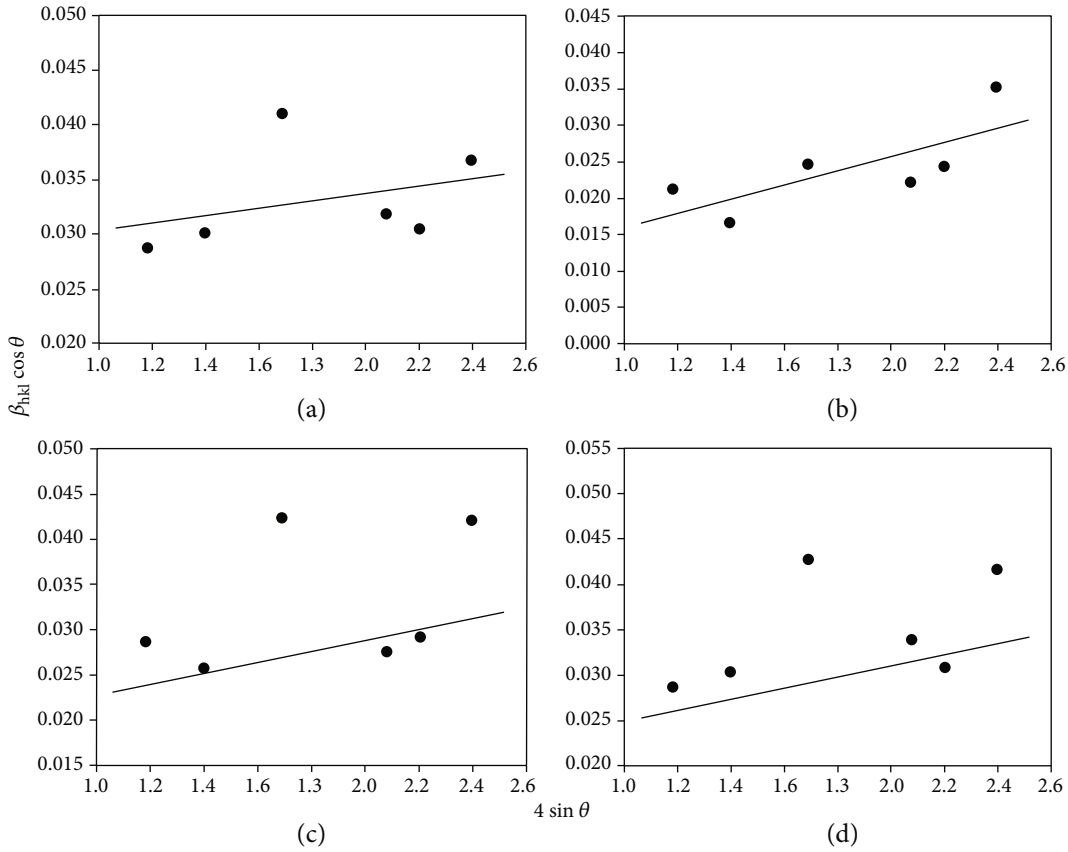

FIGURE 5: Profile of "$\beta_{hkl}\cos\theta$" vs "$4\sin\theta$" of $MnFe_{2-x}Al_xO_4$ ($x = 0.0, 0.3, 0.6,$ and 0.9). (a–d) are associated to diffraction spectrums of different Al concentrations.

average value lattice constant "a" existed. Moreover, average value lattice constant "a" is slightly more than true value lattice constant "a_o." Both true and average value lattice constants reduces as the content of Al elevates. The reduction of both lattice constants may be due to change in ionic radius between Al^{3+} (0.51 Å) and Fe^{3+} (0.67 Å). According to the literature, it is obvious that replacement of highly magnetic Fe^{3+} ions by nonmagnetic Al^{3+} reduces lattice constant as Al content elevates [46, 47]. Lattice constant reduces from 8.515 Å to 8.458 Å as the Al content in the doped ferrite increases is shown in Figure 3 (right panel). The reduction in crystallite size from 6.35 nm to 3.71 nm presented in Figure 3 (left panel) may be due to substitution of larger size Fe^{3+} ions by smaller size Al^{3+} ions. High porosity and lattice constant shown in Table 1 are other reasons responsible for crystal size reduction. The parameters a, V, ρ_m, ρ_{x-ray}, and P presented in Table 1 were determined from Equations (3) to (7). These parameters decrease as the Al content increases except for porosity which is due to reduction of crystal size and lattice constant. High porosity as the Al content increases may be due to extra vacancies established by substitution of Fe^{3+} cations by Al^{3+} cations [48].

$$d = \frac{a}{\sqrt{\frac{2}{h^2 + k \quad + l^2}}}, \tag{3}$$

TABLE 2: Average strain of $MnFe_{2-x}Al_xO_4$ ($x = 0.0, 0.3, 0.6,$ and 0.9).

Sample name	Scherrer method $\langle\varepsilon\rangle \times 10^{-3}$	W-H method $\langle\varepsilon\rangle \times 10^{-3}$
$MnFe_2O_4$	10.90	27.10
$MnFe_{1.7}Al_{0.3}O_4$	7.99	6.50
$MnFe_{1.4}Al_{0.6}O_4$	10.75	21.50
$MnFe_{1.1}Al_{0.9}O_4$	11.44	23.60

$$V = a^3, \tag{4}$$

$$\rho_m = \frac{m}{(\pi r^2)h}, \tag{5}$$

$$\rho_{x\text{-ray}} = \frac{ZM}{NV}, \tag{6}$$

$$P = 1 - \frac{\rho_m}{\rho_{x\text{-ray}}}. \tag{7}$$

The strain created by crystal defects and distortions is due to addition of Al in manganese ferrites. The average strain $<\varepsilon>$ of Al-doped manganese spinel was calculated

Table 3: The bond lengths (R_A and R_B) and hopping lengths for tetrahedral and octahedral sites (L_A and L_B), tetrahedral and octahedral bond lengths (d_{Ax} and d_{Bx}), the shared tetrahedral edge length (d_{AxE}), and shared and unshared octahedral edge lengths (d_{BxE} and d_{BxEU}) of $MnFe_{2-x}Al_xO_4$ $(0 \le x \le 0.9)$.

Sample name	Bond length (Å)		Hopping length (Å)		d_{Ax} (Å)	d_{Bx} (Å)	d_{AxE} (Å)	d_{BxE} (Å)	d_{BxEU} (Å)
	R_A	R_B	L_A	L_B					
$MnFe_2O_4$	1.9173	2.0871	2.0870	2.0870	1.9173	2.0870	3.1309	2.8901	3.0118
$MnFe_{1.7}$ $Al_{0.3}O4$	1.9166	2.0863	2.0863	2.0863	1.9167	2.0863	3.1298	2.8890	3.0107
$MnFe_{1.4}$ $Al_{0.6}O4$	1.9137	2.0831	2.0831	2.0831	1.9137	2.0831	3.1250	2.8846	3.0061
$MnFe_{1.1}$ $Al_{0.9}O4$	1.9045	2.0731	2.0731	2.0731	1.9045	2.0730	3.1100	2.8707	2.9916

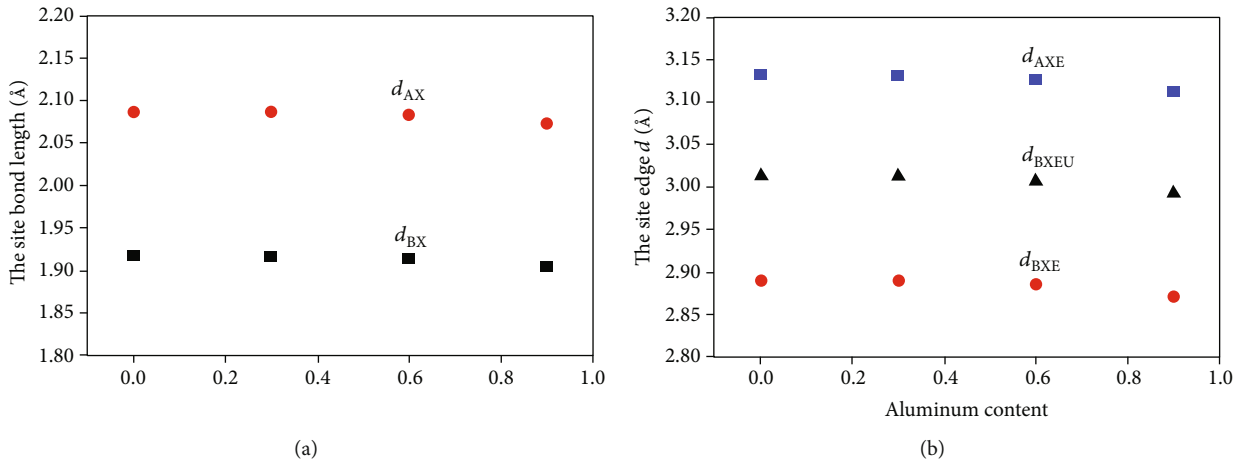

Figure 6: (a) The change in the bond lengths (d_{Ax} and d_{Bx}) and (b) the site edge lengths (d_{AxE}, d_{BxE}, and d_{BxEU}) of $MnFe_{2-x}Al_xO_4$ $(0 \le x \le 0.9)$.

by employing the following equation:

$$\langle \varepsilon \rangle = \frac{\beta_{hkl}}{4 \tan \theta}. \tag{8}$$

Addition of Equations (1) and (8) produces noticed line breadth in the form of Equation (9).

$$\beta_{hkl} = \frac{k\lambda}{D\,Cos\theta} + 4 < \varepsilon > \tan \theta, \tag{9}$$

$$\beta_{hkl} \cos \theta = \frac{k\lambda}{D} + 4 \langle \varepsilon \rangle \sin \theta. \tag{10}$$

Williamson-Hall (W-H) calculations shown above in the form of Equations (9) and (10) were used to calculate crystallite size and average strain. The "$\beta_{hkl} \cos \theta$" verses "4 sin θ" presented in Figure 5 is employed to calculate both the particle size and the strain. The linear fit of the crystal size and strain follows the uniform deformation process, where the strain is assumed as homogeneous in all directions, a property of isotropy. The W-H and Scherer formulas used for the calculation of the average strain were in complete harmony with each other as shown in Table 2.

The bond length of tetrahedral and octahedral sites was affected by the lattice constants which were created by crystal size reduction. The bond lengths shown in Table 3, associated to tetrahedral (R_A) and octahedral bonding sites (R_B) were determined by Equations (11) and (12), where $\delta = u - 0.375$. The R_A and R_B site is the closest gap between A and B with oxygen ions. The higher R_B compared to R_A is the main reason that the Mn^{2+} cation capability is towards O^{2-} anions. The existence of Al^{3+} cations in ferrites reinforces the gap between Fe^{3+} and Al^{3+} cations. The L_A and L_B values shown in Table 3 determined from Equations (13) and (14) refer to hopping lengths and space between magnetic ions present in the tetrahedral and octahedral bonding sites. The change in hopping lengths of tetrahedral and octahedral sites is associated to change in crystal size which is exactly applicable to lattice constants [49]. The ionic radius alteration between Al^{3+} (0.51 Å) and Fe^{3+} (0.67 Å) ions is the other reason associated to change in hopping lengths. The tetrahedral and octahedral bond lengths (d_{Ax} and d_{Bx}), the shared tetrahedral edge length (d_{AxE}), and shared and unshared octahedral edge lengths (d_{BxE} and d_{BxEU}) shown in Table 3 were calculated from Equations (15) to (19). Furthermore, these values shown in Table 3 and Figure 6 suggest reduction as Al content in ferrites increases, therefore indicating complete dominance of the lattice constants and ionic radii [49].

$$R_A = a\sqrt{3}\left(\delta + \frac{1}{8}\right), \tag{11}$$

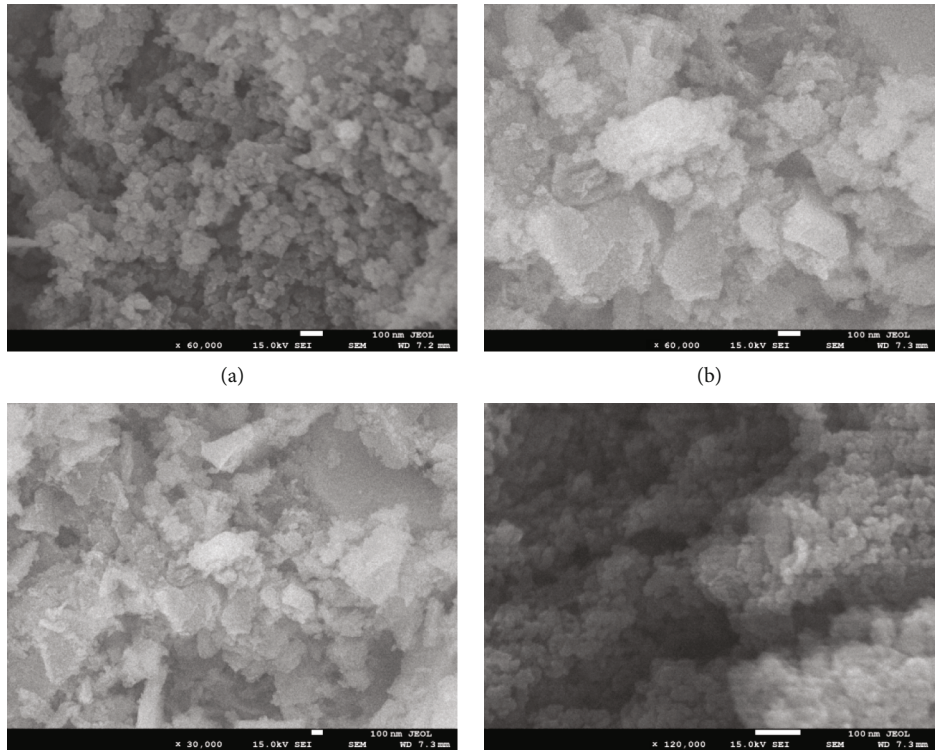

Figure 7: SEM analysis of $MnFe_{2-x}Al_xO_4$ $(0 \le x \le 0.9)$.

Table 4: Comparison of target and actual composition in $MnFe_{2-x}Al_xO_4$.

Target composition	Composition by EDX		
	Mn	Fe	Al
$MnFe_2O_4$	0.88	2.35	
$MnFe_{1.7}Al_{0.3}O_4$	0.98	2.20	0.42
$MnFe_{1.4}Al_{0.6}O_4$	0.99	1.80	0.71
$MnFe_{1.1}Al_{0.9}O_4$	1.03	1.20	1.06

$$R_B = a\left(3\delta^2 - \frac{\delta}{2} + \frac{1}{16}\right), \tag{12}$$

$$L_A = 0.25a\sqrt{3}, \tag{13}$$

$$L_B = 0.25a\sqrt{2}, \tag{14}$$

$$d_{Ax} = a\sqrt{3}\left(u - \frac{1}{4}\right), \tag{15}$$

$$d_{Bx} = a\left[3u^2 - \left(\frac{11}{4}\right)u + \frac{43}{64}\right]^{1/2}, \tag{16}$$

$$d_{AxE} = a\sqrt{2}\left(2u - \frac{1}{2}\right), \tag{17}$$

$$d_{BxE} = a\sqrt{2}(1 - 2u), \tag{18}$$

$$d_{BxEU} = a\left[4u^2 - 3u + \frac{11}{16}\right]^{1/2}. \tag{19}$$

The nanostructure characterization of $MnFe_{2-x}Al_xO_4$ performed by SEM is presented in Figure 7, where (a) corresponds to pure ferrite and (b–d) correlate to Al-doped manganese ferrites. The scale bar for all the samples is 100 nm. The agglomeration of smaller particles is visible in the nanostructured samples of ferrites. The EDX and elemental investigation averaged over different parts of the samples are presented in Table 4.

The XPS measurements shown in Figure 8 were performed to estimate functionalization of ferrite surface with different active groups. Various chemical states A and B associated with ferrite surface states are presented in Figures 8(a)–8(d). The strong peaks existed in the ferrite spectrum of $MnFe_{2-x}Al_xO_4$ $(x = 0.0, 0.3, 0.6, \text{and } 0.9)$ are correlated to Fe, Mn, O, and Al, respectively. The intense signal was adapted to different peaks including Mn 2p, doublet Fe 2p, O 1s, and Al 2p. The Mn 2p is a singlet based at a binding energy (BE) of 641.94 eV. The doublet signal of Mn $2p_{3/2}$ Mn^{2+} octa and Mn $2p_{3/2}$ Mn^{4+} tetra based at BE of 640.89 eV and 642.43 eV are related to Mn $2p_{3/2}$ peak. Similarly, the same trend was detected for Al in the doped sample; however, a peak deviation of ±1 eV was visible. The doublet peak of Fe 2p was deviated from each other by BE 8.45 eV as a result of spin-orbit coupling. The iron $2p_{3/2}$ signals were adapted into three different segments because of the multiplet splitting process. The prominent peaks located

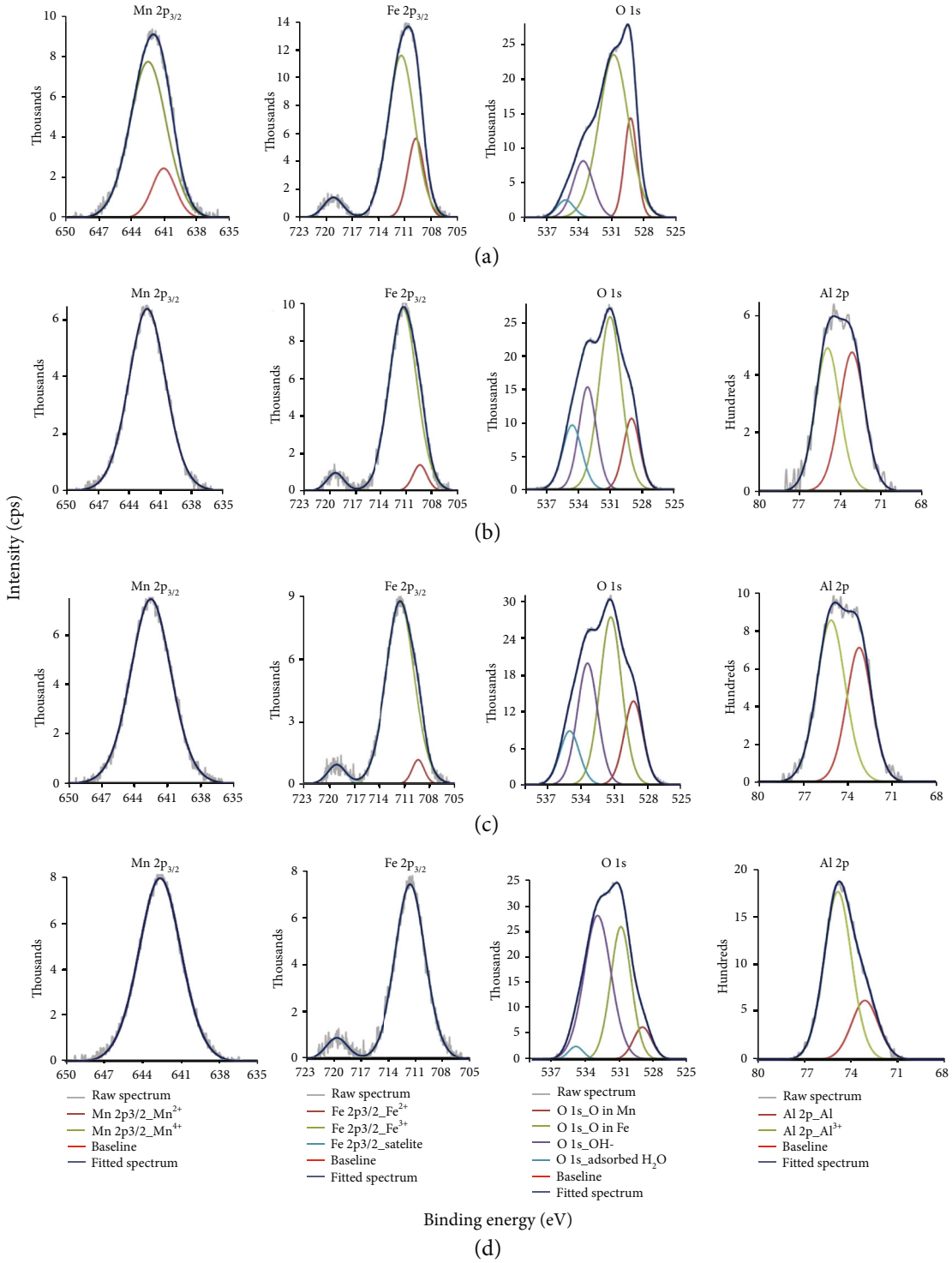

FIGURE 8: XPS spectra of $MnFe_{2-x}Al_xO_4$ ($x = 0.0, 0.3, 0.6$, and 0.9).

at BE 709.59 eV and 711.24 eV are related to Fe $2p_{3/2}$ Fe^{2+} octa and Fe $2p_{3/2}$ Fe^{3+} tetra. The doped samples follow a similar trend with a peak deviation of BE ± 2 eV. The strong peak located at BE 529.88 eV of O is in a multicomponent segment which belongs to the oxide lattice. The remaining less intense peaks of O is based at BE 529.44 eV, 538.99 eV, 533.74 eV, and 535.69 eV which are related to the oxygen bond formation with Fe, Mn, OH, and adsorbed H_2O, respectively. A similar trend for the oxygen peak was also observed in the ferrite doped samples. The Al 2p peak adapted into two prominent peaks located at BE 73.29 and 74.79 eV which are related to octahedral and tetrahedral sites. The Al peak intensity enhances as the Al concentration increases indicating expected substitution of Al^{3+} into

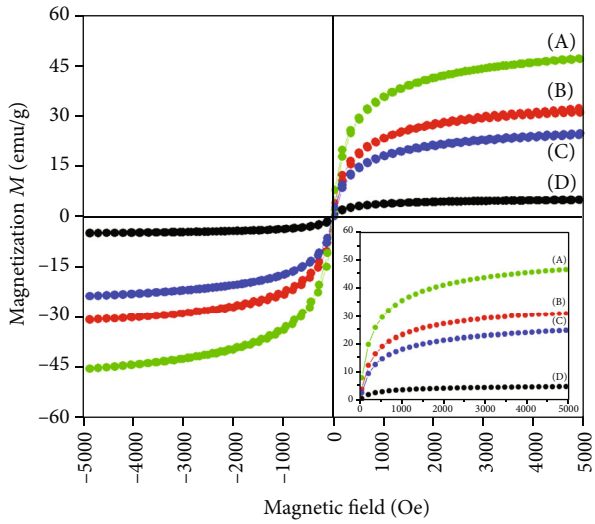

Figure 9: Magnetization curves of $MnFe_{2-x}Al_xO_4$. The inset profile figure shows saturation magnetization. Profiles (a), (b), (c), and (d) refer to Al concentration of $x = 0.0, 0.3, 0.6$, and 0.9, respectively.

Table 5: Coercive field (H_c), remnant magnetization (M_r), saturation magnetization (M_s), experimental molar magnetization (η_{exp}), and squareness ratio (M_r/M_s) determined from hysteresis loops of the ferrite samples.

Sample name	H_c (Oe)	M_r (emu/g)	M_s (emu/g)	η_{exp}	$R = M_r/M_s$
$MnFe_2O_4$	40	5.01	47.32	1.95	0.106
$MnFe_{1.7}Al_{0.3}O_4$	27	1.97	31.90	1.27	0.062
$MnFe_{1.4}Al_{0.6}O_4$	20	1.18	24.71	0.94	0.050
$MnFe_{1.1}Al_{0.9}O_4$	17	0.35	5.02	0.2	0.065

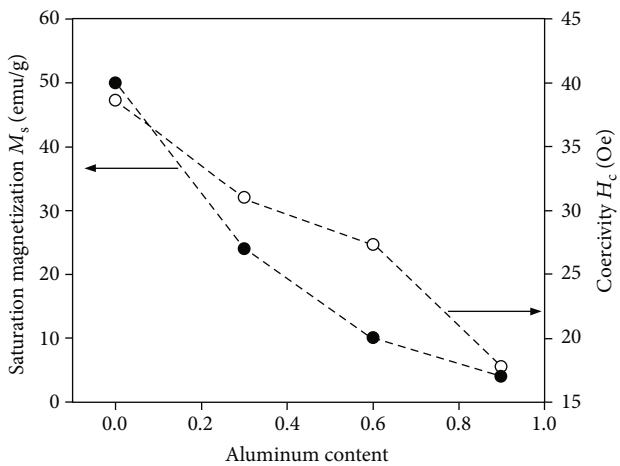

Figure 10: Saturation magnetization and coercivity of $MnFe_{2-x}Al_xO_4$ ($x = 0.0, 0.3, 0.6$, and 0.9).

manganese ferrite. The doping of Al into manganese ferrite responsible for structural and magnetic property variation is the main reason for peak deviation of Mn and Fe in the doped ferrites. The 45% Mn^{2+} ions are located at octahedral sites, and 55% Mn^{4+} ions are based at tetrahedral sites as far as unified intensity of the deconvoluted peaks is concerned. The Mn $2p_{3/2}$ peaks are fitted into two intense peaks located at BE 640.89 eV and 642.43 eV. Moreover, the assessment of Fe^{2+} and Fe^{3+} based at BE 709.59 eV and 711.24 eV is 78% at the octahedral and 22% at tetrahedral bonding sites [50–52]. The substitution formula of $MnFe_{2-x}Al_xO_4$ ($x = 0.0$) could be declared as follows:

$$\left(Mn^{4+}_{0.55}\, Fe^{3+}_{0.45}\right)\left[Mn^{2+}_{0.45} Fe^{3+}_{1.55}\right]. \tag{20}$$

Similarly, the distribution of Mn^{2+}, Mn^{4+}, Fe^{2+}, Fe^{3+}, and Al^{3+} cations at the octahedral and tetrahedral was determined as reported by integrated intensity of deconvoluted strong peaks in $MnFe_{2-x}Al_xO_4$ ($x = 0.3, 0.6$, and 0.9). The substitution formula of Al-doped manganese ferrite could be designated as follows:

$$\begin{aligned}
&\left(Mn^{4}_{0.55}\, Fe^{3+}_{0.47}\, Al^{3+}_{0.08}\right)\left[Mn^{2+}_{0.45}\, Fe^{2+}_{1.47} Al^{3+}_{0.08}\right],\\
&\left(Mn^{4+}_{0.55}\, Fe^{3+}_{0.39}\, Al^{3+}_{0.16}\right)\left[Mn^{2+}_{0.45}\, Fe^{2+}_{1.43} Al^{3+}_{0.12}\right],\\
&\left(Mn^{4+}_{0.55}\, Fe^{3+}_{0.19}\, Al^{3+}_{0.36}\right)\left[Mn^{4+}_{0.45}\, Fe^{2+}_{1.43} Al^{3+}_{0.12}\right].
\end{aligned} \tag{21}$$

With regard to the assessment of cations among octahedral and tetrahedral, Al^{3+} cations choose tetrahedral sites, which deals with chances that Al^{3+} cations would substitute Fe^{3+} cations. The substitution of Fe^{3+} cations by Al^{3+} cations is in good compliance with preparation, XRD calculation analysis, EDX spectrum analysis, and magnetic characteristics.

Magnetic hysteresis loops of $MnFe_{2-x}Al_xO_4$ measured by vibrating sample magnetometer (VSM) at RT are presented in Figure 9. The pristine manganese ferrite sample displays ferromagnetic type nature bearing saturation magnetization of 47.32 emu/g when compared to the Al-doped sample (inset of Figure 9). The representative magnetic characteristics of purified and Al-doped ferrite samples calculated on the basis of the hysteresis loop including H_c, M_r, M_s, η_{exp}, and M_r/M_s-squareness ratio are shown in Table 5. The magnetization evaluation was performed by using an additional field area of the calculated $M(H)$ data by employing Langevin dependence [53]:

$$M(H) = M_s \cdot \left(1 - \frac{k_B T}{M_s \rho V_{eff} \mu_o H}\right), \tag{22}$$

where V_{eff}, ρ, and T are the effective values of the volume, density, and temperature, respectively, and the other values are related to their typical definitions.

The Fe^{2+} and Fe^{3+} cation saturation magnetization and coercivity are changed by embedding Al^{3+} cations into manganese ferrite. As a result of integrated intensity of deconvoluted peaks, visible saturation magnetization and coercivity addiction to Mn^{2+} and Mn^{4+} ions were negligibly afflicted by the doping of Al^{3+} cations into manganese ferrite. The moderate saturation magnetization contraction and coercivity escalation as the Al content is elevated is shown in Figure 10. The decreased value of M_s and M_r of the doped ferrite sample may be associated to reduced particle size. The reduction in

M_s after addition of nonmagnetic Al^{3+} in ferrite is also confirmed by the literature date reported by Dessai et al. [46]. Furthermore, there is a decrease in the average crystallite size control existence of spin inclination and spin canting, which appear by virtue of a defined size and surface-related effects. The reduction in M_s and M_r of doped samples as the Al content is elevated may be due to cation diffusion among the host and embedded groups. The substitution of Fe^{2+} and Fe^{3+} ions by Al^{3+} ions at the octahedral and tetrahedral decreases the bond stability of Fe^{3+}-O-Fe^{3+}. The decrease in the amount of Fe^{2+} and Fe^{3+} cations in the A- and B-sites decreases the magnetic dipole moment of the B-sublattice and consequently decreases the magnetic moment of ferrites. The exchange of Fe^{3+} cations bearing magnetic moment 5 μ_B with nonmagnetic Al^{3+} cations carrying magnetic moment 0 μ_B decreases the superexchange bonding that balances adjacent magnetic dipoles in an antiparallel form. Moreover, the decrease in overall magnetization is possible because of reinforced spin noncollinearity. The elevation of Al^{3+} ions which decreases the lattice parameter is due to smaller ionic radius (0.55 Å) of Al^{3+} cations as compared to Fe^{3+} cations (0.67 Å). The decrease in magnetization in embedded ferrite is also associated with exchange of cations in the A- and B-sites. The fact is that M_s builds upon the number and type of cation based at different sites in tetrahedral and octahedral bonding sites in the ferrite. The exchange influences the magnetization M_A and M_B of the A and B ferrite sublattices. The affiliation of $M_B - M_A$ produces magnetization in spinel ferrites. In manganese-based ferrite, Mn^{4+} ions choose tetrahedral sites and are emphasized as the Al concentration is elevated. The Mn^{2+} ion location in the octahedral sites fades away as the Al content increases. Generally, tetrahedral and octahedral sites in ferrites engaged by Fe^{3+} cations are partially substituted by Al^{3+} cations. The substitution of Fe^{3+} by Al^{3+} cations in the B-sites decides magnetization of manganese ferrites. The reduction of magnetization of the Al-doped ferrite samples is due to substitution of Al^{3+} ions. The squareness ratio (R) less than 0.5 indicates a multidomain structure of ferrite materials while greater than 0.5 signifies a single-domain structure of manganese ferrite. According to the recent investigation carried out related to squareness ratio (R) revealed in several places in the literature, the squareness ratio (R) observed between 0.01 and 0.1 suggests a multidomain structure of ferrite materials [54–56].

4. Conclusions

The significance of Al^{3+} cations as a dopant in nanocrystalline manganese ferrite prepared through the thermal treatment method was discussed. The nanostructured samples were characterized by different methods to examine nanocrystallinity, thermal stability, chemical stability, distribution, and morphological properties. The representative Scherrer formula and Williamson-Hall extrapolation equations were employed to determine the crystallite size and lattice strain parameters. The parameters including ionic radii of tetrahedral and octahedral bonding sites, oxygen positional constants, hopping and bond lengths, bond angles and sites, and edge lengths were determined from the XRD spectrum. The characterization such as XPS and M-H analysis explains the inconsistency in the theoretically anticipated bond angles which implied beefing up of the A-B superexchange synergy. Distribution, chemical form, and degree of inversion were determined from the XPS spectrum. The characteristic magnetic hysteresis loop attained from VSM at RT displays that both M_r and M_s are reduced as the Al content is elevated. This contraction was associated with spin noncollinearity and delicate interactions between sublattices.

Data Availability

The data used to support the findings of this study are included within the article.

Conflicts of Interest

The authors declare that they have no conflicts of interest.

Acknowledgments

This project was funded by the Deanship of Scientific Research (DSR) at King Abdulaziz University, Jeddah, under grant no. (G: 191-135-1442). The authors, therefore, acknowledge with thanks the DSR for the technical and financial support.

References

[1] R. Valenzuela, "Novel applications of ferrites," *Physics Research International*, vol. 2012, Article ID 591839, 9 pages, 2012.

[2] M. Latorre-Esteves, A. Cortés, M. Torres-Lugo, and C. Rinaldi, "Synthesis and characterization of carboxymethyl dextran-coated Mn/Zn ferrite for biomedical applications," *Journal of Magnetism and Magnetic Materials*, vol. 321, no. 19, pp. 3061–3066, 2009.

[3] A. Nigam and S. J. Pawar, "Structural, magnetic, and antimicrobial properties of zinc doped magnesium ferrite for drug delivery applications," *Ceramics International*, vol. 46, no. 4, pp. 4058–4064, 2020.

[4] K. K. Kefeni, T. A. M. Msagati, T. T. I. Nkambule, and B. B. Mamba, "Spinel ferrite nanoparticles and nanocomposites for biomedical applications and their toxicity," *Materials Science and Engineering: C*, vol. 107, article 110314, 2020.

[5] X. Wang, L. Gong, D. Zhang, X. Fan, Y. Jin, and L. Guo, "Room temperature ammonia gas sensor based on polyaniline/copper ferrite binary nanocomposites," *Sensors and Actuators B: Chemical*, vol. 322, article 128615, 2020.

[6] G. Sukmarani, R. Kusumaningrum, A. Noviyanto et al., "Synthesis of manganese ferrite from manganese ore prepared by mechanical milling and its application as an inorganic heat-resistant pigment," *Journal of Materials Research and Technology*, vol. 9, no. 4, pp. 8497–8506, 2020.

[7] G. Ott, J. Wrba, and R. Lucke, "Recent developments of Mn-Zn ferrites for high permeability applications," *Journal of Magnetism and Magnetic Materials*, vol. 254-255, pp. 535–537, 2003.

[8] V. Kumar Chakradhary and M. J. Akhtar, "Absorption properties of CNF mixed cobalt nickel ferrite nanocomposite for

radar and stealth applications," *Journal of Magnetism and Magnetic Materials*, vol. 525, article 167592, 2021.

[9] M. Hernandez, M. Messagie, O. Hegazy, L. Marengo, O. Winter, and J. van Mierlo, "Environmental impact of traction electric motors for electric vehicles applications," *JLCA*, vol. 22, no. 1, pp. 54–65, 2017.

[10] C. C. Agrafiotis and V. T. Zaspalis, "Self-propagating high-temperature synthesis of MnZn-ferrites for inductor applications," *Journal of Magnetism and Magnetic Materials*, vol. 283, no. 2-3, pp. 364–374, 2004.

[11] O. Caltun, I. Dumitru, M. Feder, N. Lupu, and H. Chiriac, "Substituted cobalt ferrites for sensors applications," *Journal of Magnetism and Magnetic Materials*, vol. 320, no. 20, pp. e869–e873, 2008.

[12] R. Ranga, A. Kumar, P. Kumari, P. Singh, V. Madaan, and K. Kumar, "Ferrite application as an electrochemical sensor: a review," *Materials Characterization*, vol. 178, article 111269, 2021.

[13] F. Javed, M. A. Abbas, M. I. Asad et al., "Gd^{3+} doped $CoFe_2O_4$ nanoparticles for targeted drug delivery and magnetic resonance imaging," *Magnetochemistry*, vol. 7, no. 4, p. 47, 2021.

[14] N. Adeela, K. Maaz, U. Khan et al., "Influence of manganese substitution on structural and magnetic properties of $CoFe_2O_4$ nanoparticles," *Journal of Alloys and Compounds*, vol. 639, pp. 533–540, 2015.

[15] F. Nekvapil, A. Bunge, T. Radu, S. Cinta Pinzaru, and R. Turcu, "Raman spectra tell us so much more: Raman features and saturation magnetization for efficient analysis of manganese zinc ferrite nanoparticles," *Journal of Raman Spectroscopy*, vol. 51, no. 6, pp. 959–968, 2020.

[16] M. E. Fleet, "The structure of magnetite: symmetry of cubic spinels," *Journal of Solid State Chemistry*, vol. 62, no. 1, pp. 75–82, 1986.

[17] S. K. Pradhan, S. Bid, M. Gateshki, and V. Petkov, "Microstructure characterization and cation distribution of nanocrystalline magnesium ferrite prepared by ball milling," *Materials Chemistry and Physics*, vol. 93, no. 1, pp. 224–230, 2005.

[18] P. Puspitasari, U. A. Rizkia, S. Sukarni, A. A. Permanasari, A. Taufiq, and A. B. N. R. Putra, "Effects of various sintering conditions on the structural and magnetic properties of zinc ferrite (ZnFe2O4)," *Materials Research*, vol. 24, no. 1, pp. 1–5, 2020.

[19] B. J. Rani, M. Ravina, B. Saravanakumar et al., "Ferrimagnetism in cobalt ferrite ($CoFe_2O_4$) nanoparticles," *Nano-Structures and Nano-Objects*, vol. 14, pp. 84–91, 2018.

[20] Y. W. Ju, J. H. Park, H. R. Jung, S. J. Cho, and W. J. Lee, "Electrospun $MnFe_2O_4$ nanofibers: preparation and morphology," *Composites Science and Technology*, vol. 68, no. 7-8, pp. 1704–1709, 2008.

[21] Y. Slimani, M. A. Almessiere, M. Sertkol et al., "Structural, magnetic, optical properties and cation distribution of nanosized $Ni_{0.3}Cu_{0.3}Zn_{0.4}Tm_xFe_{2-x}O_4$ ($0.0 \le x \le 0.10$) spinel ferrites synthesized by ultrasound irradiation," *Ultrasonics Sonochemistry*, vol. 57, pp. 203–211, 2019.

[22] A. Hossain, M. S. I. Sarker, M. K. R. Khan, and M. M. Rahman, "Spin effect on electronic, magnetic and optical properties of spinel $CoFe_2O_4$: a DFT study," *Materials Science and Engineering: B*, vol. 253, article 114496, 2020.

[23] T. Ramaprasad, R. Jeevan Kumar, U. Naresh, M. Prakash, D. Kothandan, and K. Chandra Babu Naidu, "Effect of pH value on structural and magnetic properties of CuFe2O4nanoparticles synthesized by low temperature hydrothermal technique," *Materials Research Express*, vol. 5, no. 9, article 095025, 2018.

[24] E. E. Ateia, A. A. el-Bassuony, G. Abdelatif, and F. S. Soliman, "Novelty characterization and enhancement of magnetic properties of Co and Cu nanoferrites," *Journal of Materials Science: Materials in Electronics*, vol. 28, no. 1, pp. 241–249, 2017.

[25] Z. Zhang, G. Yao, X. Zhang, J. Ma, and H. Lin, "Synthesis and characterization of nickel ferrite nanoparticles via planetary ball milling assisted solid-state reaction," *Ceramics International*, vol. 41, no. 3, pp. 4523–4530, 2015.

[26] J. Wang, F. Ren, R. Yi, A. Yan, G. Qiu, and X. Liu, "Solvothermal synthesis and magnetic properties of size-controlled nickel ferrite nanoparticles," *Journal of Alloys and Compounds*, vol. 479, no. 1-2, pp. 791–796, 2009.

[27] I. H. Gul, W. Ahmed, and A. Maqsood, "Electrical and magnetic characterization of nanocrystalline Ni-Zn ferrite synthesis by co-precipitation route," *Journal of Magnetism and Magnetic Materials*, vol. 320, no. 3-4, pp. 270–275, 2008.

[28] D. H. Chen and X. R. He, "Synthesis of nickel ferrite nanoparticles by sol-gel method," *Materials Research Bulletin*, vol. 36, no. 7-8, pp. 1369–1377, 2001.

[29] G. Singh and S. Chandra, "Electrochemical performance of $MnFe_2O_4$ nano-ferrites synthesized using thermal decomposition method," *International Journal of Hydrogen Energy*, vol. 43, no. 8, pp. 4058–4066, 2018.

[30] J. Huo and M. Wei, "Characterization and magnetic properties of nanocrystalline nickel ferrite synthesized by hydrothermal method," *Materials Letters*, vol. 63, no. 13-14, pp. 1183-1184, 2009.

[31] V. Pillai, P. Kumar, M. S. Multani, and D. O. Shah, "Structure and magnetic properties of nanoparticles of barium ferrite synthesized using microemulsion processing," *Colloids and Surfaces: Physicochemical and Engineering Aspects*, vol. 80, no. 1, pp. 69–75, 1993.

[32] E. Mazarío, P. Herrasti, M. P. Morales, and N. Menéndez, "Synthesis and characterization of $CoFe_2O_4$ ferrite nanoparticles obtained by an electrochemical method," *Nanotechnology*, vol. 23, no. 35, article 355708, 2012.

[33] R. Nawathey-Dikshit, S. R. Shinde, S. B. Ogale, S. D. Kulkarni, S. R. Sainkar, and S. K. Date, "Synthesis of single domain strontium ferrite powder by pulsed laser ablation," *Applied Physics Letters*, vol. 68, no. 24, pp. 3491–3493, 1996.

[34] M. G. Naseri, M. K. Halimah, A. Dehzangi, A. Kamalianfar, E. B. Saion, and B. Y. Majlis, "A comprehensive overview on the structure and comparison of magnetic properties of nanocrystalline synthesized by a thermal treatment method," *Journal of Physics and Chemistry of Solids*, vol. 75, no. 3, pp. 315–327, 2014.

[35] M. Naseri, "Optical and magnetic properties of monophasic cadmium ferrite ($CdFe_2O_4$) nanostructure prepared by thermal treatment method," *Journal of Magnetism and Magnetic Materials*, vol. 392, pp. 107–113, 2015.

[36] M. G. Naseri, E. B. Saion, M. Hashim, A. H. Shaari, and H. A. Ahangar, "Synthesis and characterization of zinc ferrite nanoparticles by a thermal treatment method," *Solid State Communications*, vol. 151, no. 14-15, pp. 1031–1035, 2011.

[37] S. Gyergyek, D. Makovec, A. Kodre, I. Arčon, M. Jagodič, and M. Drofenik, "Influence of synthesis method on structural and magnetic properties of cobalt ferrite nanoparticles," *Journal of Nanoparticle Research*, vol. 12, no. 4, pp. 1263–1273, 2010.

[38] S. Jauhar, J. Kaur, A. Goyal, and S. Singhal, "Tuning the properties of cobalt ferrite: a road towards diverse applications," *RSC Advances*, vol. 6, no. 100, pp. 97694–97719, 2016.

[39] K. Chakrapani, G. Bendt, H. Hajiyani et al., "Role of composition and size of cobalt ferrite nanocrystals in the oxygen evolution reaction," *ChemCatChem*, vol. 9, no. 15, pp. 2988–2995, 2017.

[40] S. Prathapani, M. Vinitha, T. V. Jayaraman, and D. Das, "Effect of Er doping on the structural and magnetic properties of cobalt-ferrite," *Journal of Applied Physics*, vol. 115, no. 17, pp. 17A502–A7A5023, 2014.

[41] S. K. Pendyala, K. Thyagarajan, A. GuruSampath Kumar, and L. Obulapathi, "Effect of Mg doping on physical properties of Zn ferrite nanoparticles," *Journal of the Australian Chemical Society*, vol. 54, no. 3, pp. 467–473, 2018.

[42] F. R. Mariosi, J. Venturini, A. da Cas Viegas, and C. P. Bergmann, "Lanthanum-doped spinel cobalt ferrite ($CoFe_2O_4$) nanoparticles for environmental applications," *Ceramics International*, vol. 46, no. 3, pp. 2772–2779, 2020.

[43] J. A. Paulsen, A. P. Ring, C. C. H. Lo, J. E. Snyder, and D. C. Jiles, "Manganese-substituted cobalt ferrite magnetostrictive materials for magnetic stress sensor applications," *Journal of Applied Physics*, vol. 97, no. 4, article 044502, 2005.

[44] H. Kaur, A. Singh, V. Kumar, and D. S. Ahlawat, "Structural, thermal and magnetic investigations of cobalt ferrite doped with Zn^{2+} and Cd^{2+} synthesized by auto combustion method," *Journal of Magnetism and Magnetic Materials*, vol. 474, pp. 505–511, 2019.

[45] F. Z. Mou, J. G. Guan, Z. G. Sun, X. A. Fan, and G. X. Tong, "In situ generated dense shell-engaged Ostwald ripening: A facile controlled- preparation for $BaFe_{12}O_{19}$ hierarchical hollow fiber arrays," *Journal of Solid State Chemistry*, vol. 183, no. 3, pp. 736–743, 2010.

[46] P. P. Gauns Dessai, S. S. Meena, and V. M. S. Verenkar, "Influence of addition of Al^{3+} on the structural and solid state properties of nanosized Ni-Zn ferrites synthesized using malic acid as a novel fuel," *Journal of Alloys and Compounds*, vol. 842, article 155855, 2020.

[47] K. V. Kumar, D. Paramesh, and P. V. Reddy, "Effect of Aluminium doping on structural and magnetic properties of Ni-Zn ferrite nanoparticles," *World Journal of Nano Science and Engineering*, vol. 5, no. 3, pp. 68–77, 2015.

[48] S. P. Waghmare, D. M. Borikar, and K. G. Rewatkar, "Impact of Al doping on structural and magnetic properties of Co-ferrite," *Materials Today*, vol. 4, pp. 11866–11872, 2017.

[49] S. U. Rather and O. M. Lemine, "Effect of Al doping in zinc ferrite nanoparticles and their structural and magnetic properties," *Journal of Alloys and Compounds*, vol. 812, pp. 152058–152068, 2020.

[50] G. Kumar, R. K. Kotnala, J. Shah et al., "Cation distribution: a key to ascertain the magnetic interactions in a cobalt substituted Mg–Mn nanoferrite matrix," *Physical Chemistry Chemical Physics*, vol. 19, no. 25, pp. 16669–16680, 2017.

[51] S. R. Naik and A. V. Salker, "Change in the magnetostructural properties of rare earth doped cobalt ferrites relative to the magnetic anisotropy," *Journal of Materials Chemistry*, vol. 22, no. 6, pp. 2740–2750, 2012.

[52] R. S. Yadav, I. Kuřitka, J. Vilcakova et al., "Impact of grain size and structural changes on magnetic, dielectric, electrical, impedance and modulus spectroscopic characteristics of $CoFe_2O_4$ nanoparticles synthesized by honey mediated sol-gel combustion method," *Advances in Natural Sciences: Nanoscience*, vol. 8, article 045002, 2017.

[53] A. T. Raghavender, S. E. Shirsath, D. Pajic et al., "Effect of Al doping on the cation distribution in copper ferrite nanoparticles and their structural and magnetic properties," *Journal of the Korean Physical Society*, vol. 61, no. 4, pp. 568–574, 2012.

[54] S. T. Assar and H. F. Abosheiasha, "Effect of Ca substitution on some physical properties of nano-structured and bulk Ni-ferrite samples," *Journal of Magnetism and Magnetic Materials*, vol. 374, pp. 264–272, 2015.

[55] H. N. Chaudhari, P. N. Dhruv, C. Singh, S. S. Meena, S. Kavita, and R. B. Jotania, "Effect of heating temperature on structural, magnetic, and dielectric properties of magnesium ferrites prepared in the presence of Solanum lycopersicum fruit extract," *Journal of Materials Science: Materials in Electronics*, vol. 31, pp. 18445–18463, 2020.

[56] A. R. Kagdi, N. P. Solanki, F. E. Carvalho et al., "Influence of Mg substitution on structural, magnetic and dielectric properties of X-type barium![single bond](https://sdfestaticassets-us-east-1.sciencedirectassets.com/shared-assets/55/entities/sbnd.gif)zinc hexaferrites $Ba_2Zn_{2-x}Mg_xFe_{28}O_{46}$," *Journal of Alloys and Compounds*, vol. 741, pp. 377–391, 2018.

Hindawi
Journal of Nanomaterials
Volume 2021, Article ID 9076170, 13 pages
https://doi.org/10.1155/2021/9076170

Research Article

Effect of Coupling Agent on Softwood Kraft Nanocellulose Fibril-Reinforced Polylactic Acid Biocomposite

Usman Saeed, Sami Ullah Rathur, Hamad AlTuraif, and Hisham Bamufleh

Department of Chemical and Materials Engineering, Faculty of Engineering, King Abdulaziz University, Jeddah 21441, Saudi Arabia

Correspondence should be addressed to Usman Saeed; usman144de@yahoo.com

Received 12 August 2021; Revised 2 November 2021; Accepted 29 November 2021; Published 24 December 2021

Academic Editor: P. Davide Cozzoli

The nanocellulose fibril produced by using natural sources can be used in developing sustainable and green products. The useful features of nanocellulose fibril can include valuable physical properties, appropriate surface chemistry, low toxicity, and biocompatibility. The study presented shows the use of polylactic acid with five different percentages of nanocellulose fibril and the use of 3% maleic anhydride as a coupling agent. The maleic anhydride acts as coupling agent which improves the thermochemical and thermomechanical characteristics of the end product. The addition of 3% maleic anhydride as coupling agent with 10% nanocellulose fibril improved the impact strength up to 14.3%, elastic modulus up to 40.6%, and tensile strength up to 30.1%. Furthermore, the dynamic mechanical analysis result indicates that the inclusion of maleic anhydride improved the toughness by reducing the tan δ peak and increases the storage modulus. Finally, the scanning electron micrograph shows that the interfacial compatibility between nanocellulose fibril and polylactic acid matrix is improved with the addition of maleic anhydride.

1. Introduction

The growing environmental concerns of plastic waste and pollution have paved the way for use of naturally sourced sustainable polymers instead of synthetic polymer. In the sustainable product development, natural polymers such as poly(lactic acid) (PLA), (butylene succinate) (PBS), and poly(butylenesadipate-co-terephthalate) (PBSA) are shown to be the most useful alternative to synthetic polymers as they are biocompatible and biodegradable [1–3]. The biopolymer degrades when disposed and returns all natural constituents to the environment helping in decreasing the plastic waste. In the naturally sourced polymers, PLA is a promising candidate for developing green products in comparison to synthetic polymers such as polyethylene, polypropylene, and polyethylene terephthalate. Also, PLA offers suitable physical properties (specific gravity and shrink rate) and thermal processing ability [3]. The disadvantages of using PLA can include innate brittleness, inadequate thermal stability, and lower quality of crystallization which limits its use in mass manufacturing in fields such as biomedical, packaging, energy storage, and automotive [4].

The natural fibers can help in forming green composite due to their cost-effectiveness, biodegradability, renewability, and low density. The naturally sourced fibers such as flex and kenaf are used to develop green composite because of their suitable tensile strength (280 ± 15 MPa) and elastic modulus (40 ± 5 GPa). The natural fibers when compared to synthetic glass, aramid, and carbon fiber have some disadvantages such as lower tensile strength, lower processing temperature, higher linear coefficients of thermal expansion, and moisture susceptibility [5]. In the natural fiber, the plant-derived cellulose can be used as reinforcement at the nanolevels which includes nanocellulose fibril (NCF) and nanocrystalline cellulose (NCC) [6–9]. The nanocellulose fibril (NCF) when used with polymer composite has shown excellent ability to act as nanoreinforcement, and it is cost-effective with respect to manufacturing. Moreover, the advantages of using NCF as nanoreinforcement include low density, strength, high stiffness, and biodegradability [10, 12]. There are studies performed to address the problem of brittleness with PLA by blending it with elastomeric materials such as rubber, copolymerizing with other monomer, and by utilizing plasticizer [13–15].

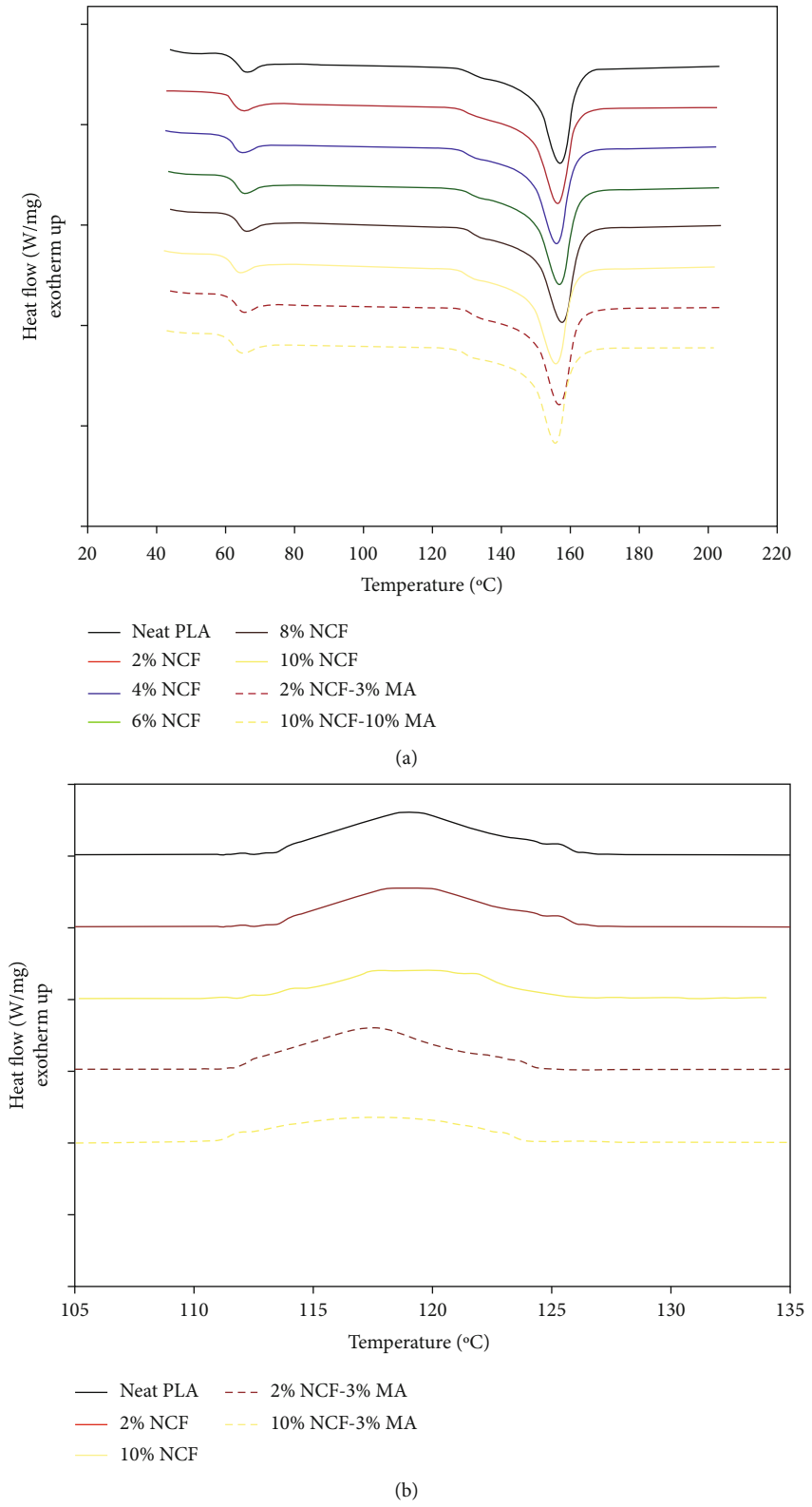

Figure 1: DSC thermogram of PLA-NCF-MA composite: (a) heating and (b) cooling.

However, the examiners described that even though there are substantial improvements in the toughness and ductility, the blends sacrificed their mechanical properties such as Young's modulus and strength. In one of the studies, PLA was reinforced with cellulose nanowhisker (CNW) and nanocellulose fibril (NCF) to improve the mechanical properties [16]. Additionally, there are issues related to uniform dispersion of nanocellulose fibril with

Table 1: Thermal properties of PLA-NCF-MA composites.

PLA-NCF-MA	T_g (°C)	T_m (°C)	T_c (°C)	ΔH_m (J/g)	X_c %
100/0/0	59.4	153.6	126.7	24.9	14.9
98/2/0	59.1	153.4	125.6	22.3	13.3
96/4/0	58.0	152.7	124.9	25.9	12.7
94/6/0	57.7	152.3	124.5	24.9	11.2
92/8/0	57.6	151.9	124.1	22.1	10.4
90/10/0	57.5	151.4	123.7	20.9	9.5
95/2/3	58.0	152.6	124.9	23.2	13.1
93/4/3	57.9	152.4	124.5	24.8	12.4
91/6/3	57.6	151.5	124.1	23.6	10.9
89/8/3	57.3	151.5	123.9	23.5	10.6
87/10/3	57.4	151.1	123.5	20.7	9.3

polar surfaces in the nonpolar polymers such as PLA [17–20]. The inhomogeneous distribution and low compatibility of NCF in polymer matrix resulted in end product with inadequate and unsuitable properties [21, 22]. The previous studies have shown that fiber-matrix interface is an important factor which predicts the characteristics of composite. To improve the interfacial adhesion between polymer and NCF, a study utilized a coupling agent and performed surface modification of nanocellulose fibrils (NCF) [23]. The studies also illustrated the use of functional elements found in PLA interact with nanocellulose by including maleic anhydride (MAH) as compatibilizer [24–26]. Carlson et al. showed the improvement in interfacial adhesion by mixing maleic anhydride in starch-reinforced PLA [27]. Also, Petersson and Oksman reported that the addition of microcrystalline cellulose reduces the barrier properties and mechanical strength of PLA biocomposite due to the less interaction between PLA matrix and cellulose [28]. Plackett indicated that by adding maleic anhydride interfacial adhesion can be improved between PLA and cellulose-based wood fiber [29]. To make biocomposite perform usefully, certain amount of adhesion was achieved between surface of the hydrophilic nanocellulose fibers and polymer matrix. The treatments such as grafting, isocyanate, dewaxing, and coupling agent were used to enhance the interfacial adhesion between natural fiber and polymer matrix [30]. The treatment of jute cellulose fiber with epoxy and silane showed improvement in mechanical properties such as elastic modulus, tensile strength, and hardness [31]. The coir fibers treated with enzyme influenced overall mechanical properties excluding flexural characteristic because of size of fibers [32]. The fibers were chemically treated by using benzoylation, acetylation, and acrylonitrile grafting. The structural stability and improved mechanical properties are the indicators showing the effects of chemical treatment of natural fiber in enhancement of interfacial adhesion [33]. The chemical treatment alternate hydrophilic nature of fiber helps in reducing the effect of moisture in the performance of composite [34]. The chemical treatments have the capability to alternate the physical and chemical properties of composites; therefore, it is necessary to examine the influence of maleated anhydride (MA) as coupling agent in nanocellulose fibril-reinforced PLA composite for improvement in interfacial adhesion.

In the research presented, the influence of 3% maleic anhydride (MA) as a coupling agent on variable NCF content (2 wt.%–10 wt.%)-reinforced polylactic acid (PLA) is being studied by evaluating chemistry, morphological, mechanical, and thermal properties. The characterization was performed by tensile test, differential scanning calorimetry (DSC), dynamic mechanical analysis (DMA), drop shape analyzer (DSA), and X-ray photo electron spectroscopy (XPS). Finally, fracture surface of the PLA-NCF-MA composites was analyzed by using scanning electron microscopy (SEM).

2. Materials and Methods

2.1. Preparation. NatureWorks, USA, provided the polylactic acid (PLA) 2003 D with melt flow index of 6 g/10 min. The University of Maine (Orono, USA) supplied water-based softwood kraft nanocellulose fibrils (NCF) having an average diameter of 30 nm-50 nm and approximate length of one micron. A stable dispersion with considerable transparency was being attained by dilution of NCF with Milli-Q water. The Milli-Q water helped in development of solution with NCF as 1.67 g/L. To produce the suspension, the solution was being stirred with the help of ultrasonic microtip for a time period of 10 min having amplitude of 25%. The Optima L-90K18 ultracentrifuge (Beckman Coulter, USA) was used to remove fibril aggregates by centrifuging at 10,000 rpm for 20 min. Finally, NCF was dried in spray dryer (BUCHI B290, Switzerland) before using it as reinforcement.

3% maleic anhydride (MA, Fusabond, MB100, DuPont, USA) was used as a coupling agent in PLA-NCF composite to improve adhesion between NCF and PLA. The NCF in five different concentrations ranging from 2% to 10% was mixed for 20 minutes with PLA and 3% maleic anhydride (MA) by using twin-screw extruder (Leistritz model ZSE27) with speed of 100 rpm at 180°C. The developed specimen was cooled in water, and a grinder was used for pelletizing. The drying of pellets was done for 24 h at 60°C. The hot compression moulding machine (Carver Press, Germany) was used to produce specimen for tensile test according to ASTM D638 type IV dimensions and 40 mm × 12mm × 5 mm dimensions for dynamic mechanical analysis. The hot compression moulding of pellets was performed for 2 minutes at 120°C with pressure of one ton. The developed PLA-NFC-MA composite specimens were cooled down to 25°C temperature under pressure for 24 h.

2.2. Characterization. The thermal behaviour of PLA-NCF-MA composite was examined by using the differential scanning calorimeter (DSC Netzsch 200 F3). The DSC thermogram was generated at 10°C min^{-1} from 20°C to 200°C for cooling and heating curves. The thermogram was used to examine the melting enthalpy, melting temperature, crystallization temperature, and degree of crystallinity (X_c %).

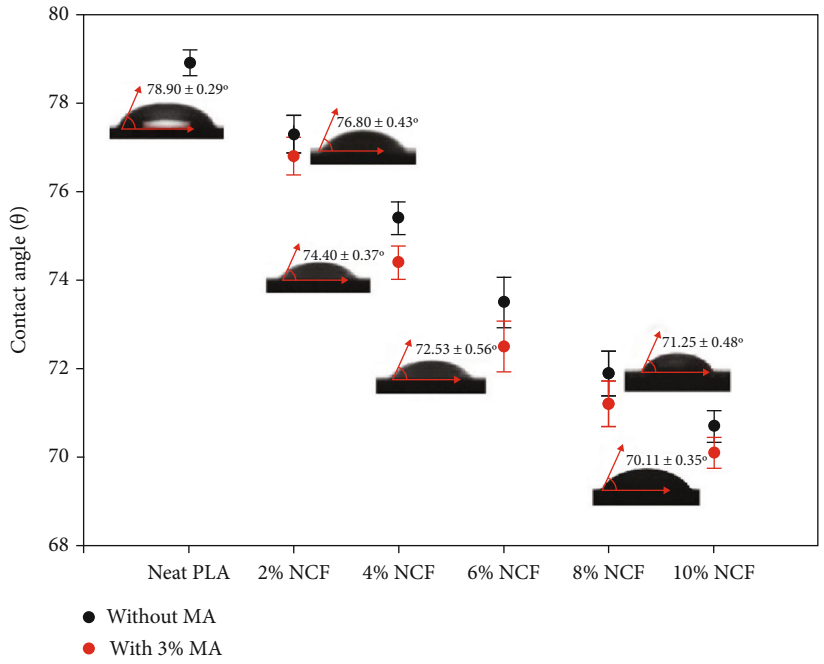

FIGURE 2: Contact angle of the PLA-NCF-MA composite (images of the drops present the values of NCF-PLA with 3% MA).

Equation (1) was used to evaluate the crystallinity (X_c %) of PLA-NCF-MA composite

$$X_c\% = \frac{\Delta H_m}{w \times \Delta H_m^o}, \quad (1)$$

where ΔH_m^o is melting enthalpy of 100% crystalline PLA (93.7 J/g), ΔH_m is the melting enthalpy, and w is the PLA weight fraction in PLA-NCF-MA composite.

The contact angle θ was characterized using a sessile drop of water on the surface of PLA-NCF-MA composite by employing drop shape analyzer (DSA 100, KRUSS, Germany). The water drop image on the surface of composites was taken to determine the contact angle in order to analyze the wetting. Three measurements of each composite specimen were evaluated to find the value of final contact angle.

The tensile testing machine (3369 Instron, USA) with 50 kN load cell was used to characterize the mechanical properties of PLA-NCF-MA composite having ASTM D638 type IV geometry. The test was performed with crosshead speed of 5 mm/min at 25°C having 0.500 N preload.

The impact testing machine (JB W300J, Poland) was utilized to perform Charpy impact test. The ASTMD256 dimensions of the specimen were 10 mm × 10 mm × 55 mm having 2 mm notch size. During the impact test, the impact speed was 5.2 m/s, potential impact energy was 150 J, and raise angle was 150°.

The dynamic mechanical analysis (DMA, 242, Netzsch, USA) was used to characterize PLA-NCF-MA composites for loss factor (tan δ) and storage modulus G'. The DMA functions with dual cantilever approach having sample dimensions of 40 mm × 12 mm × 5 mm. The DMA test was performed having 2°C/min heating rate, 1 Hz frequency, and 0.1% strain rate. During the test, the temperature was maintained between 30°C and 120°C.

The X-ray photo electron spectrometer (XPS, SPECS GmbH, Germany) was used at the pressure 1×10^{-8} mbar to characterize the PLA-NCF-MA composite. The composite specimen surfaces were irradiated by an X-ray source of 150 W and 13.5 kV utilizing dual anode nonmonochromatic Mg-K_α. The PLA-NCF-MA composite specimen was positioned having 90° take-off angle facing the direction of photoelectrons and surface of specimen. The atomic % concentration, energy of binding (BE), and bond type (C1s and O1s) orbital data were obtained by using a hemispherical energy analyzer (PHOIBOS 150 MCD-9) which was functioning in fixed analyzer transmission (FAT) mode.

The fracture surface of PLA-NCF-MA platinum-coated specimen was analyzed by using an electron microscope (JEOL JSM-7600F, MA) having 10 kV accelerating voltage.

All PLA-NCF-MA composite specimens with different compositions were three times examined by employing characterization methods to verify the final outcomes.

3. Results and Discussion

The heating and cooling curves are presented in Figures 1(a) and 1(b) for PLA-NCF-MA composites. The presented figures indicate the melting behaviour and crystallization of the composite. Also, Table 1 presents the assessed values of crystallinity (X_c %), glass transition temperature (T_g), crystallization temperature (T_c), melting enthalpy (ΔH_m), and melting temperature (T_m) of neat PLA and PLA-NCF-MA. The heating thermogram shows that the neat PLA has melting temperature T_m of 153.6°C. Table 1 demonstrates that T_m decreases up to 151.4°C with the rising increments of

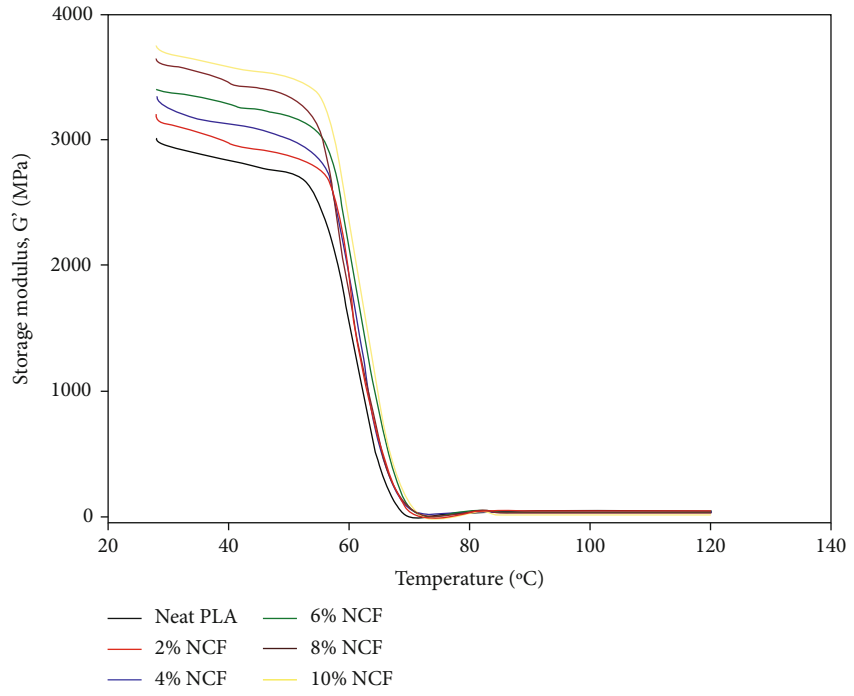

(a)

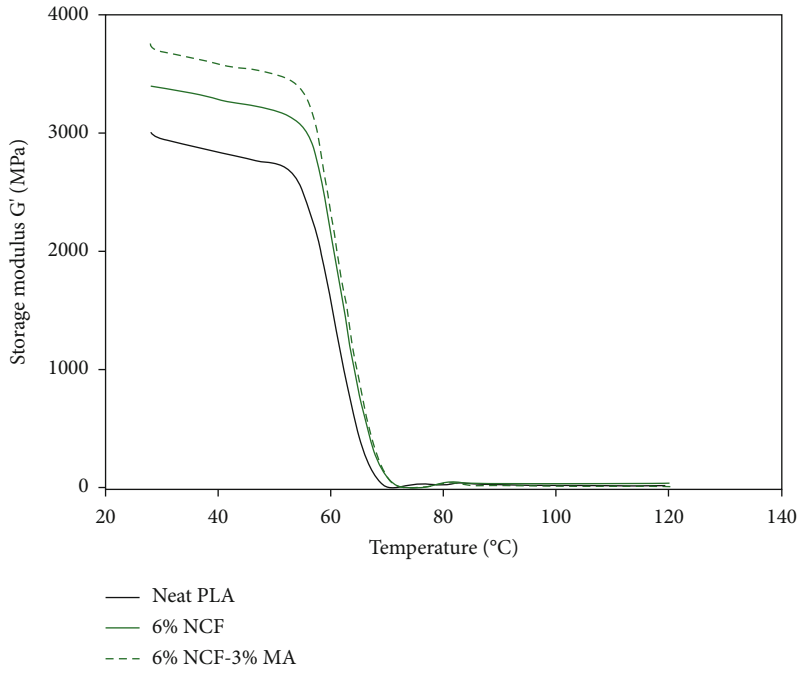

(b)

Figure 3: Continued.

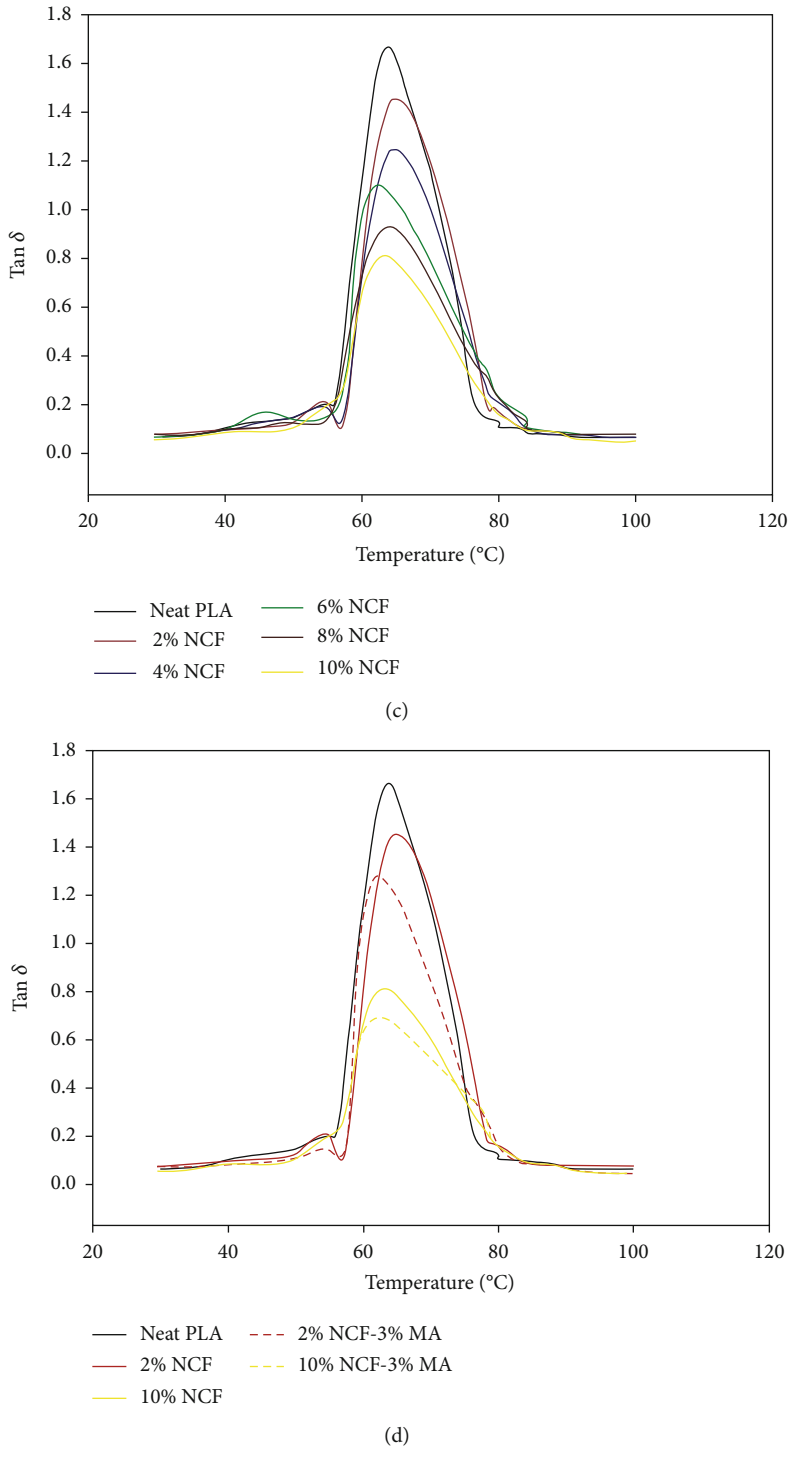

Figure 3: (a) Storage modulus G' of the PLA-NCF composite. (b) Storage modulus G' of PLA-6%NCF-3%MA. (c) tan δ of PLA-NCF. (d) tan δ of PLA-NCF-3%MA.

10% NCF in PLA. Meanwhile, the 3% addition of MA reduces the melting temperature up to 151.1°C of 10%NCF-PLA. Also, the glass transition temperature, T_g, reduces to 57.4°C from 59.4°C with the inclusion of MA and NCF in the PLA. The small reduction of melting and glass transition temperature may have taken place due to the reason that the NCF and MA do not form heterogeneous nucleation sites in the NCF-PLA composite. Also, Figure 1(b) and Table 1 illustrate that the crystallization temperature T_c of neat PLA changes to 123.5°C from 125.5°C when NCF and MA are added in the PLA matrix. The reduction in T_c demonstrates that NCF and MA restrict the mobility of PLA matrix chains for crystallization. The estimated PLA melting enthalpy ΔH_m is 24.9 J/g that reduces

Table 2: Mechanical properties of PLA-NCF-MA composites.

PLA/NCF/MA	Tensile strength (MPa)	Elastic modulus (GPa)	Elongation at break (%)	Impact strength (kJ/m^2)	Storage modulus (MPa)	tan δ
100/0/0	37.1 ± 0.90	0.87 ± 0.02	14.1 ± 0.28	5.32 ± 0.04	3025 ± 20	1.54 ± 0.01
98/2/0	38.9 ± 0.70	0.95 ± 0.03	13.9 ± 0.27	5.13 ± 0.06	3232 ± 19	1.45 ± 0.02
96/4/0	42.7 ± 0.68	1.01 ± 0.05	13.7 ± 0.31	4.86 ± 0.11	3350 ± 18	1.21 ± 0.01
94/6/0	43.6 ± 0.71	1.09 ± 0.03	13.4 ± 0.23	4.55 ± 0.10	3454 ± 15	1.11 ± 0.03
92/8/0	45.1 ± 0.59	1.17 ± 0.02	12.9 ± 0.18	4.29 ± 0.09	3642 ± 17	0.93 ± 0.01
90/10/0	47.6 ± 0.74	1.26 ± 0.01	12.5 ± 0.17	4.01 ± 0.08	3855 ± 16	0.81 ± 0.04
95/2/3	40.8 ± 0.61	1.08 ± 0.03	20.11 ± 0.31	5.64 ± 0.08	3410 ± 19	1.39 ± 0.02
93/4/3	47.9 ± 0.65	1.18 ± 0.02	19.7 ± 0.11	5.85 ± 0.07	3541 ± 15	1.14 ± 0.01
91/6/3	50.8 ± 0.64	1.29 ± 0.01	19.05 ± 0.22	5.90 ± 0.05	3734 ± 17	1.01 ± 0.03
89/8/3	52.1 ± 0.76	1.38 ± 0.06	18.4 ± 0.30	5.98 ± 0.08	3856 ± 18	0.71 ± 0.02
87/10/3	53.2 ± 0.69	1.45 ± 0.04	17.9 ± 0.11	6.21 ± 0.04	4060 ± 19	0.67 ± 0.01

to 20.7 J/g with the inclusion of 3% MA and 10% NCF. The peak width and height of cooling curves (Figure 1(b)) reduce with the introduction of 3% MA and NCF increments which decreases the melting enthalpy for PLA-NCF-FB composite.

Equation (1) was used to calculate the degree of crystallinity (X_c %) in PLA. Table 1 shows that the degree of crystallinity decreases from 14.9% to 9.8% when 10% NCF and 3% MA are added. The 37.4% decrease in X_c % demonstrates that the addition of NCF and MA did not initiate the nucleation site in PLA matrix. The FB and NCF obstruct the movement of PLA chains that result in the reduction of crystallization temperature (T_c). Furthermore, reduction in crystallinity accelerates the diffusivity and solubility of CO_2 in the polymer matrix [5]. The impermeability of crystalline zones hinders the diffusion of molecules due to close packed and regular chain structure that offers minimum free volume for solubility of CO_2. The reduction of crystallinity in PLA-NCF-MA composite indicates that the addition of NCF and MA increases the diffusivity and solubility of CO_2. The energy consumption during processing can be reduced by increased CO_2 solubility which also increases the diffusion coefficient acting as a potential plasticizer in the processes.

The contact angle of sessile drop of water is illustrated in Figure 2 for neat PLA and PLA-NCF-MA composite. The neat PLA has a contact angle of 78.9 ± 0.3°. The 10% NCF addition decreases the contact angle by 11 percent and reaches up to 70.7 ± .0.35° indicating the improvement in hydrophilic behaviour. Also, 3% MA inclusion in 10%NCF-PLA decreases the contact angle to 70.1 ± 0.35° demonstrating the minimum effect of MA on the composite wettability. The enhanced hydrophilic behaviour with inclusion of NCF shows the existence of hyroxyl groups increasing the wettability and hydrophilic behaviour in PLA-NCF. Also, the decrease in water contact angle with the inclusion of NCF increases the surface area providing the opportunity for distilled water to interact more with the surface of fiber. Additionally, the NCF decreases the surface roughness allowing adequate distribution of water leading to reduction of contact angle and enhancement in wetting of PLA-NCF-MA composite.

Figure 3 illustrates the loss factor (tan δ) and storage modulus (G') of composite with respect to temperature. Figure 3(a) illustrates that the storage modulus G' of PLA is 3010 MPa. In contrast to neat PLA, the storage modulus G' is increased up to 20% when 10% NCF is inserted in the PLA matrix. The storage modulus rises due to increased stiffness of the PLA matrix which is reinforced by NCF [35, 36]. Moreover, Figure 3(a) illustrates that the fall of NCF-PLA storage modulus occurs in the range of 56°C and 58°C due to glass transition temperature which is consistent with the results of DSC. The molecular mobility of the PLA matrix chain beyond the glass transition temperature can be the reason because storage modulus G' falls [36]. Figure 3(b), as an example, illustrates that the storage modulus of 6% NCF-PLA is 3454 ± 15 MPa which rises up to 3734 ± 17 MPa when 3% MA is added. The 10% increase in storage modulus with the addition of 3% MA in 6% NCF-PLA composite is due to enhancement in interfacial adhesion between the PLA matrix and NCF. Also, the interfacial adhesion might reduce the molecular mobility at the interfaces of NCF and PLA matrix. Table 2 demonstrates maximum storage modulus values showing enhancement in adhesion which might have occurred because of improvement in compatibility because of MA inclusion. The maleic anhydride (MA) compounds might have reacted to the hydroxyl groups in the NCF that consequently formed the ester bonds, and because of similar polarity, the PLA matrix intermingled with MA which acts as copolymer. The increase of storage modulus occurred due to improvement in interfacial adhesion after the addition of MA as interfacial modifier which linked the PLA matrix and NCF.

Figure 3(c) indicates that 1.55 is the mechanical damping tan δ for neat PLA. The increase of NCF in gradual increments of 10% reduces tan δ up to 0.81. The decrease in tan δ occurs because of restriction of PLA molecule movement instigated by stiff CNF [37]. Figure 3(d) illustrates the reduction in peak height of tan δ to 0.69 when 3% MA is

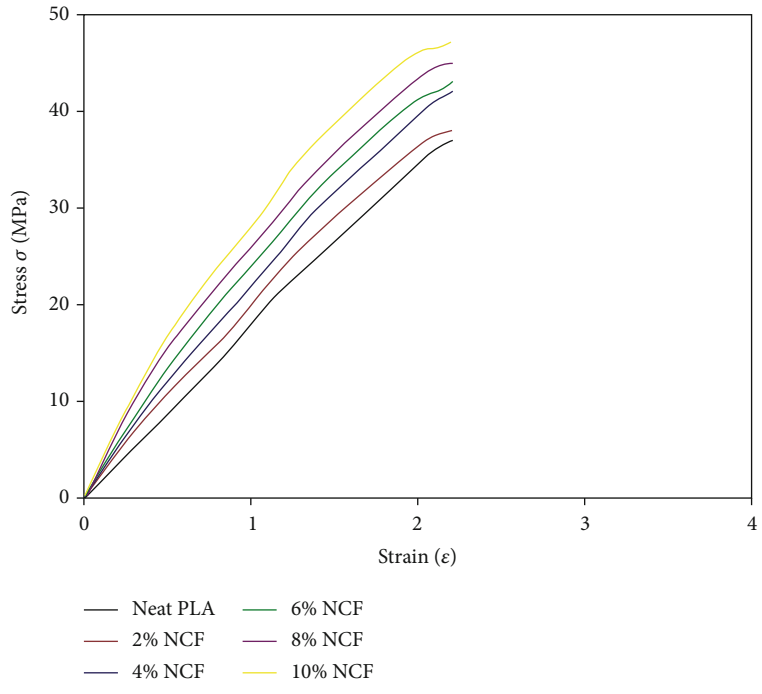

(a)

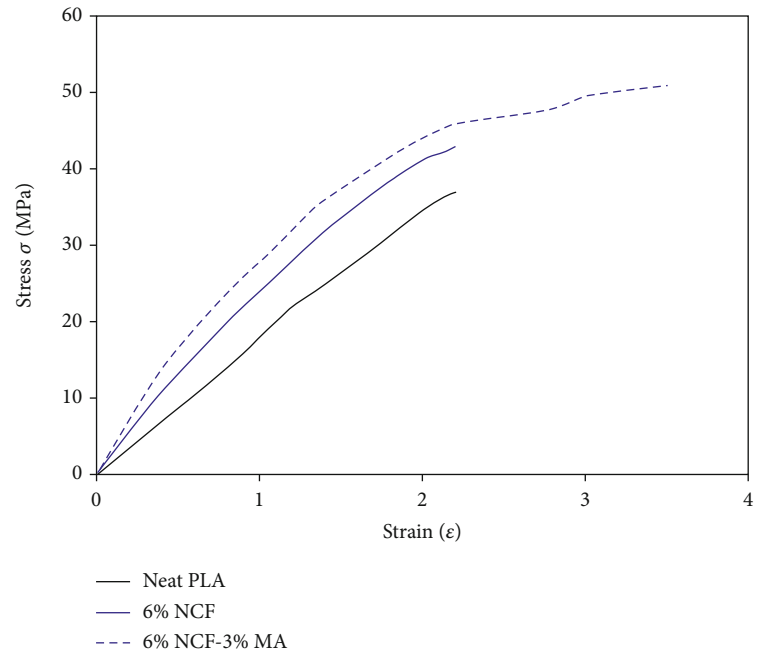

(b)

Figure 4: Continued.

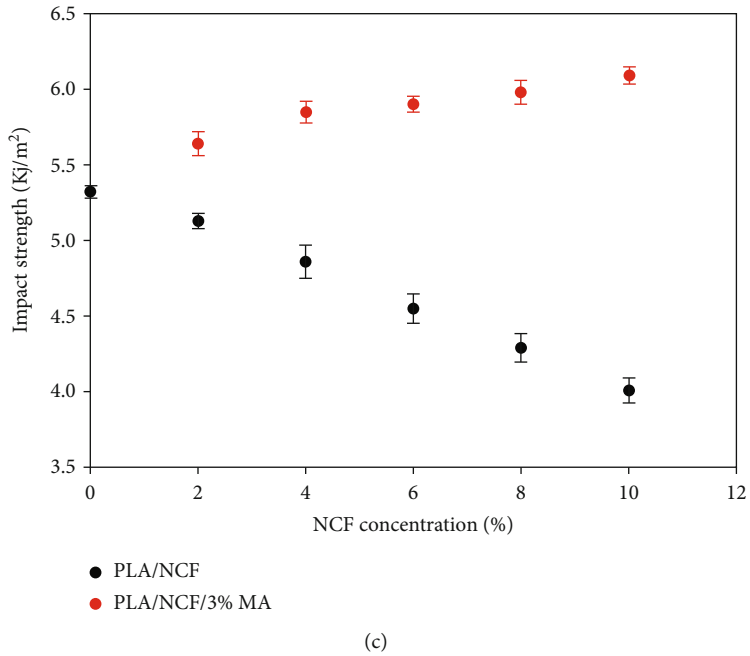

(c)

Figure 4: (a) Tensile curve of PLA-NCF. (b) Tensile curve of PLA-6%NCF-3%MA. (c) Impact strength of PLA-NCF-MA.

Table 3: Atomic % concentration, binding energy (BE), and bond type of C1s and O1s orbitals.

Bond type	Neat PLA		PLA-6% NCF		PLA-6%NCF-3%MA	
	BE (eV)	Atomic % concentration	BE (eV)	Atomic % concentration	BE (eV)	Atomic % concentration
O1s	532.33	22.74	532.31	26.93	532.29	34.59
C1s	284.83	77.01	284.79	72.89	284.95	65.25
O1s_1_O=C	532.09	12.61	532.07	13.82	532.05	14.81
O1s_2_O-C	533.42	10.15	533.33	13.19	533.38	19.70
C1s_1_C-C	284.79	54.65	248.68	47.95	248.85	33.39
C1s_2_C-O	286.38	13.36	286.32	15.35	286.34	18.26
C1s_3_O-C=O	288.90	8.98	288.82	9.67	288.85	13.69

added in 10%NCF-PLA signifying the advancement in interfacial adhesion. The results indicate that the reduction in tan δ increases molecular relaxation and aids the NCF-PLA composite to withstand greater amount of force. Finally, the impact of effective interfacial adhesion can be noticed in reduction of energy dissipation resulting in improved behaviour of energy absorption. Table 2 summarizes the tan δ values of PLA-NCF-MA composites.

Figures 4(a) and 4(b) demonstrate the tensile curves of PLA-NCF-MA composite. Table 2 shows the analogous data of % elongation at break, tensile strength, and elastic modulus. The tensile strength of neat PLA appears to be 37.1 ± 0.9 MPa, and it increases to 47.6 ± 0.74 MPa when the 10% NCF is added to the PLA matrix. Additionally, the insertion of 10% NCF in the PLA matrix increases the modulus of elasticity to 1.26 ± 0.01 MPa in comparison to neat PLA. The 10%NCF-PLA composite shows the improvement in elastic modulus up to 30.9% and tensile strength up to 22.1% when compared to neat PLA. The NCF content from 2% to 10% has negligible effect on the improvement of % elongation at break. The slight reduction in % elongation might have occurred due to the restriction of molecular mobility of PLA chains with the addition NCF. The noticeable increase in % elongation at break, tensile strength, and elastic modulus occurs with the addition of MA in the NCF-PLA composite. Figure 4(b) shows the addition of 3% MA in composite with 6% NCF-PLA increases tensile strength up to 26.9%, elastic modulus up to 32.5%, and % elongation at break up to 21.2% in comparison to neat PLA. The MA acted as interfacial compatibilizer which improved the interfacial adhesion and increased the mechanical properties of the NCF-PLA composite. In contrast to neat PLA, the 3% MA inclusion in 10%NCF-PLA demonstrates the increase of tensile strength up to 30.2%, % elongation at break up to 21.2%, and elastic modulus up to 40.0%. The improvement in mechanical properties might have happened due to the development of hydrogen bonds between the PLA matrix and NCF because of the presence of MA. The presence of strong hydrogen bonds also

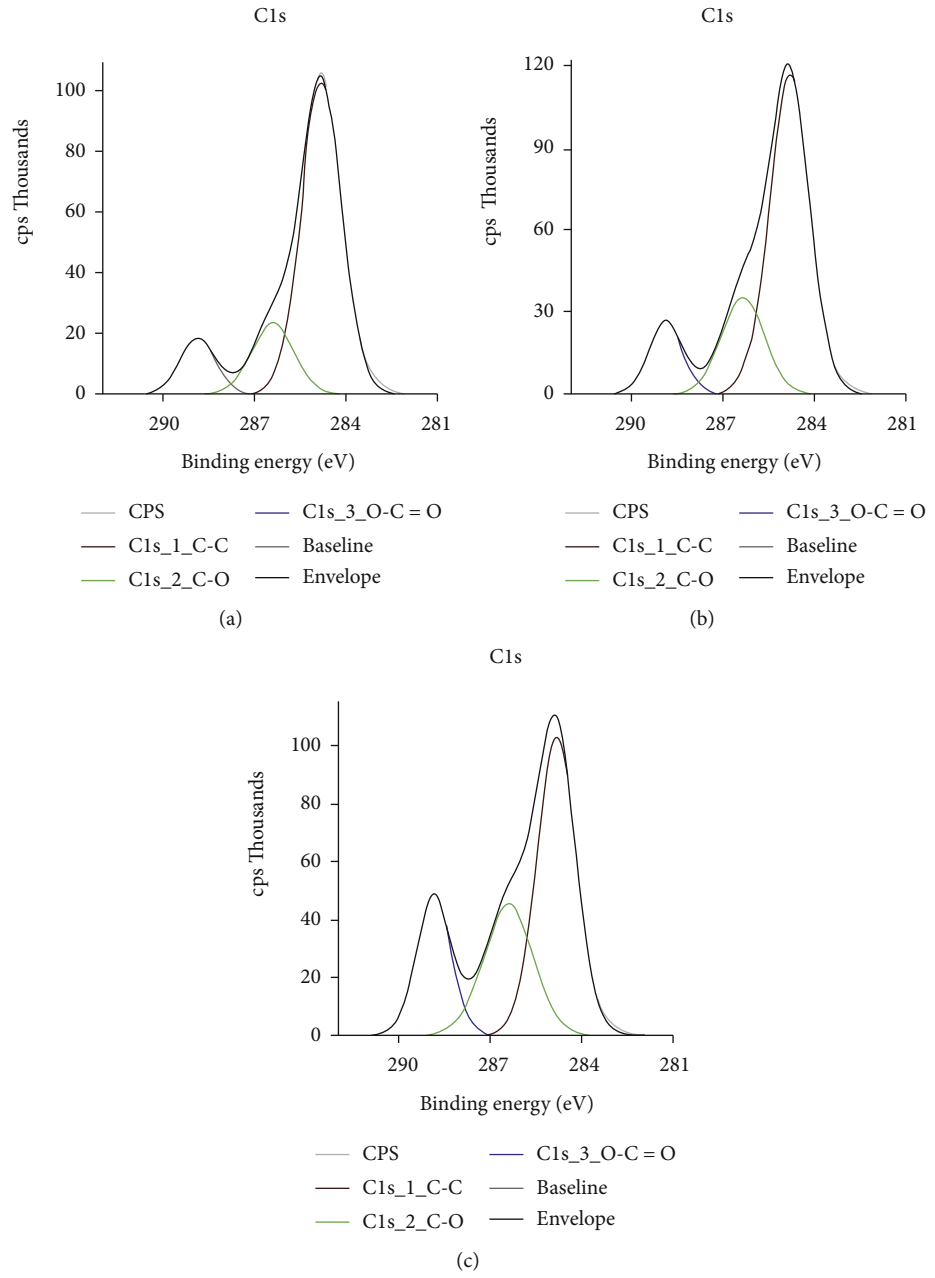

Figure 5: X-ray photo spectroscopy peaks in C1s and O1s orbitals: (a) neat PLA, (b) PLA-6%NCF composite, and (c) PLA-6%NCF-3%MA composite.

played a role in adequate dispersion of NCF in the PLA matrix resulting in capable load transfer from the PLA matrix to NCF [38].

Figure 4(c) indicates that incorporating NCF in PLA decreased impact strength up to 25% from 5.32 ± 0.04 kJ/m^2 to 4.01 ± 0.08 kJ/m^2 for the NCF-PLA composite. The addition of nanocellulose fibril decreases molecular mobility in the PLA matrix in turn reducing the energy absorption that decreases the impact strength of the NCF-PLA composite. Furthermore, the reduction of impact strength occurs because of inefficient stress transfer when nanocellulose fibril (NCF) is present as its presence obstructs the penetration of PLA between the nanofibrils. The enhancement in impact strength by the addition of 3% MA in 10%NCF-PLA can be noticed when compared to neat PLA as it is increases up to 15.3%. The MA as a coupling agent increased the interaction between NCF and PLA matrix resulting in strong interfacial adhesion and helped in effective load transfer. Also, the presence of MA causes the chain grafting between NCF and PLA matrix that increases the impact strength of composite due to effective energy absorption. The improvement in mechanical properties of the NCF-PLA composite is increased remarkably by the addition of MA which acts as interfacial modifier.

The carbon oxygen bond types were recognized by exposing the O1s and C1s regions of specimen by using

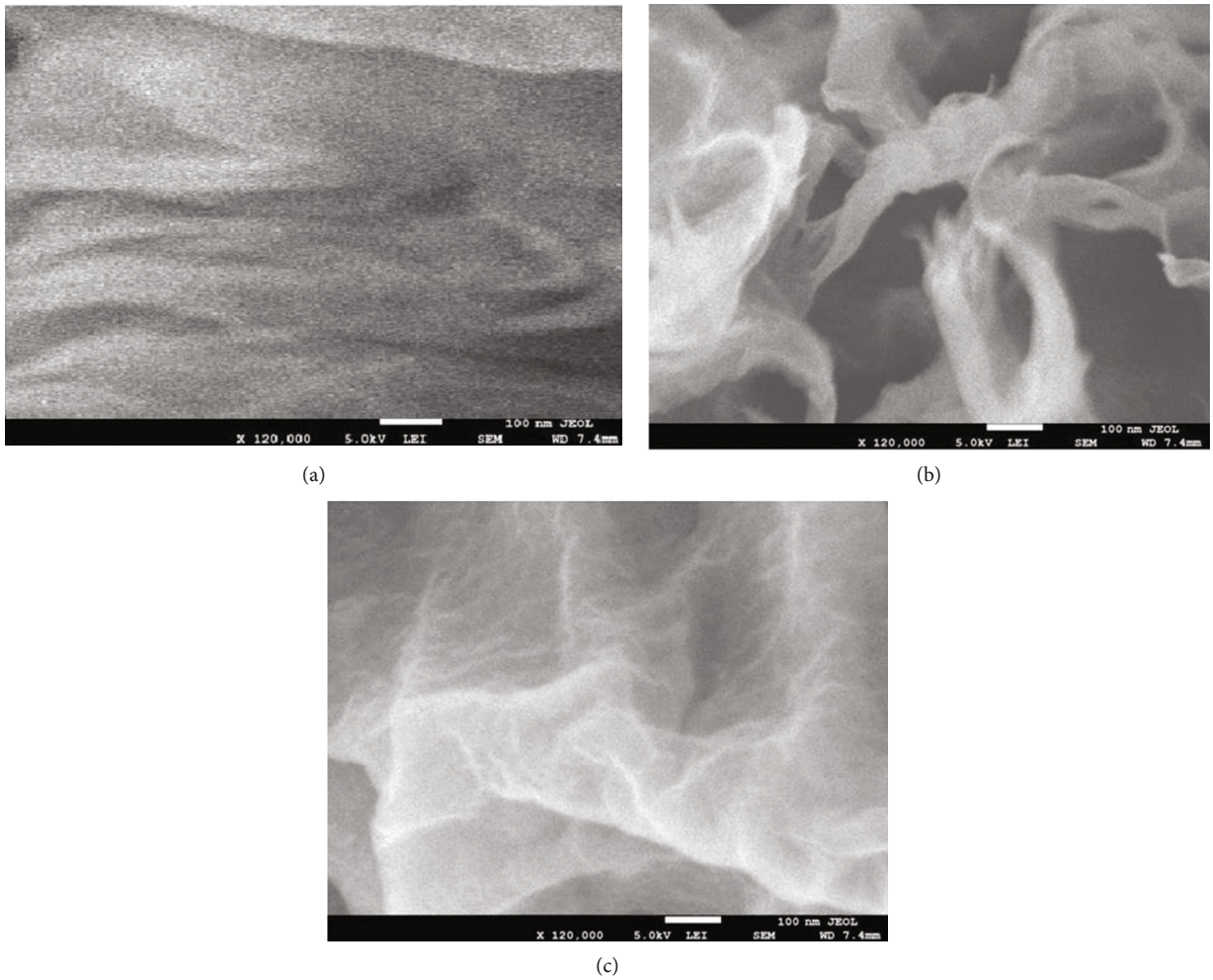

Figure 6: Fracture surface: (a) neat PLA, (b) PLA-6%NFC, and (c) PLA-6%NFC-3%MA.

XPS. Table 3 shows the bond type with their related energy of binding and atomic concentrations. Figure 5(a) demonstrates the peaks of pure PLA having corresponding intensities for functional groups related to the C1s region. The pure PLA polymer consists of covalent bond between oxygen, carbon, and hydrogen. In PLA matrix except hydrogen, 288.90 eV, 286.38 eV, 284.79 eV, 533.42 eV, and 532.09 eV binding energies are being presented for O–C=C bond, C–O bond, C–C bond, O=C bond, and O–C bond, respectively. Table 3 and Figure 5(b) illustrate that inclusion of 6% NCF in the PLA matrix elevates the carbon-oxygen bond concentration in the composite. The NCF contains higher level of carbon oxygen in its structure than PLA which increases the atomic % concentration of O-C=O to 9.67 atomic % from 8.98 atomic %. Moreover, in the PLA matrix, the atomic concentration of C-O bond increases to 15.35% from 13.36% due to the addition of NCF. In previous studies, it is shown that the corresponding binding energies of C-O bond and CC bond are 286.5 eV and 285.0 eV which correspond to our data [5]. The C-O, C-C, and C=O are the fundamental bonds of maleic anhydride (MA). The combinations of these bonds remarkably improve the grafting of carbon-oxygen bonds on the PLA matrix [38]. The presence of hydroxyl bonds in MA improves the properties of the NCF-PLA composite by increasing interaction between NCF and PLA. Figure 5(c) shows the increase in shoulder peak of the C1s region which might have occurred because of strong grafting creating better adhesion and crosslinking. The improvement can be attributed to the supplemented C-O bond concentration because of MA to 18.26 at.% from 13.36 at.% as shown in Table 3. Moreover, when compared to neat PLA, the O-C=O bond concentration increases to 13.69 at.% from 8.98 at.% as MA is added. Similar results were found with variable concentrations of NCF having 3% MA. The studies show that the MA might have shorter molecular chains than PLA making this as an attractive feature when it comes to effective creation of interfacial adhesion and crosslinking [39]. The effect is confirmed by analyzing the impact strength for the PLA-10%NCF-3%MA composite which improved 15% as shown in Table 2.

The tensile fracture surfaces of neat PLA, PLA-6%NCF, and PLA-6%NCF-3%MA are shown in Figure 6. Figure 6(a) shows smooth fracture arising from neat molecular attachment indicating the brittle nature of pure PLA. The addition of NCF in PLA demonstrated irregular surface pattern and voids in the cross section of fracture surface as shown in Figure 6(b) of PLA/6%NCF. The voids on fracture surface of PLA/6%NCF form because of pulling out of NCF

showing weak interfacial adhesion. Figure 6(c) shows the addition of 3% MA in PLA/6%NCF creates irregular fracture surface and decreases the voids as the reduction in debonding of NCF occurs due to increase in interfacial adhesion. The anhydride groups present in MA supplemented the adhesion by reacting with hydroxyl group on the NCF and PLA surfaces resulting in improvement of tensile and impact strength of the NCF-PLA-MA composite.

4. Conclusion

The study presents analysis of the PLA-NCF-MA composite developed by utilizing twin extruder. The addition of NCF in varying concentrations in PLA has shown minimum impact on degree of crystallinity in the NCF-PLA composite and does not act as nucleating agent. The presence of hydroxyl bonds in NCF increased hydrophilicity in the NCF-PLA composite. Furthermore, the molecular relaxation caused by MA increased the storage modulus and decreased tan δ. Also, the decrease in tan δ peak which resulted from molecular relaxation allows the PLA-NCF-MA composite to endure high energy of absorption. The addition of 3% MA increased the impact strength and % elongation at break illustrating the presence of strong interfacial adhesion between NCF and PLA. Moreover, the results show that interfacial adhesion increased due to the addition of MA which not only enhanced uniform dispersion of NCF but also reduced NCF pulling out from the PLA matrix.

Data Availability

All data are available within the manuscript.

Conflicts of Interest

The authors declare that they have no conflicts of interest.

Acknowledgments

The authors disclosed receipt of the following financial support for the research, authorship, and/or publication of this article. This project was funded by Deanship of Scientific Research (DSR) at King Abdulaziz University, Jeddah, under grant no. G1255-135-1440. The authors, therefore, acknowledge with thanks DSR for technical and financial support.

References

[1] E. Drumright, R. Gruber, and E. Henton, "Polylactic acid technology," *Advanced Materials*, vol. 12, no. 23, pp. 1841–1846, 2000.

[2] R. MacDonald, P. McCarthy, and A. Gross, "Enzymatic degradability of poly(lactide): effects of chain stereochemistry and material crystallinity," *Macromolecules*, vol. 29, no. 23, pp. 7356–7361, 1996.

[3] A. Mohanty, K. Misra, and G. Hinrichsen, "Biofibres, biodegradable polymers and biocomposites: An overview," *Macromolecules Materials Engineering*, vol. 276-277, no. 1, pp. 1–24, 2000.

[4] D. Feng, D. F. Caulfield, and A. R. Sanadi, "Effect of compatibilizer on the structure-property relationships of kenaf-fiber/polypropylene composites," *Polymer Composites*, vol. 22, no. 4, pp. 506–517, 2001.

[5] U. Saeed, M. Nawaz, and H. Al-Turaif, "Wood flour reinforced biodegradale PBS/PLA composite," *Journal of Composite Materials*, vol. 52, no. 19, pp. 2641–2645, 2018.

[6] A. Alemdar and M. Sain, "Biocomposites from wheat straw nanofibers: morphology, thermal and mechanical properties," *Composites Science and Technology*, vol. 68, no. 2, pp. 557–565, 2008.

[7] H. Yang, D. Gardner, and A. Nader, "Characteristic impact resistance model analysis of cellulose nanofibril-filled polypropylene composites," *Composites Part A Applied Science and Manufacturing*, vol. 42, pp. 2028–2034, 2011.

[8] J. Gardner, S. Oporto, and R. Mills, "Adhesion and surface issues in cellulose and nanocellulose," *Journal of Adhesion Science and Technology*, vol. 22, no. 5-6, pp. 545–567, 2008.

[9] P. Mathew, K. Oksman, and M. Sain, "Mechanical properties of biodegradable composites from poly lactic acid (PLA) and microcrystalline cellulose (MCC)," *Journal of Applied Polymer Science*, vol. 97, pp. 2014–2018, 2005.

[10] A. Ilyas, M. Sapuan, and L. Sanyang, "Nanocrystalline cellulose as reinforcement for polymeric matrix nanocomposites and its potential applications: a review," *Current Analytical Chemistry*, vol. 14, no. 3, pp. 203–208, 2018.

[11] A. Ilyas, M. Sapuan, and L. Sanyang, "Sugar palm nanofibrillated cellulose (Arenga pinnata (Wurmb.) Merr): effect of cycles on their yield, physic-chemical, morphological and thermal behaviour," *International Journal of Biological Macromolecules*, vol. 123, pp. 379–384, 2019.

[12] N. Bitinis, R. Verdejo, and P. Cassagnau, "Structure and properties of polylactide/natural rubber blends," *Materials Chemistry and Physics*, vol. 129, no. 3, pp. 823–831, 2011.

[13] P. Bordes, E. Pollet, and L. Ave'rous, "Nano-biocomposites: biodegradable polyester/nanoclay systems," *Progress in Polymer Science*, vol. 34, no. 2, pp. 125–155, 2009.

[14] A. Sorrentino, G. Gorrasi, and V. Vittoria, "Potential perspectives of bio-nanocomposites for food packaging applications," *Trends in Food Science and Technology*, vol. 18, pp. 84–95, 2007.

[15] A. L. Goffin, J. M. Raquez, and E. Duquesne, "From interfacial ring-opening polymerization to melt processing of cellulose nanowhisker-filled polylactide-based Nanocomposites," *Biomacromolecules*, vol. 12, no. 7, pp. 2456–2465, 2011.

[16] B. Dogu and C. Kaynak, "Behavior of polylactide/microcrystalline cellulose biocomposites: effects of filler content and interfacial compatibilization," *Cellulose*, vol. 23, pp. 611–622, 2016.

[17] A. Iwatake, M. Nogi, and H. Yano, "Cellulose nanofiber-reinforced polylactic acid," *Composites Science and Technology*, vol. 68, no. 9, pp. 2103–2106, 2008.

[18] K. Oksman, A. Mathew, and D. Bondeson, "Manufacturing process of cellulose whiskers/polylactic acid nanocomposites," *Composites Science and Technology*, vol. 66, no. 15, pp. 2776–2784, 2006.

[19] A. N. Frone, S. Berlioz, and J. F. Chailan, "Morphology and thermal properties of PLA-cellulose nanofibers composites," *Carbohydrate Polymers*, vol. 91, no. 1, pp. 377–384, 2013.

[20] M. Jonoobi, J. Harun, and P. Mathew, "Mechanical properties of cellulose nanofiber (CNF) reinforced polylactic acid (PLA)

prepared by twin screw extrusion," *Composites Science and Technology*, vol. 70, no. 12, pp. 1742–1747, 2010.

[21] S. Kalia, A. Dufresne, and B. M. Cherian, "Cellulose-based bio- and nanocomposites: a review," *International Journal of Polymer Science*, vol. 5, 35 pages, 2011.

[22] G. Siqueira, J. Bras, and A. Dufresne, "Cellulosic bionanocomposites: a review of preparation, properties and applications," *Polymers*, vol. 2, no. 4, pp. 728–765, 2010.

[23] H. A. Khalil, A. Bhat, and A. I. Yusra, "Green composites from sustainable cellulose nanofibrils: a review," *Carbohydrate Polymers*, vol. 87, no. 2, pp. 963–979, 2012.

[24] J. F. Zhang and X. Sun, "Mechanical properties of poly (lactic acid)/starch composites compatibilized by maleic anhydride," *Biomacromolecules*, vol. 5, pp. 1446–1451, 2004.

[25] A. C. Fowlks and R. Narayan, "The effect of maleated polylactic acid (PLA) as an interfacial modifier in PLA-talc composites," *Journal of Applied Polymer Science*, vol. 118, pp. 2810–2820, 2010.

[26] T. Yu, N. Jiang, and Y. Li, "Study on short ramie fiber/poly (lactic acid) composites compatibilized by maleic anhydride," *Composites Part A: Applied Science and Manufacturing*, vol. 64, pp. 139–146, 2014.

[27] D. Carlson, L. Nie, and R. Narayan, "Maleation of polylactide (PLA) by reactive extrusion," *Journal of Applied Polymer Science*, vol. 72, no. 4, pp. 477–485, 1999.

[28] L. Petersson and K. Oksman, "Biopolymer based nanocomposites: comparing layered silicates and microcrystalline cellulose as nanoreinforcement," *Composites Science and Technology*, vol. 66, no. 13, pp. 2187–2196, 2006.

[29] D. Plackett, "Maleated polylactide as an interfacial compatibilizer in biocomposites," *Journal of Polymers and the Environment*, vol. 12, pp. 131–138, 2004.

[30] A. K. Mohanty, M. Misra, and L. T. Drzal, "Surface modifications of natural fibers and performance of the resulting biocomposites: an overview," *Composite Interfaces*, vol. 8, no. 5, pp. 313–343, 2001.

[31] T. F. Salem, S. Tirkes, A. O. Akar, and U. Tayfun, "Enhancement of mechanical, thermal and water uptake performance of TPU/jute fiber green composites via chemical treatments on fiber surface," *E-Polymers*, vol. 20, pp. 133–143, 2020.

[32] K. Coskun, A. Mutlu, M. Dogan, and E. Bozaci, "Effect of various enzymatic treatments on the mechanical properties of coir fiber/poly (lactic acid) biocomposites," *Journal of Thermoplastic Composite Materials*, vol. 34, pp. 1066–1079, 2021.

[33] M. M. Kabir, H. Wang, K. T. Lau, and F. Cardona, "Chemical treatments on plant-based natural fibre reinforced polymer composites: an overview," *Composites Part B: Engineering*, vol. 43, no. 7, pp. 2883–2892, 2012.

[34] A. K. Bledzki and J. Gassan, "Composites reinforced with cellulose based fibres," *Progress in Polymer Science*, vol. 24, no. 2, pp. 221–274, 1999.

[35] L. A. Pothan, Z. Oommen, and S. Thomas, "Dynamic mechanical analysis of banana fiber reinforced polyester composites," *Composites Science and Technology*, vol. 63, pp. 283–292, 2003.

[36] N. Hameed, P. A. Sreekumar, and B. Francis, "Morphology, dynamic mechanical and thermal studies on poly(styrene-co-acrylonitrile) modified epoxy resin/glass fibre composites," *Composites Part A: Applied Science and Manufacturing*, vol. 38, no. 12, pp. 2422–2432, 2007.

[37] A. K. Rana, B. C. Mitra, and A. N. Banerjee, "Short jute fiber-reinforced polypropylene composites: dynamic mechanical study," *Journal of Applied Polymer Science*, vol. 71, no. 4, pp. 531–539, 1999.

[38] M. S. Nicole and M. Laurent, "Surface chemistry changes of weathered HDPE/wood-flour composites studied by XPS and FTIR spectroscopy," *Polymer Degradation and Stability*, vol. 1, pp. 1–9, 2004.

[39] J. Z. Lu, Q. Wu, and S. Harold, "Chemical coupling in wood fiber and polymer composites: a review of coupling agents and treatments," *Wood and Fiber Science*, vol. 32, pp. 88–99, 2000.

Hindawi
Journal of Nanomaterials
Volume 2021, Article ID 3913601, 15 pages
https://doi.org/10.1155/2021/3913601

Research Article

Investigations on Microstructure, Mechanical, Thermal, and Tribological Behavior of Cu-MWCNT Composites Processed by Powder Metallurgy

B. Stalin,[1] **M. Ravichandran**,[2] **Alagar Karthick**,[3] **M. Meignanamoorthy**,[2] **G. T. Sudha**,[4] **S. Karunakaran**,[1] **and Murugesan Bharani**[5]

[1]*Department of Mechanical Engineering, Anna University, Regional Campus Madurai, Madurai, 625 019 Tamil Nadu, India*
[2]*Department of Mechanical Engineering, K. Ramakrishnan College of Engineering, Trichy, 621 112 Tamil Nadu, India*
[3]*Department of Electrical and Electronics Engineering, KPR Institute of Engineering and Technology, Coimbatore, 641 407 Tamil Nadu, India*
[4]*Department of Mechanical Engineering, Government Polytechnic College, Coimbatore, 641 014 Tamil Nadu, India*
[5]*School of Textile Leather and Fashion Technology, Kombolcha Institute of Technology, Wollo University, South Wollo, 208 Kombolcha, Ethiopia*

Correspondence should be addressed to Murugesan Bharani; bharani.murugesan@kiot.edu.et

Received 17 June 2021; Revised 5 August 2021; Accepted 13 August 2021; Published 26 August 2021

Academic Editor: Sami-Ullah Rather

Copper (Cu) metal matrix composite (MMC) was developed with multiwall carbon nanotubes (MWCNT) as reinforcement by using powder metallurgy (PM) technique. The composition of the composites is Cu, Cu-4 wt% MWCNT, Cu-8 wt% MWCNT, and Cu-12 wt% MWCNT. The Cu and MWCNTs were blended for 6 hours in a ball mill and compacted at a 6 ton pressure to form green compacts using a 10 ton hydraulic press. Using a tubular furnace, the heat was applied at 900°C for 1.5 hours to impart strength and integrity to the green compacts. Milled composite blends were studied to analyze its characterization through SEM and EDAX analysis. Characterization studies such as SEM and EDAX confirm the presence and even dispersion of Cu and MWCNT constituents. The relative density, hardness, and ultimate compressive strength have been studied, and a remarkable improvement in properties has been obtained by the inclusion of MWCNTs. The composites reinforced by 8 and 12 wt% MWCNT were recorded with low thermal conductivity than the Cu composite reinforced by 4 wt% MWCNT. A wear study was analyzed using Taguchi technique for determining the effect caused by the wear test parameters and MWCNT content on wear rate. The optimized parameter that contributes minimum wear rate was identified as 12 wt% MWCNT content, 10 N applied load, 2 m/s sliding velocity, and 500 m sliding distance. Based on the obtained results, it could be understood that the produced composites can be utilized for various applications like relay contact springs and switchgear, rotor bars, and bus bars.

1. Introduction

Composite fabrication generally incorporates combining the reinforcement with matrix and wetting them. By doing like that, matrix-reinforcement combines collectively into an inflexible material [1]. Because of their superior mechanical, tribological, electrical, and thermal properties, metal matrix composites (MMC) found their widespread applications in ever-growing fields such as aerospace, automotive, and structural [2, 3]. Metal matrix composites (MMCs) are composed of a metallic matrix like Al, Mg, Fe, Cu, and a dispersed ceramic (oxides, carbides, and nitrides). Most MMCs are at a standstill in the improvement stage and are not so extensively established. The merits of MMCs are better strength-to-density ratios, good opposition to wear and corrosion, radiations and fatigue, less creep rate and coefficients of thermal expansion, no moisture absorption, noninflammability, and higher electrical and thermal conductivities [4]. Copper

Table 1: Sample compositions of composite preparation.

Sample no.	Copper (Cu), wt%	Multi-walled carbon nanotube (MWCNT), wt%
1	100	0
2	96	4
3	92	8
4	88	12

has outstanding properties such as electrical conductivity, thermal conductivity, workability, and corrosion resistance. Due to these unique properties, copper is expected to be an outstanding material for manufacturing parts in industries in connection with water supply and electrical and thermal industries and has broad applications in gas turbine nozzles, rocket engines, electrical switches, combustion chamber wall liners, electronic packages, contact breakers, cooling systems, heat exchangers, rotating neutron targets, and integrated circuits. Although copper possesses good properties because of its ductile nature, it has poor mechanical properties and this restricts structural applications [5–7]. To overcome the aforementioned disadvantage, copper is reinforced with Al_2O_3, SiC, TiO_2, Gr, ZrO_2, Ti, TiB, TiB_2, TiC, and fly ash particles to form copper matrix composites which improved the mechanical properties [2, 8–13]. Most manufacturing companies focus on copper matrix composites to produce several components due to the supreme properties over other matrix composites [14]. Carbon nanotubes (CNTs) are such a reinforcement that is well known for its one-dimensional quasicarbon structures with greater aspect ratio and better electrical, thermal, and mechanical properties. The strength of the matrix materials has been found to get improved in association with CNT reinforcements, and hence, the CNT reinforced composites are extensively used in automotive and aerospace applications [15, 16]. In view of the excellent atomic structure and intriguing properties, the researchers heeded over the investigations on CNT. As yet, CNT is the utmost exclusive and adaptable materials exposed in the world, and this has been concluded from the theoretical and experimental results obtained [17]. A substantial attempt to synthesize better Cu-CNT composites is therefore on the rise [18, 19]. Though the powder metallurgy (PM) manufacturing process is an older technique to fabricate MMCs, in the recent era, the manufacturing industries are much attracted towards the PM fabricating process due to the various merits such as components with net shape and no wastages and better mechanical properties [20]. Excellent mechanical properties and fine microstructure can also be achieved without any defects through PM manufacturing process [21, 22].

Liu et al. [23] formed Cu-CNT properties with enhanced strength and ductility, and the better interfacial bonding between Copper and CNT was identified to be the reason behind improved properties. Wang et al. [24] investigated the properties and enhancements of Cu-CNT composites' interfacial interaction and found that yield strength, plasticity, and electrical conductivity were improved with the increase in CNT reinforcement. The predominant increase in yield strength and plasticity was justified by the dislocation theory and the strengthening mechanisms. Yang et al. [25] investigated the mechanical and electrical properties of CNT reinforced copper composites, and the maximum values were obtained in composite with 2.5 vol% CNT reinforcement. Alam et al. [26] studied the wear behavior of stir cast aluminium/SiC nanocomposites and reported that addition of reinforcement increases the wear resistance. Previous reports proven that MWCNTs are remarkably stronger than the impressively single-walled carbon nanotube. Also, the single wall CNT is very useful for electrical and electronics applications. Hence, for strength enhancement, we have used MWCNT as reinforcement in this study.

An extensive literature review indicates that the production of Cu-CNT composites through PM technique is rare. Thus, this study was endeavored to explore the characteristics and properties of Cu-MWCNT composites after developing using the PM method. The influence of MWCNT reinforcement on the hardness, density, compressive strength, and thermal conductivity of the fabricated composites was stated. Wear property of the composites was tested in a pin-on-disc wear tester. The impact of MWCNT weight percentage and the wear test parameters such as load applied, sliding distance, and sliding velocity on the wear rate of Cu-MWCNT composites was analyzed using Taguchi analysis, and the optimized parameter levels for minimum wear rate were also identified.

2. Experimental Details

The chosen copper matrix and MWCNT reinforcement powders of current investigation were procured from Modern Scientific, Madurai, India. The MWCNTs were added to the step of 4, 8, and 12 weight percentages to yield the different compositions. The size of the copper powder is 300 μm, and MWCNT is 50 μm. The proportions of MWCNT particles added to Cu powders to form composites are depicted in Table 1, and the fabrication process setup and sequence of processes used are shown in Figure 1.

In the present investigation, the Cu/MWCNT composites were synthesized through the PM technique as mentioned by the following procedure. At 600 rpm, the mixing of Cu and MWCNTs was achieved by a planetary ball mill with a stainless steel mixing jar consisting of 10 mm diameter stainless steel balls, and the milling was performed for a duration of 6 hours under argon atmosphere. The BPR maintained was 5 : 1, and pure alcohol was added to the mixture so as to control self-cold welding of powders. Milling was also performed to establish reduction in the particle size of powders and thereby improving the homogenization of powders. The density of the used Cu and MWCNT powders was 8.9 g/cc and 1.8 g/cc, respectively, and these density values were considered in the calculation of relative density. Once the milling was complete, each composition was compacted in a hydraulic press with a capacity of 10 Ton. By using a cylindrical punch die arrangement, the well-blended Cu and MWCNT powders were compacted to green compacts of cylindrical shape at room temperature. The compaction was made at a pressure of 6 tons, and the

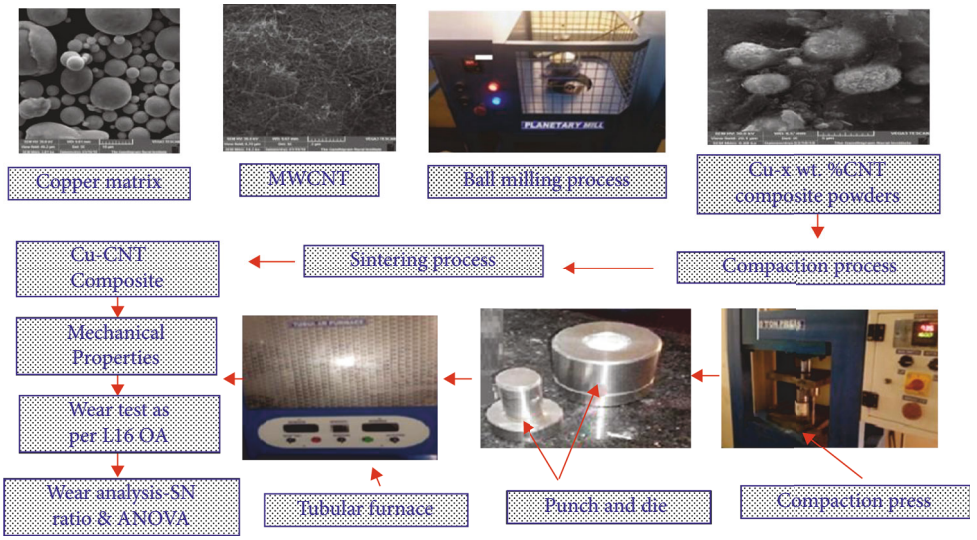

Figure 1: Fabrication process setup and sequence of processes used for the present work.

Table 2: Parameters with levels chosen for wear rate analysis.

Parameters	Symbols	Unit	Level 1	Level 2	Level 3	Level 4
Weight percentage of MWCNT	A	%	0	4	8	12
Load applied	B	N	10	20	30	40
Sliding velocity	C	m/s	1	2	3	4
Sliding distance	D	m	500	1000	1500	2000

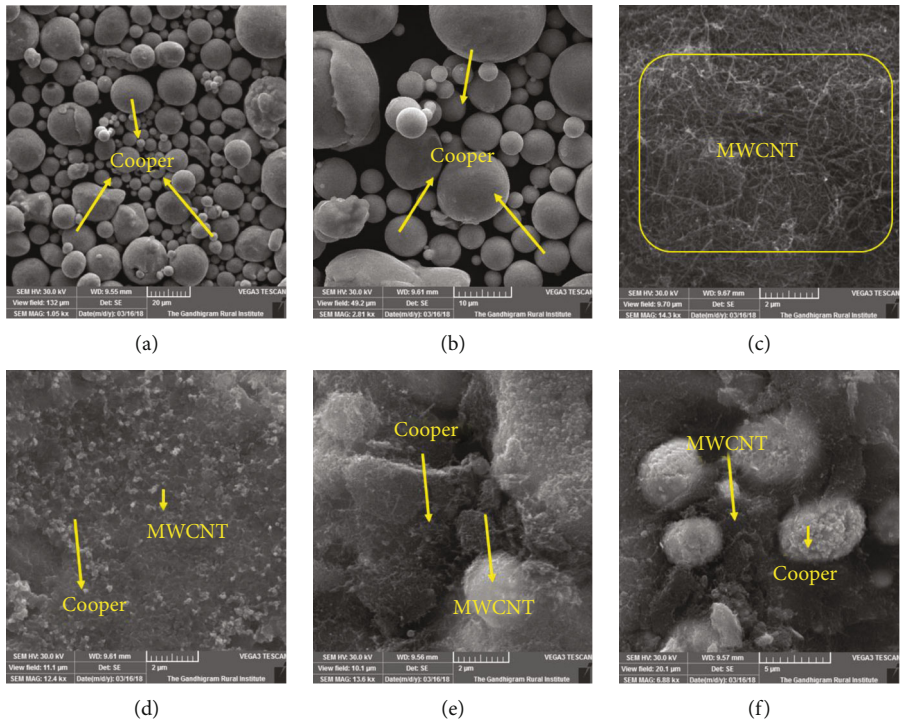

Figure 2: SEM micrographs. (a, b) SEM image of pure copper; (c) SEM image of multiwalled carbon nanotubes; (d) Cu–4 wt% MWCNT; (e) Cu–8 wt% MWCNT; (f) Cu–12 wt% MWCNT milled powders.

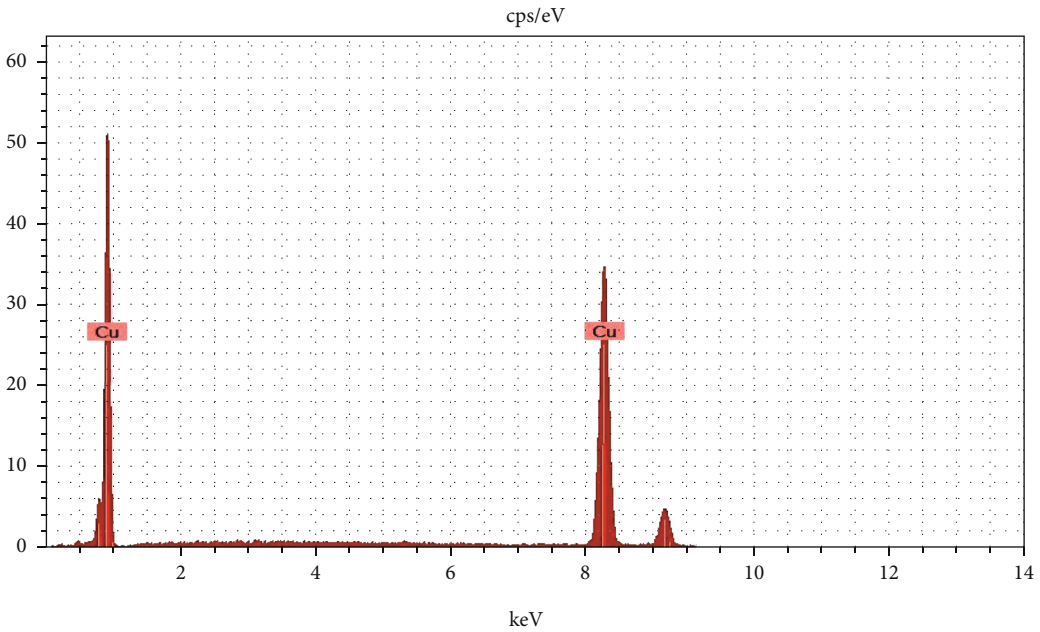

(a)

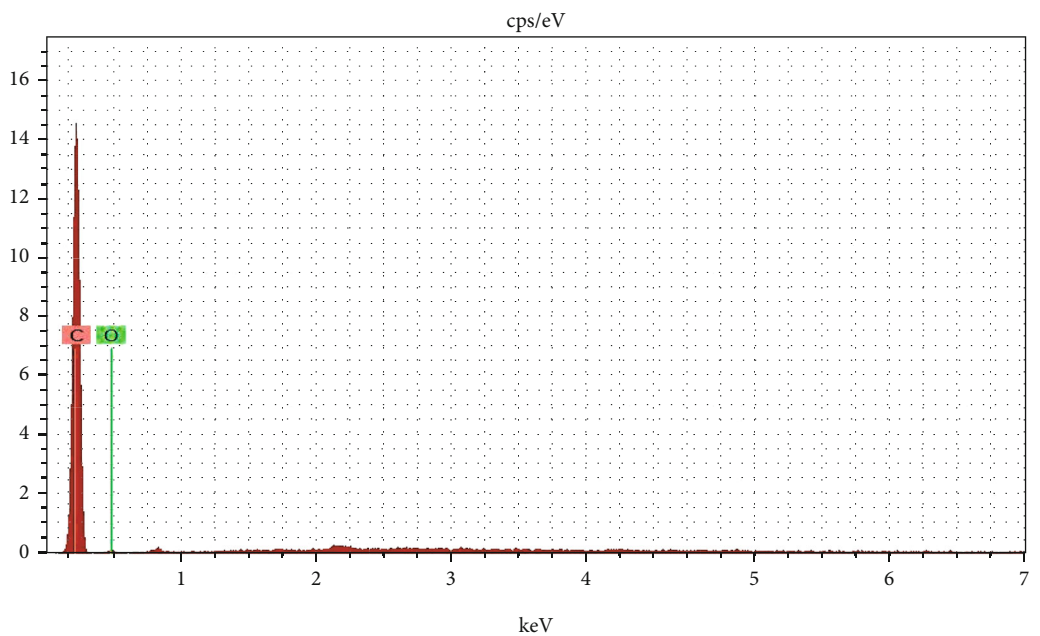

(b)

Figure 3: Continued.

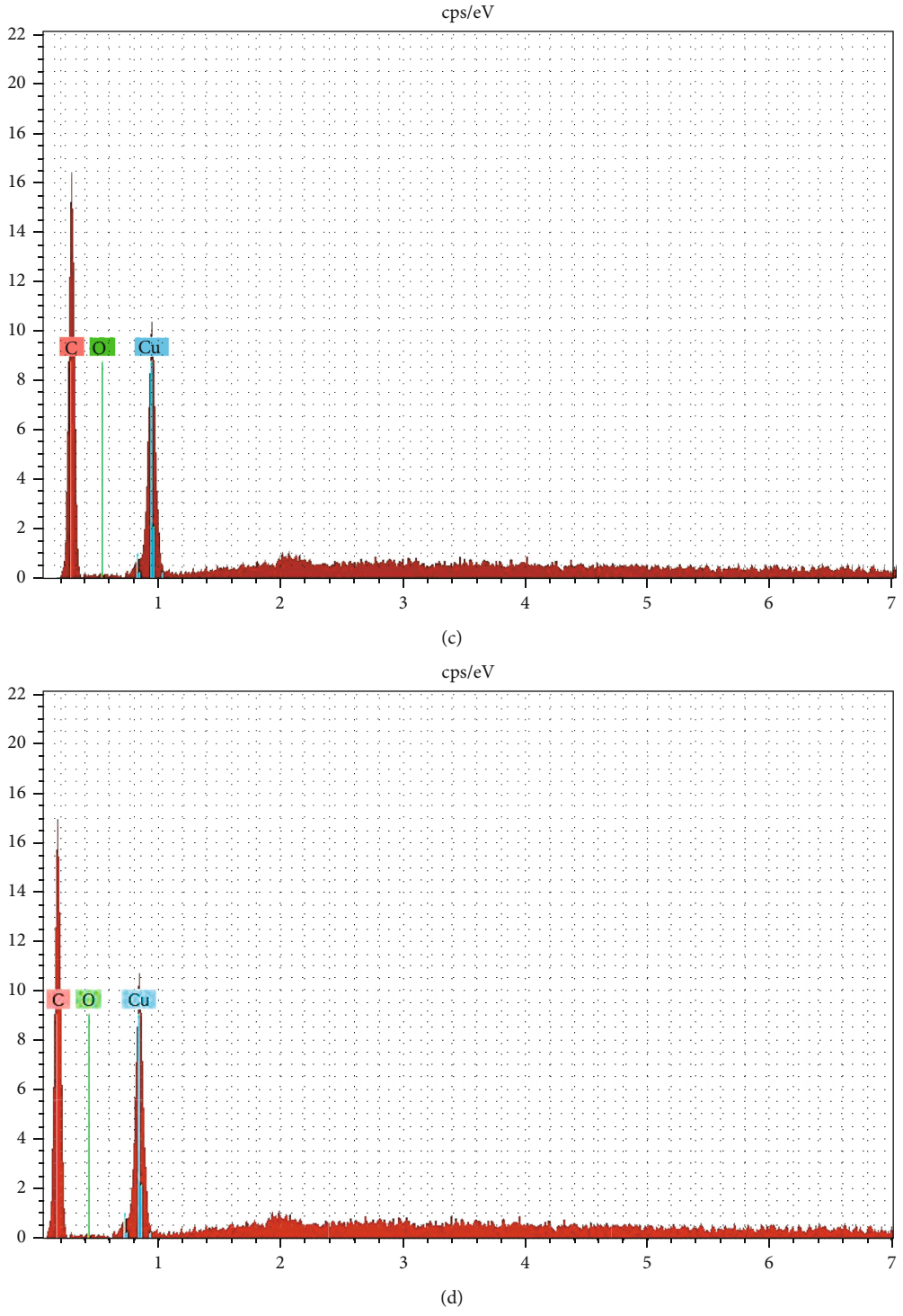

Figure 3: EDX Analysis (a) EDAX of Cu; (b) MWCNT; (c) Cu–4 wt% MWCNT; (d) Cu–8 wt% MWCNT milled powders.

compaction dwell time was about 12 seconds and the resultant cylindrical green compacts were of 10 mm diameter and 10 mm height.

Sintering was done in a tubular furnace at 900°C much below the melting point of copper, to integrate the particles and improve the strength of the green compacts produced. The sintering temperature (900°C) was achieved inside the furnace by heating at a rate of 5°C/min for 1.5 hours. Sintering was performed in a controlled argon atmosphere to produce clean parts without products of oxidation and to prevent surface contamination from atmospheric air. The sintered samples were tested for hardness by using Vickers hardness testing machine by following ASTM standard E384-08 [27]. The compressive strength was evaluated as

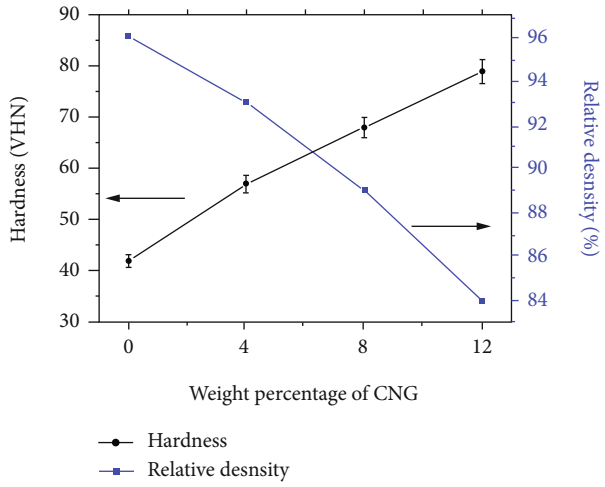

Figure 4: Cu-MWCNT composite hardness and relative density.

per ASTM standard E9-89a using a 10 Ton Universal testing machine [28]. By recording the power meter reading and temperature with respect to time, the thermal conductivity values of the produced composites were determined in W/mK. Three sets of readings were noted for all the experiments, and the average of these three values was calculated for investigation. The wear rate of the composites was evaluated by adopting ASTM G-99 standard procedure using a pin-on-disc apparatus. During experimentation, the Cu-CNT wear test specimens and EN-31 hardened steel with 60 HRC were employed to be the pin and disc material. The surfaces were mirror-polished to enable properly engaged contact between the counterparts and thereby ensuring uniform wear all over the surface. The parameters considered for wear rate analysis were MWCNT weight percentage, load applied, sliding speed, and sliding distance, and for each parameter, four levels were chosen as depicted in Table 2. By L16 orthogonal array, the experimental run for the study was framed and the effect of these parameters on the wear rate was analyzed by Taguchi analysis.

3. Results and Discussion

3.1. Microstructural Characterization. As obtained, pure Cu powder was subjected to SEM examination and the micrographs that clearly illustrate the three-dimensional spherical shaped copper powder particles are shown in Figures 2(a) and 2(b). Figure 2(c) reveals the needle-like one-dimensional acicular-shaped MWCNT powder particles. Figures 2(d)–2(f) exhibit the SEM micrograph of the Cu + 4 wt%MWCNT, Cu + 8 wt%MWCNT, and Cu + 12 wt %CNT milled powders. The occurrence of CNT particle is evidently noticeable in all the samples of Figures 2(d)–2(f). The SEM image in Figure 2(d) shows that the MWCNT particulates were more evenly distributed among the copper particles and are homogenous. Figures 2(e) and 2(f) reveal the occurrence of MWCNT clusters in between the copper matrixes in Cu–8 wt% MWCNT and Cu–12 wt% MWCNT composites, and this confirms the possibility of reinforcement accumulation formation at higher reinforcement content. The shape change effect and cold welding [29] of MWCNT with copper particles that happened during ball milling were understood from Figures 2(e) and 2(f).

3.2. Energy Dispersive X-Ray Analysis. The compositional analysis of the As procured pure Cu and MWCNT powders, and milled Cu-MWCNT powders were done by EDAX, and the result supplements the even dispersal observation made by SEM micrographs. The images displayed in Figures 3(a)–3(d) indicate the occurrence of peaks equivalent to the presence of pure Cu and MWCNT. The higher peaks correspond to the main content copper in the composite powders. The even mixing and homogenous dispersal of MWCNT particles in Cu particles were substantiated by the obtained MWCNT weight percentage from Figures 3(c) and 3(d).

3.3. Relative Density and Hardness of Cu-MWCNT Composites. The theoretical and experimental density of the composites was calculated by following the rule of mixtures and Archimedes principle, respectively. From the calculated values, the relative density values of the copper and Cu-MWCNT composites were calculated. The relative density of the composites was depicted in the graph notified in Figure 4. From the graph in Figure 4, it was noted that the relative density values declined with the addition of more MWCNT content and the Cu-12% MWCNT composite exhibited the lowest relative density values. Increasing the wt% of MWCNT beyond 10 causes severe decline in the curve, and this severe declining effect on the relative density may be possible because of the accumulation of CNT particles at a higher reinforcement weight percentage that causes deprived bonding of CNT with the Cu matrix [16].

Figure 4 also depicts the hardness of copper and Cu-MWCNT composites with respect to the different MWCNT percentages loaded, and the hardness values were found to get enhanced with the increase in MWCNT content. The hardness enhancement is accredited to the strengthening effect imposed by the dispersal of highly strengthened MWCNT particles in the copper matrix. The increased amount of CNT particles with high strength enhanced the hardness of the composite progressively [30]. The increase in hardness improved the bonding between the copper and MWCNT particles. Numerous researchers investigated and explained the correlation that exists between the hardness and strengthening effect of the CNT-embodied composites. Akbarpour et al. [27] fabricated CNT-reinforced composites with elevated hardness values, and the hardness improvement with incorporation of CNT particles may be due to the underlying conditions: (i) reduction in grain size, (ii) increase in dislocation density, (iii) decrease in pore size, and (iv) work hardening of powders during milling. Besides outstanding interfacial bonding, hardness may be improved because of the prevention of dislocation movement due to CNT inclusion as per Hall-patch and Orowan strengthening phenomena. The improvement of hardness in Cu-CNT composites is due to excellent physical bonding between Cu and CNT at the interface. Due to grain improvement, particle strengthening and load bearing ability of hard

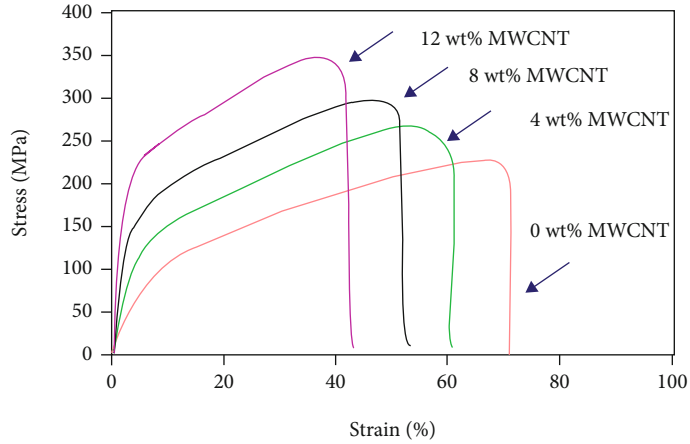

Figure 5: Stress-strain curve of Cu-MWCNT composite.

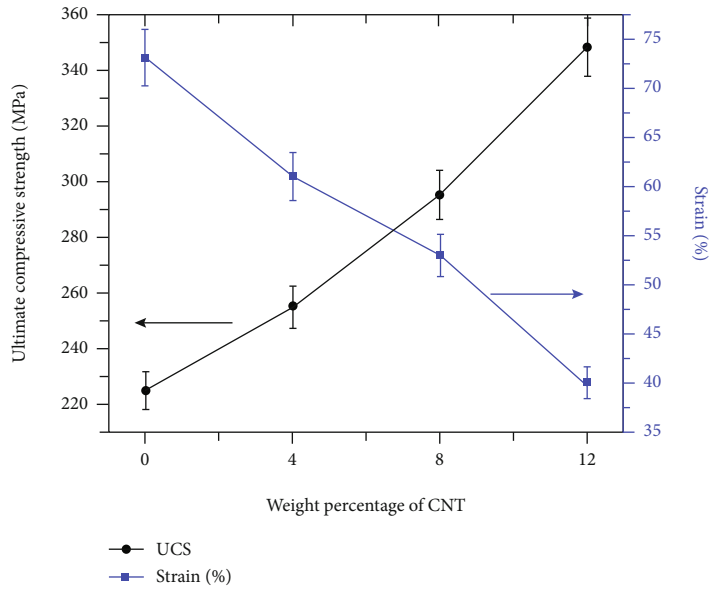

Figure 6: Effect of Cu-MWCNT on compression strength.

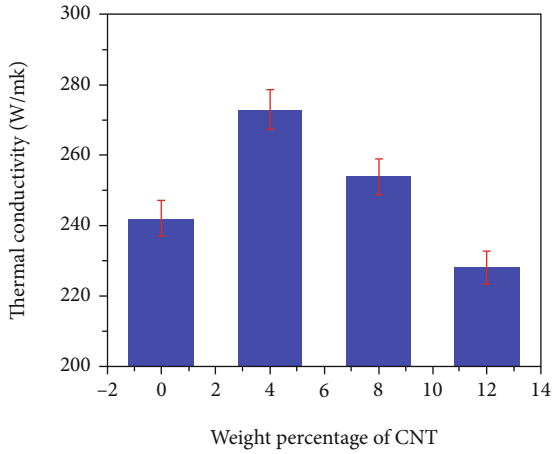

Figure 7: Effect of Cu-MWCNT on thermal conductivity.

reinforcement particle with matrix composites hardness enhanced [31].

3.4. Compressive Strength. The stress-strain curves drawn out with the values attained from the compression test carried out on Cu, Cu–4 wt% MWCNT, Cu–8 wt% MWCNT, and Cu–12 wt% MWCNT composites are illustrated in Figure 5. The compression strength of the Cu-MWCNT composites was better when compared with copper and on account of the progressive inclusion of MWCNT reinforcement; 33% enhancement in compressive strength was recorded. The superior molecular level mixing of matrix and reinforcement particles and the occurrence of better distribution impacted the stress-strain relationship [30]. The occurrence of strengthening accompanied by the load transfer between the copper and high strength MWCNT particles at their interfaces also leads to improvement in compressive strength of the composites. The fact that

Table 3: Wear rate and their corresponding *S*/*N* ratio.

Experiment number	Weight percentage of MWCNT	Applied load (N)	Sliding velocity (m/s)	Sliding distance (m)	Wear rate $(mm^3/Nm) \times 10^{-6}$	*S*/*N* ratio
1	0	10	1	500	44.59	-32.9847
2	0	20	2	1000	48.62	-33.7363
3	0	30	3	1500	53.49	-34.5655
4	0	40	4	2000	57.64	-35.2145
5	4	10	2	1500	26.95	-28.6112
6	4	20	1	2000	29.54	-29.4082
7	4	30	4	500	33.52	-30.5061
8	4	40	3	1000	36.74	-31.3028
9	8	10	3	2000	7.13	-17.0618
10	8	20	4	1500	10.77	-20.6443
11	8	30	1	1000	17.55	-24.8855
12	8	40	2	500	13.92	-22.8728
13	12	10	4	1000	4.59	-13.2363
14	12	20	3	500	4.12	-12.2979
15	12	30	2	2000	5.16	-14.253
16	12	40	1	1500	6.47	-16.2181

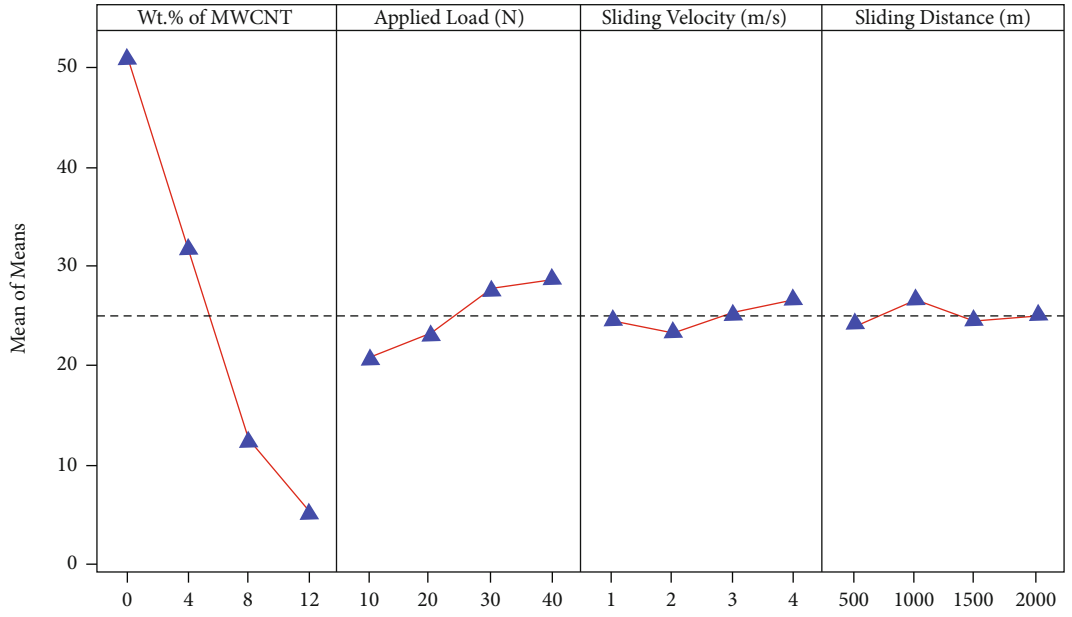

Figure 8: Main effect plot for mean (wear rate).

enhanced dislocation density tends to improve the compressive properties was because of thermal mismatch between matrix and reinforcement [32] and Orowan strengthening mechanism and dispersion hardening effect [33].

Figure 6 shows that the ultimate compressive strength increases with increasing MWCNT reinforcement weight percentage, and the results implied that the compressive strength of Cu-MWCNT composites was superior than the copper matrix. The augmentation of ultimate compressive strength was because of the noteworthy causes such as grain refinement, load transfer from Cu matrix to MWCNT reinforcement, and Orowan strengthening mechanism. Higher plastic deformation and strain hardening also contributed to greater compression strength. It is also well proved by many researchers that the addition of reinforcement content improves the compressive strength [15, 17]. The main significant cause for compressive strength improvement is well and fine dispersion of MWCNT particles with matrix.

3.5. Thermal Conductivity. Figure 7 depicts the influence made by the MWCNT reinforcement particles on the thermal conductivity Cu-MWCNT composites. The graph illustrated that the maximum thermal conductivity was recorded with the composite having 4 wt% MWCNT. The uniform

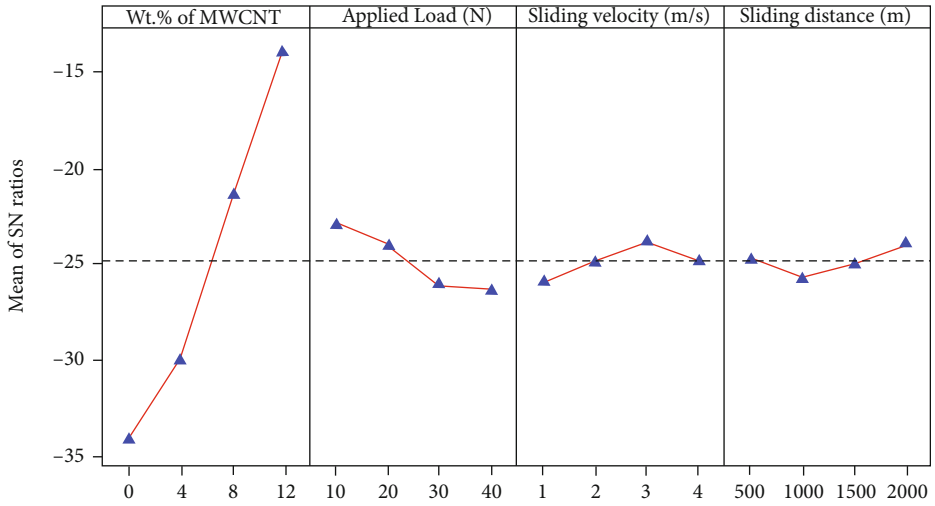

Figure 9: Main effect plot for *S/N* ratios (wear rate).

Table 4: Response table for the signal to noise ratios (smaller is better).

Level	Weight percentage of MWCNT	Applied load (N)	Sliding velocity (m/s)	Sliding distance (m)
1	-34.13	-22.97	-25.87	-24.67
2	-29.96	-24.02	-24.87	-25.79
3	-21.37	-26.05	-23.81	-25.01
4	-14.00	-26.40	-24.90	-23.98
Delta	20.12	3.43	2.07	1.81
Rank	1	2	3	4

Table 5: Response table for means.

Level	Weight percentage of MWCNT	Applied load (N)	Sliding velocity (m/s)	Sliding distance (m)
1	51.085	20.815	24.537	24.038
2	31.688	23.262	23.662	26.875
3	12.343	27.430	25.370	24.420
4	5.085	28.692	26.630	24.868
Delta	46.000	7.877	2.968	2.837
Rank	1	2	3	4

and even dispersion of MWCNT reinforcement and also the existence of better interfacial bonding contributed to the improvement in thermal conductivity. Beyond 4 wt%, the addition of MWCNT particles and the thermal conductivity experiences the reverse trend and declines with the addition of 8 and 12 wt% MWCNT reinforcement particles. Furthermore, increasing the MWCNT weight percentage up to 12 wt%, the thermal conductivity value decreases drastically. This significant lessening of thermal conducting property with the more weight percentage of MWCNT reinforcement addition is justified by the following reasons:

(i) The agglomerated MWCNTs which were held together as a bunch failed to maintain the contact with the copper matrix, and hence, the higher weight percentage of MWCNTs cannot subsidize the thermal conducting effect

(ii) An agglomeration of MWCNT may tempt the tube-tube interface, and this bundling separates the CNTs into ropes and offers the inner tube dispersion of phonons; therefore, a noteworthy reduction in the thermal conductivity occurred [28, 34]

(iii) The heat flow transformation in the composites was hindered due to the back dispersion of phonons in the composites which were caused by clustering effect [35]. Nevertheless, in this study, it is clear that thermal conductivity of copper matrix is superior than MWCNT particle; this is the most important reason to beg off in the composite thermal conductivity

3.6. Taguchi Analysis: Wear Rate versus wt% of MWCNT, Applied Load, Sliding Velocity, and Sliding Distance. This wear study conducted to determine the optimized parameter levels for achieving the minimum wear rate followed the L16 orthogonal array, and the experimental values acquired were interpreted using MINITAB software. The optimization is done by spotting the level of the parameter that yields the preferred quality characteristic, and for the current investigation, "the smaller the better" quality characteristic was chosen. The experimental observations are shown in Table 3, and the *S/N* ratios are obtained by dividing the mean (signal) to the standard deviation (noise). The maximum wear rate of 57.64×10^{-6} (mm^3/Nm) was recorded by the pure copper without MWCNT particles, and the minimum wear rate of 4.12×10^{-6} (mm^3/Nm) was observed in the sample with 12 wt% MWCNT. These values illustrate the leading control exhibited by the percentage of MWCNT reinforcement over the wear rate of the Cu-MWCNT composites. The property wear resistance is always related and directly proportional to its hardness as indicated by Archard's law [36]. The high hardness exhibited by the composite

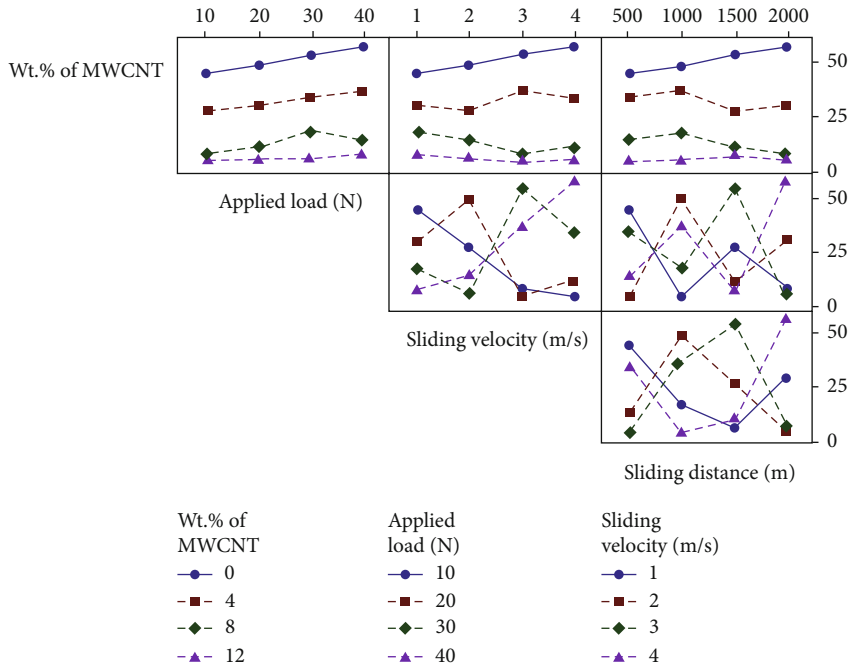

Figure 10: Interaction plot showing the interaction effect caused by input parameters on wear rate.

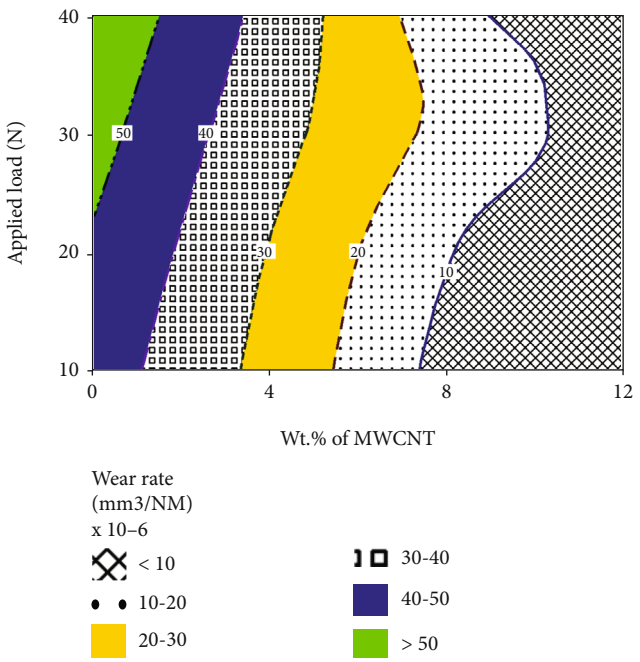

Figure 11: Contour plot showing wear rate with the combined effect of wt% of MWCNT and applied load.

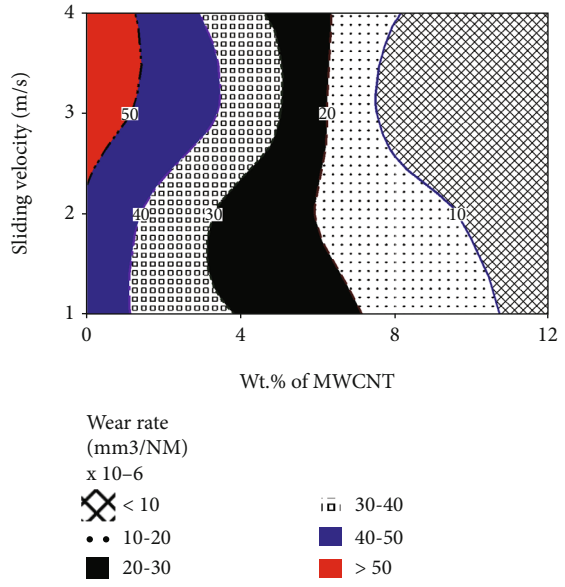

Figure 12: Contour plot showing wear rate with the combined effect of wt% of MWCNT and sliding velocity.

with 12 wt% MWCNT thereby explicates its high wear resistance behavior.

The main effect plots portray the influence made by the process input parameters over the response. The nature of lines observed in the main effect plot elucidates the influence level. The parameter that contributes a highly inclined line will be proclaimed as the most influential parameter, and the parameter with a plot nearer to the horizontal axis will be the least influential one. From the plots in Figures 8 and 9, the addition of MWNT wt% was recognized to be the predominant parameter to affect wear rate. The parameters sliding velocity and sliding distance were recognized as the least significant parameters. These results were also substantiated by the delta and rank values in Tables 4 and 5. The parameter wt% of MWCNT with the highest rank is the most significant parameter followed by applied load, sliding velocity, and sliding distance. From the main effect plots, the optimized parameter levels that contribute minimum wear rate were identified as 12% MWCNT content, 10 N applied load,

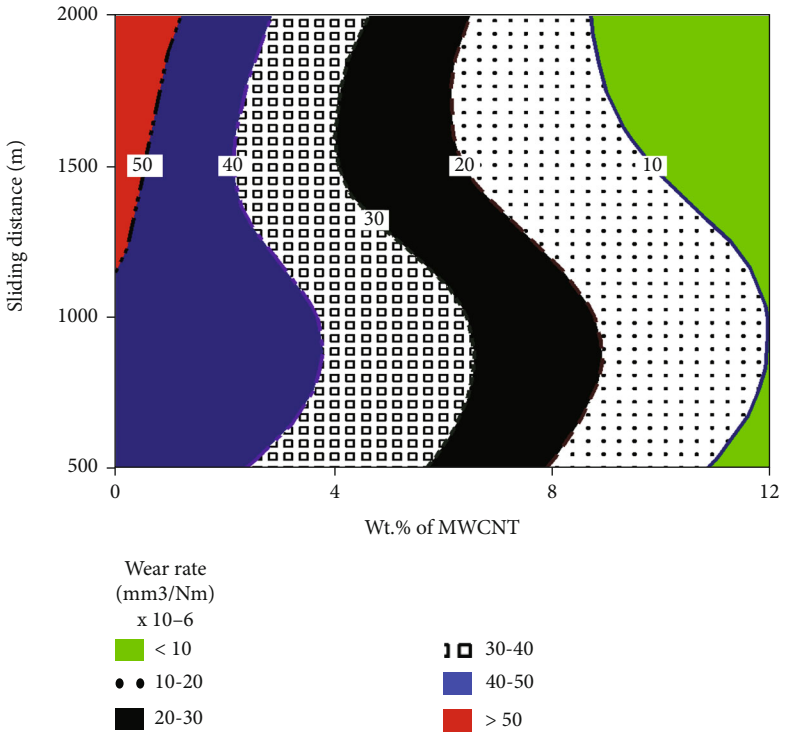

Figure 13: Contour plot showing wear rate with the combined effect of wt% of MWCNT and sliding distance.

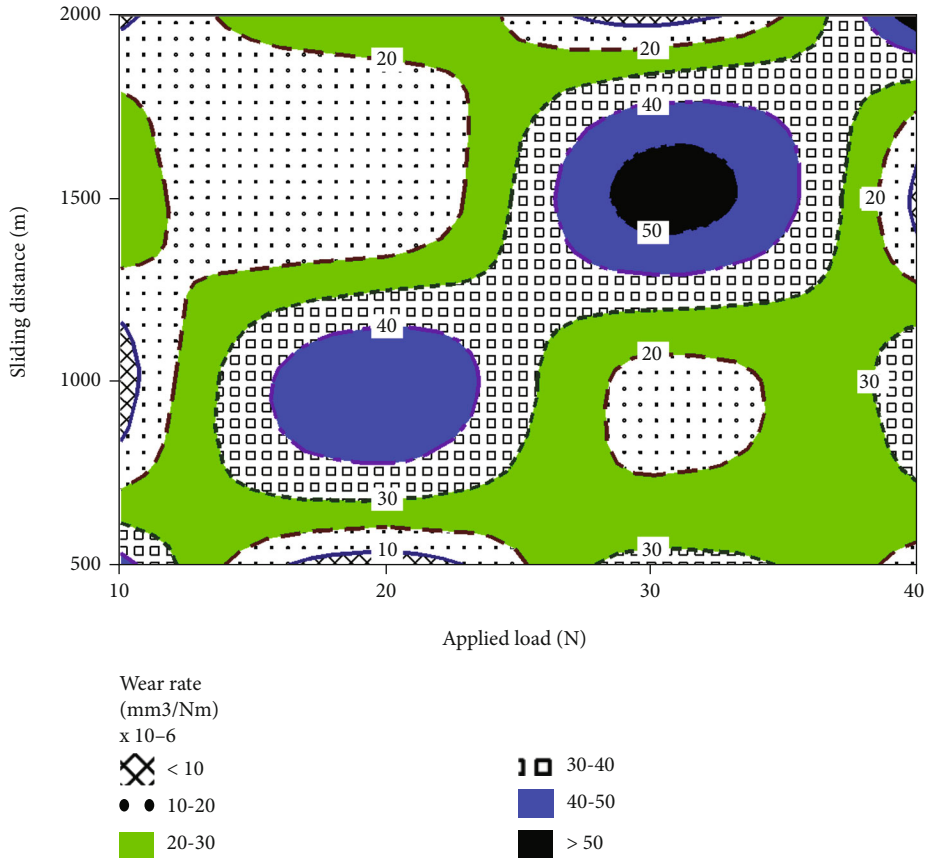

Figure 14: Contour plot showing wear rate with the combined effect of applied load and sliding distance.

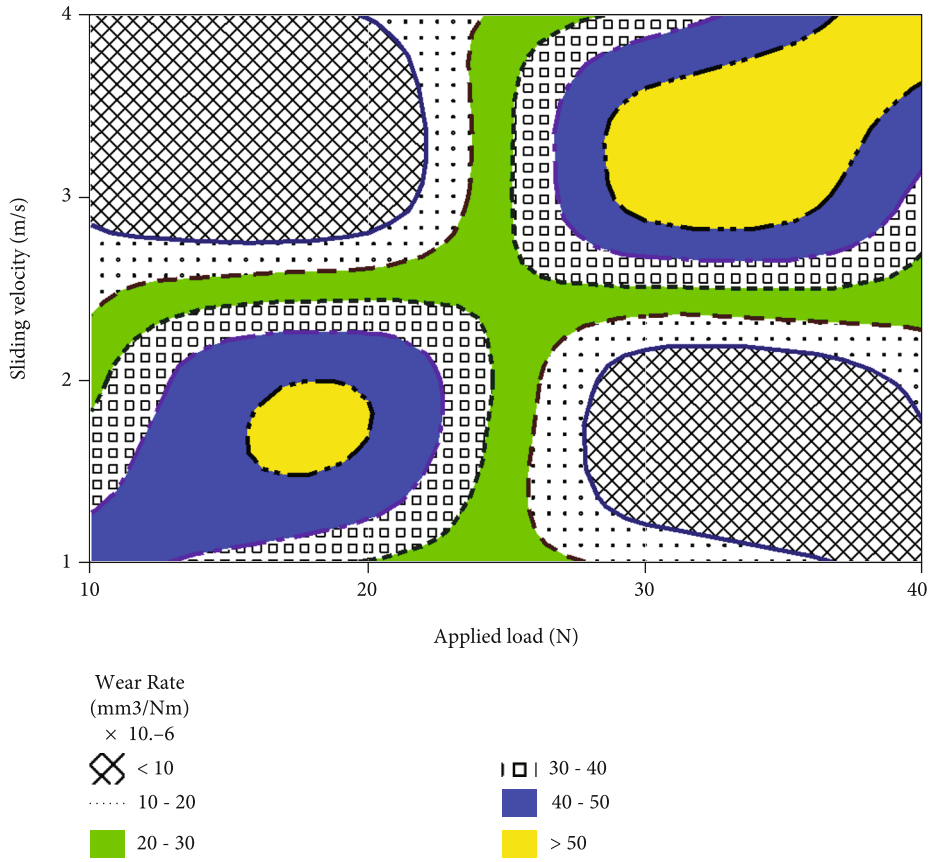

Figure 15: Contour plot showing wear rate with the combined effect of applied load and sliding velocity.

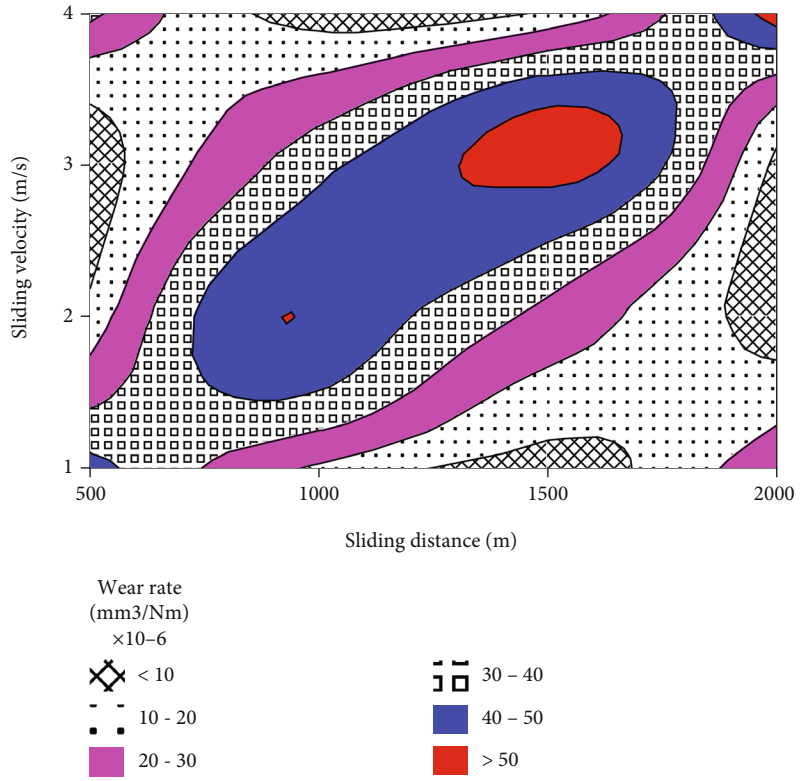

Figure 16: Contour plot showing wear rate with the combined effect of sliding distance and sliding velocity.

Table 6: Analysis of variance for wear rate (mm^3/Nm) $\times 10^{-6}$.

Source	DF	Seq SS	Adj SS	Adj MS	*F*-value	*P* value	% contribution
Weight percentage of MWCNT	3	5127.84	5127.84	1709.28	305.89	≤0.001	95.97
Applied load (N)	3	160.25	160.25	53.42	9.56	0.048	2.99
Sliding velocity (m/s)	3	19.15	19.15	6.38	1.14	0.458	0.35
Sliding distance (m)	3	19.14	19.14	6.38	1.14	0.458	0.35
Error	3	16.76	16.76	5.59			
Total	15	5343.14					

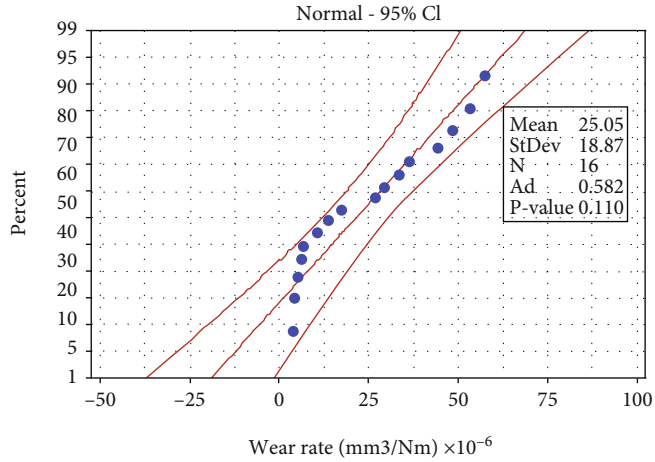

Figure 17: Probability plot.

2 m/s sliding velocity, and 500 m sliding distance. The similar results were observed for the researcher [2]. The rise in sliding and sliding speed rises the temperature amid the counterparts and therefore successfully improves wear rate. An augmentation in the value of applied load contact amid disc and pin rises causes the wear rate to get prominent [37].

The interaction effect generated from various combinations of input parameters and the effect imposed on the wear rate was as illustrated in the interaction plot in Figure 10. The parallel lines perceived in the frontline plots reveal that no interaction effect was caused by the wt% of MWCNT when linked with the other three parameters. Under all cases, the composite with 12 wt% MWNCT gained the minimum wear rate. The wear rate gets elevated because of the hike in applied load, and this may be attributed to the perfect contact and in turn the friction between the counterparts encountered at high loads. Also, the plastic deformation was configured due to the existence of friction-induced high temperature contributed to the increase in wear loss.

Though the sliding distance was drawn out to be the least significant factor, the spike in sliding distance increases the wear rate initially, then suddenly experiences a drop-in wear rate, and resumes the increasing trend. This behavior can be well explained by correlating with the oxide layer formation. An increase in sliding distance will bring out more heat between the mating parts, and this aids in oxide layer formation that inhibits the wear loss. For a further increase in sliding distance, due to high temperature, the mating surfaces become softer and the oxide layer deteriorates causing the wear rate to get increased again. The cross-linked patterns observed in the interaction plots that portray the combined effect of applied load, sliding distance, and sliding velocity revealed the presence of interaction effect between the aforesaid parameters. The contour plots in Figures 11–13 explain the combined effect caused by the weight percentage of MWCNT when interacted with load, sliding velocity, and sliding distance. In all the three plots, lower wear rate region was observed in the zone with 12 wt% MWCNT and the pure copper contributes to the high wear rate region. The *y*-axis parameters remain ineffective and failed to cause the combined effect. The scattered low wear rate region in Figures 14–16 confirms the presence of interaction effect between the respective parameters.

3.7. ANOVA Analysis of Wear Rate. Through ANOVA (Table 6), by conducting *F*-test and identifying the maximum *F*-value, the most influencing parameter can be ascertained. The weight percentage scored a maximum *F*-value of 305.89 and succeeded to be the most influencing parameter. The parameters sliding velocity and sliding distance were proven progressive inclusion of MWCNT reinforcement to be the least significant with 1.14 as the *F*-value.

The probability plot in Figure 17 confirmed that the process pursued a normal distribution and also verified the absence of outliers. These observations inferred that the model proposed for wear study was executed satisfactorily.

4. Conclusions

Cu-MWCNT composites were successfully produced via powder metallurgy route, and the impact made by MWCNT on the behaviours of the composite was studied. The physical and mechanical properties of the Cu-MWCNT composites were evaluated and by performing Taguchi analysis, the effect of wear test parameters and the optimized conditions to accomplish minimum wear rate were identified. From the results of the current investigation, the following conclusions were made:

(i) The SEM micrographs of the milled composite powders confirm even dispersal of the composite constituents and proved 6 hours of milling to be an effective and optimum milling time to achieve the aforesaid condition

(ii) The existence of Cu and MWCNT particles in the composite powders formed was confirmed by EDAX analysis

(iii) Relative density values show the occurrence of agglomerated MWCNT with higher reinforcement addition

(iv) The hardness and compressive strength of the composites were superior over pure copper matrix, and the highest values were attained in the composites with the addition of 12 wt% of MWCNT

(v) The MWCNT addition was limited to 4 wt%, and while increasing further up to 12 wt%, the thermal conductivity of the composites was found to get declined due to cluster formation

(vi) The pure copper exhibits the maximum wear rate, and the MWCNT reinforcement weight content was identified as the most significant parameter

(vii) The optimized parameter levels that contribute minimum wear rate were identified as 12% MWCNT content, 10 N applied load, 2 m/s sliding velocity, and 500 m sliding distance

Data Availability

The data used to support the findings of this study are included in the article.

Conflicts of Interest

The authors declare that there is no conflict of interest regarding the publication of this article.

References

[1] M. T. Alam, A. H. Ansari, S. Arif, and M. N. Alam, "Mechanical properties and morphology of aluminium metal matrix nanocomposites-stir cast products," *Advances in Materials and Processing Technologies*, vol. 3, no. 4, pp. 600–615, 2017.

[2] B. Stalin, M. Ravichandran, G. T. Sudha et al., "Effect of titanium diboride ceramic particles on mechanical and wear behaviour of Cu-10 wt% W alloy composites processed by P/M route," *Vacuum*, vol. 184, article 109895, 2021.

[3] Y. Liu, F. Wang, Y. Cao et al., "Unique defect evolution during the plastic deformation of a metal matrix composite," *Scripta Materialia*, vol. 162, pp. 316–320, 2019.

[4] M. T. Alam, S. Arif, A. H. Ansari, and M. N. Alam, "Optimization of wear behaviour using Taguchi and ANN of fabricated aluminium matrix nanocomposites by two-step stir casting," *Materials Research Express*, vol. 6, no. 6, article 065002, 2019.

[5] X. Gao, H. Yue, E. Guo et al., "Tribological properties of copper matrix composites reinforced with homogeneously dispersed graphene nanosheets," *Journal of Materials Science & Technology*, vol. 34, no. 10, pp. 1925–1931, 2018.

[6] T. Zuo, J. Li, Z. Gao et al., "Simultaneous improvement of electrical conductivity and mechanical property of Cr doped Cu/CNTs composites," *Materials Today Communications*, vol. 23, article 100907, 2020.

[7] K. R. Ramkumar, S. Ilangovan, S. Sivasankaran, and A. S. Alaboodi, "Experimental investigation on synthesis and structural characterization of Cu- Zn-x wt%Al_2O_3 (x = 0, 3, 6, 9 & 12%) nanocomposites powders through mechanical alloying," *Journal of Alloys and Compounds*, vol. 688, pp. 518–526, 2016.

[8] S. D. Kumar, M. Ravichandran, A. Jeevika, B. Stalin, C. Kailasanathan, and A. Karthick, "Effect of ZrB_2 on microstructural, mechanical and corrosion behaviour of aluminium (AA7178) alloy matrix composite prepared by the stir casting route," *Ceramics International*, vol. 47, no. 9, pp. 12951–12962, 2021.

[9] S. Sebastin, A. K. Priya, A. Karthick, R. Sathyamurthy, and A. Ghosh, "Agro waste sugarcane bagasse as a cementitious material for reactive powder concrete," *Clean Technologies*, vol. 2, no. 4, pp. 476–491, 2020.

[10] E. Karakulak, "Characterization of Cu–Ti powder metallurgical materials," *International Journal of Minerals, Metallurgy, and Materials*, vol. 24, no. 1, pp. 83–90, 2017.

[11] K. J. Joshua, S. J. Vijay, and D. P. Selvaraj, "Effect of nano TiO_2 particles on microhardness and microstructural behavior of AA7068 metal matrix composites," *Ceramics International*, vol. 44, no. 17, pp. 20774–20781, 2018.

[12] S. Liang, W. Li, Y. Jiang, F. Cao, G. Dong, and P. Xiao, "Microstructures and properties of hybrid copper matrix composites reinforced by TiB whiskers and TiB_2 particles," *Journal of Alloys and Compounds*, vol. 797, pp. 589–594, 2019.

[13] R. G. Chandrakanth, K. Rajkumar, and S. Aravindan, "Fabrication of copper–TiC–graphite hybrid metal matrix composites through microwave processing," *The International Journal of Advanced Manufacturing Technology*, vol. 48, no. 5-8, pp. 645–653, 2010.

[14] K. R. Ramkumar, S. Sivasankaran, and A. S. Alaboodi, "Effect of alumina content on microstructures, mechanical, wear and machining behavior of Cu-10Zn nanocomposite prepared by mechanical alloying and hot- pressing," *Journal of Alloys and Compounds*, vol. 709, pp. 129–141, 2017.

[15] D. Jeyasimman, K. Sivaprasad, S. Sivasankaran, and R. Narayanasamy, "Fabrication and consolidation behavior of Al 6061 nanocomposite powders reinforced by multi-walled carbon nanotubes," *Powder Technology*, vol. 258, pp. 189–197, 2014.

[16] V. Kavimani, B. Stalin, P. M. Gopal, M. Ravichandran, A. Karthick, and M. Bharani, "Application of r-GO-MMT hybrid nanofillers for improving strength and flame retardancy of epoxy/glass fibre composites," *Advances in Polymer Technology*, vol. 2021, Article ID 6627743, 9 pages, 2021.

[17] S. M. Uddin, T. Mahmud, C. Wolf et al., "Effect of size and shape of metal particles to improve hardness and electrical properties of carbon nanotube reinforced copper and copper alloy composites," *Composites Science and Technology*, vol. 70, no. 16, pp. 2253–2257, 2010.

[18] S. K. Soni, B. Thomas, and V. R. Kar, "A comprehensive review on CNTs and CNT-reinforced composites: syntheses, characteristics and applications," *Materials Today Communications*, vol. 25, article 101546, 2020.

[19] R. Naveenkumar, M. Ravichandran, B. Stalin et al., "Comprehensive review on various parameters that influence the performance of parabolic trough collector," *Environmental Science and Pollution Research*, vol. 28, no. 18, article 13439, pp. 22310–22333, 2021.

[20] W. D. Wong-Ángel, L. Téllez-Jurado, J. F. Chávez-Alcalá, E. Chavira-Martínez, and V. F. Verduzco-Cedeño, "Effect of copper on the mechanical properties of alloys formed by powder metallurgy," *Materials & Design*, vol. 58, pp. 12–18, 2014.

[21] X. Li, G. Ma, P. Jin, L. Zhao, J. Wang, and S. Li, "Microstructure and mechanical properties of the ultra-fine grained ZK60 reinforced with low content of nano-diamond by powder metallurgy," *Journal of Alloys and Compound*, vol. 778, pp. 309–317, 2018.

[22] K. Yoganandam, V. Shanmugam, A. Vasudevan et al., "Investigation of dynamic, mechanical, and thermal properties of *Calotropis procera* particle-reinforced PLA biocomposites," *Advances in Materials Science and Engineering*, vol. 2021, Article ID 2491489, 7 pages, 2021.

[23] L. Liu, R. Bao, J. Yi, and D. Fang, "Fabrication of CNT/Cu composites with enhanced strength and ductility by SP combined with optimized SPS method," *Journal of Alloys and Compounds*, vol. 747, pp. 91–99, 2018.

[24] H. Wang, Z. H. Zhang, Z. Y. Hu et al., "Improvement of interfacial interaction and mechanical properties in copper matrix composites reinforced with copper coated carbon nanotubes," *Materials Science Engineering A*, vol. 715, pp. 163–173, 2018.

[25] P. Yang, X. You, J. Yi et al., "Simultaneous achievement of high strength, excellent ductility, and good electrical conductivity in carbon nanotube/copper composites," *Journal of Alloys and Compounds*, vol. 752, pp. 431–439, 2018.

[26] M. T. Alam, S. Arif, and A. H. Ansari, "Wear behaviour and morphology of stir cast aluminium/SiC nanocomposites," *Materials Research Express*, vol. 5, no. 4, article 045008, pp. 1–24, 2018.

[27] M. R. Akbarpour, S. Alipour, M. Farvizi, and H. S. Kim, "Mechanical, tribological and electrical properties of Cu-CNT composites fabricated by flake powder metallurgy method," *Archives of Civil and Mechanical Engineering*, vol. 19, no. 3, pp. 694–706, 2019.

[28] C.-W. Nan and R. Birringer, "Determining the Kapitza resistance and the thermal conductivity of polycrystals: a simple model," *Physical Review B*, vol. 57, no. 14, pp. 8264–8268, 1998.

[29] S. Sivasankaran, K. Sivaprasad, R. Narayanasamy, and V. K. Iyer, "Synthesis, structure and sinter- ability of 6061 AA100 –x–xwt.% TiO_2 composites prepared by high-energy ball milling," *Journal of Alloys and Compounds*, vol. 491, no. 1-2, pp. 712–721, 2010.

[30] A. K. Shukla, N. Nayan, S. V. S. N. Murty et al., "Processing of copper-carbon nanotube composites by vacuum hot pressing technique," *Materials Science and Engineering: A*, vol. 560, pp. 365–371, 2013.

[31] V. M. Kumar and C. V. Venkatesh, "Evaluation of microstructure, physical and mechanical properties of Al 7079–AlN metal matrix composites," *Materials Research Express*, vol. 6, no. 12, article 126503, 2019.

[32] M. P. Reddy, R. A. Shakoor, G. Parande et al., "Enhanced performance of nano-sized SiC reinforced Al metal matrix nanocomposites synthesized through microwave sintering and hot extrusion techniques," *Progress in Natural Science: Materials International*, vol. 27, no. 5, pp. 606–614, 2017.

[33] P. R. Matli, U. Fareeha, R. A. Shakoor, and A. M. A. Mohamed, "A comparative study of structural and mechanical properties of Al-Cu composites prepared by vacuum and microwave sintering techniques," *Journal of Materials Research and Technology*, vol. 7, no. 2, pp. 165–172, 2018.

[34] P. Zhang, J. Jie, Y. Gao et al., "Preparation and properties of TiB_2 particles reinforced Cu-Cr matrix composite," *Materials Science and Engineering: A*, vol. 642, pp. 398–405, 2015.

[35] J. H. Nie, C. C. Jia, X. Jia, Y. Li, Y. F. Zhang, and X. B. Liang, "Fabrication and thermal conductivity of copper matrix composites reinforced by tungsten-coated carbon nanotubes," *International Journal of Minerals, Metallurgy and Materials*, vol. 19, no. 5, pp. 446–452, 2012.

[36] S. Arivukkarasan, V. Dhanalakshmi, B. Stalin, and M. Ravichandran, "Mechanical and tribological behaviour of tungsten carbide (WC) reinforced aluminium LM4 matrix composites," *Particulate Science and Technology*, vol. 36, pp. 967–973, 2018.

[37] C. Zou, Z. Chen, H. Kang et al., "Study of enhanced dry sliding wear behavior and mechanical properties of Cu- TiB_2 composites fabricated by in situ casting process," *Wear*, vol. 392-393, pp. 118–125, 2017.

Hindawi
Journal of Nanomaterials
Volume 2021, Article ID 1828147, 11 pages
https://doi.org/10.1155/2021/1828147

Research Article

Preparation and Characterization of Lauric–Myristic Acid/Expanded Graphite as Composite Phase Change Energy Storage Material

Dongyi Zhou,[1,2,3] **Jiawei Yuan**,[1,3] **Xianghua Xiao**,[1,3] **and Yicai Liu**[2]

[1]*School of Mechanical and Energy Engineering, Shaoyang University, Shaoyang 422000, China*
[2]*School of Energy Science and Engineering, Central South University, Changsha 410083, China*
[3]*Key Laboratory of Hunan Province for Efficient Power System and Intelligent Manufacturing, Shaoyang University, Shaoyang 422000, China*

Correspondence should be addressed to Dongyi Zhou; zhoudongyi2005@163.com and Yicai Liu; lyc0300@163.com

Received 12 April 2021; Revised 12 May 2021; Accepted 28 May 2021; Published 17 June 2021

Academic Editor: Sami-Ullah Rather

Lauric acid (LA) and myristic acid (MA) were used to prepare a binary eutectic mixture. The expanded graphite (EG) was used as the carrier, and the lauric–myristic acid/expanded graphite (LA–MA/EG) composite phase change material was prepared by physical adsorption method. The microstructure, chemical structure, and thermal properties of LA–MA/EG were characterized by scanning electron microscopy (SEM), differential scanning calorimeter (DSC), Fourier transform infrared spectroscopy (FTIR), and thermal conductivity measurement. The experimental results have shown that the maximum mass ratio of the binary eutectic mixture in the LA–MA/EG composite phase change energy-storing material was 92.2%, and there was physical mixing and has no chemical reaction between LA–MA and EG. The fusion point temperature of LA–MA/EG was 33.4°C, the solidification point temperature was 33.8°C, and the latent heat was 171.1 J/g, which was suitable for building energy storage field. After several thermal cycles, the change of the fusion point and potential heat of the composite phase change materials were very small, and it still has good energy storage performance.

1. Introduction

Because of the growing energy shortage in today's society, it is particularly important to improve the effective utilization of traditional energy gradually; the development and application of new energy resources such as solar energy are also significant. Thermal energy storage (TES) has become a wide development prospect technology in order to improve the utilization rate of renewable energy [1–3]. In general, according to the different heat storage mechanisms, TES technology is divided into sensible heat energy storage technology, latent heat energy storage technology, and chemical reaction energy storage technology [4]. The chemical reaction energy storage technology can release heat energy through the endothermic and exothermic processes of chemical reactions [5], and due to the high cost of equipment, complex operation process, and the risk of chemical hazards, it is not applicable to the field of building energy conservation. Sensible heat storage technology can store and release heat energy by changing the temperature of thermal insulation materials [6], and the technology was relatively mature but the storage density was low. Latent heat energy storage technology utilizes the characteristics of heat energy release and absorption of PCMs during the transition between solid phase and liquid phase [7, 8], to achieve the goal of energy storage, temperature control, and energy recovery and reuse and balance the contradiction between energy supply and demand [9]. It has the advantages of high potential heat of phase transition, high energy storage density, and stable temperature output and has a broad application prospect in many fields such as building energy conservation [10, 11], solar energy utilization [12–14], recycling and utilization of industrial

Table 1: Heat performances of some phase change materials (PCMs) and composite phase change materials (CPCMs). CA: capric acid; LA: lauric acid; MA: myristic acid; PA: palmitic acid; SA: stearic acid; EG: expanded graphite.

PCMs/CPCMs	Melting		Freezing		Reference
	Temperature (°C)	Latent heat (J/g)	Temperature (°C)	Latent heat (J/g)	
PA–SA	54.81	187.0	54.06	179.7	[39]
PA–SA/EG	55.18	176.2	54.91	175.6	
MA–PA–SA	41.72	163.5	42.38	159.8	[40]
MA–PA–SA/EG	41.64	153.5	42.99	151.4	
CA–MA–PA	18.98	135.6	17.26	131.9	[41]
CA–MA–PA/EG	18.61	128.2	16.58	124.5	
LA–SA	35.54	159.9	34.36	/	[42]
LA–SA/EG	35.69	143.4	34.28	/	
LA–MA	33.90	176.9	32.6	154.1	This study
LA–MA/EG	33.4	171.1	33.8	152.3	

exhaust heat [15], food storage [16], the balance of the electric power, and military infrared camouflage, getting more and more extensive attention.

Phase change materials (PCMs) can supply a large heat capacity with a limited range of temperatures, and the phase change process was isothermal. Phase change materials used in construction must meet its phase transition temperature were within the scope of the indoor temperature, latent heat of large, stable chemical performance, not leak and metamorphism, etc. [17, 18]. According to the phase state, phase change materials can be divided into solid–solid phase change materials [19], solid–liquid phase change material [20], solid–gas phase change material, and liquid–gas phase change material. According to their chemical composition, they can be divided into organic phase change materials [21] and inorganic phase change materials [22]; organic phase change materials are divided into the paraffin [23] and nonparaffin; subdivided, nonparaffin phase change materials include alcohols [24], lipids, diols, and fatty acids, and different kinds of phase change materials have certain limitations in their application. As a kind of common organic PCM, fatty acids are cheap and easy to obtain. Due to their high latent heat of phase change, stable performance [25, 26], and different melting temperatures, fatty acids can adapt to different climatic conditions and be widely used in the research and application of building energy conservation.

Although fatty acids have many advantages, they still have the negative characteristics of poor thermal conductivity and easy leakage of pure phase change materials [27]. To resolve this problem, high thermal conductivity materials can be added into fatty acid PCM to prepare composite phase change materials. Not only can composite phase change materials be improved in terms of thermal conductivity, but they can also be made into stable PCMs which are not as likely to leak. The commonly used base materials for preparing shaped phase change materials include expanded graphite [28, 29], expanded perlite [30], diatomite [31], and activated carbon. The commonly used preparation methods of composite phase change materials include the microcapsule method [32], sol–gel method [33], solution–melt infiltration method, and physical adsorption method [34].

Zhang et al. studied a composite phase change material (CPCM) of capric acid, palmitic acid, and stearic acid ternary eutectic mixture/expanded graphite (CA–PA–SA/EG) used for low-temperature heat storage. CA–PA–SA/EG composite phase change material was a kind of promising energy storage material at low temperature, and the melting and freezing temperatures were 21.33°C and 19.01°C, severally. And the latent heat of CA–PA–SA/EG was 131.7 J/g and 127.2 J/g, respectively. CA–PA–SA/EG composite PCMs were dry and easy to be pressed, and thermal conductivity was much higher than the ternary eutectic mixture of CA–PA–SA. The thermal performance test has shown that with the increase of thermal conductivity of CA–PA–SA, the melting/cooling time was obviously shortened. After 500 times thermal cycling test, the result indicated that CA–PA–SA/EG composite phase change material has good thermal reliability [35]. Many studies have shown that adding the expanded graphite can not only prevent the leakage occurred in the molten state of PCMs but also extremely strengthen the thermoconductivity of CPCMs and enhance the thermal performance [36–38]. The thermal properties of some PCM and composite PCM were shown in Table 1.

LA and MA as PCMs applied in the fields of low-temperature thermal storage, such as building heating/cooling and indoor temperature controlling, represent higher phase change temperatures. In this paper, the phase transition temperature and potential thermal of the prepared LA–MA/EG were 33.9°C and 176.9 J/g, severally, and it can be extensively used in low-temperature energy storage areas. The LA–MA/EG composite PCM was prepared by the physical adsorption method. The scanning electron microscopy (SEM) measurement was used for the LA–MA/EG microstructure; Fourier transform infrared spectroscopy (FTIR) tests the material structure and determines the combination between LA–MA binary eutectic mixture and EG; the CPCM phase transition point and phase change latent heat were determined by differential scanning calorimeter (DSC); the CPCM thermal stability was determined by thermogravimetric analysis (TGA); the change of the change phase point and latent heat of CPCMs after multiple phase transformation were determined by thermal cycle test; the thermal storage

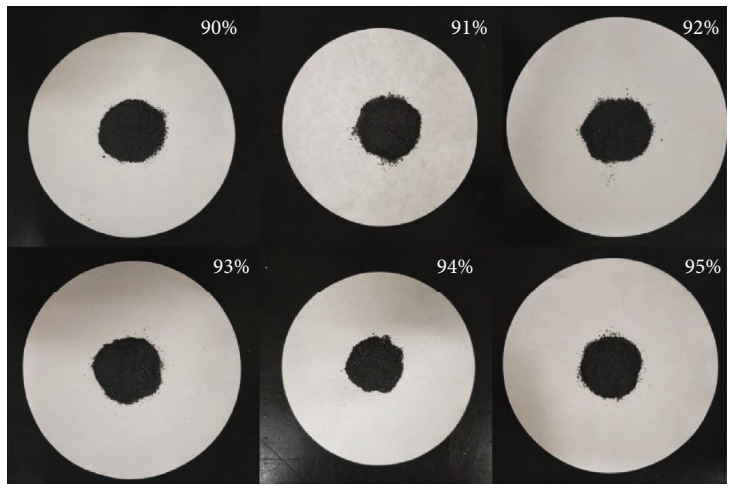

(a)

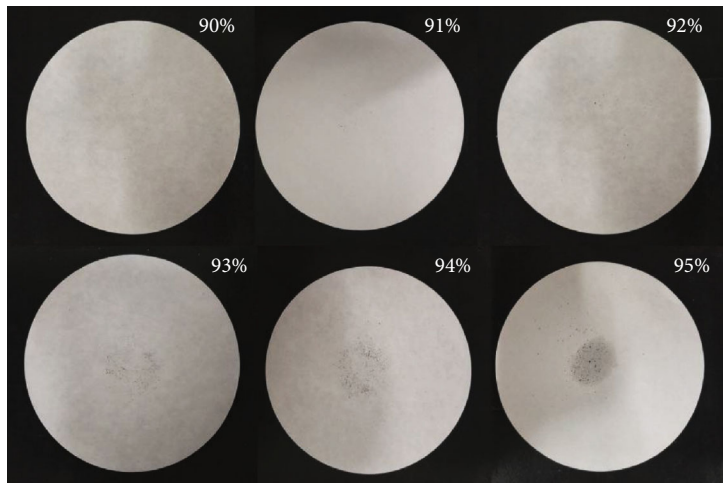

(b)

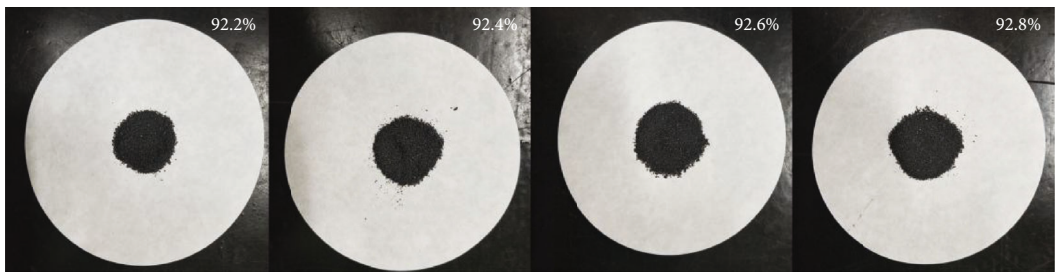

(c)

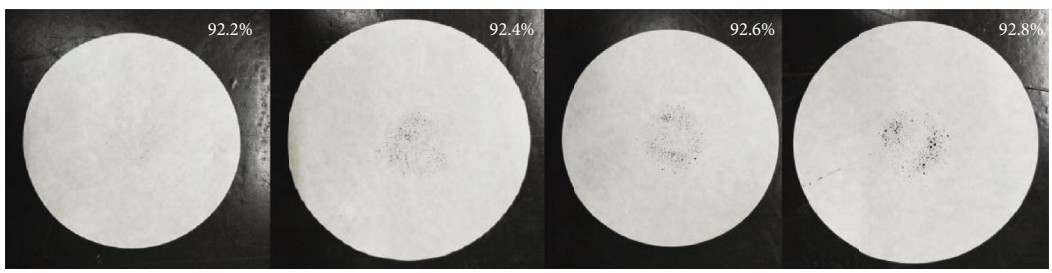

(d)

Figure 1: The LA–MA/EG CPCM samples before and after heat treatment. (a) The first set of specimens after heat treatment; (b) the first set of filter papers with specimens brushed off after thermal treatment; (c) the second set of specimens after heat treatment; (d) the leakage of the second set of filter papers with specimens brushed off after thermal treatment.

and release capacity of CPCM was tested by heat storage and release experiment. Finally, the coefficient of heat conductivity of CPCM was measured by the thermal flow method.

2. Experiments

2.1. Materials. Lauric acid (LA, $C_{12}H_{24}O_2$, analytical pure) was purchased from Shanghai Eppie Chemical Reagent Co., Ltd.; myristic acid (MA, $C_{14}H_{28}O_2$, the 98% pure) was purchased from Shanghai Zhanyun Chemical Co., Ltd. Expansible graphite (particle size 80 mesh, expansion rate 350 mL/g, carbon content 99%, and density 1.1 g/cm^3) was purchased from Qingdao Forest Graphite Products Co., Ltd., China.

2.2. LA–MA/EG CPCM Preparation. Take different content of LA and MA into the beakers, respectively, and heat them in a water bath with the temperature at 60°C. After the fatty acids were fully dissolved, use the constant temperature magnetic stirrer to fully blend LA–MA, with a rotating speed of 500 r for 30 min, and then cool the mixture to room temperature.

Put an amount of expandable graphite into the beaker, seal the beaker with the thin film, and dry in a vacuum drying oven. Then, the expandable graphite after drying is heated at high temperature in a Muffle furnace. The expansion temperature is set as 900°C, and the expansion time is 30–50 s; finally, the expandable graphite can be obtained.

The eutectic mixture of LA–MA and EG was placed in the same beaker and stirred evenly with a glass rod. The thin film sealed beaker was used; then, the eutectic mixture was placed into a vacuum drying oven with temperature 50°C for 48 h and stirred evenly every 2 h, to ensure that the PCM was uniform adsorption in the pores of EG. After cooling the sample to room temperature, the LA–MA/EG composite PCM was obtained.

2.3. Characterization. The differential scanning calorimeter (DSC; DSC instrument, STA2500, Germany) was used to measure the LA–MA/EG composite PC, and the phase transition temperature and phase change potential heat of LA–MA/EG before and after the thermal cycle. Under a nitrogen atmosphere of 0.5 bar, the samples with a mass of 5–10 mg were encapsulated in an aluminum crucible, the temperature range was set to 0–100°C, and the temperature and the heat measurement accuracy was ±2.0%. In order to remove the sample thermal history, ignore the first heating cycle. The heating and cooling ratio was set to 10°C/min. After the test, a temperature–heat flow curve of the samples can be received. The phase transition temperature and phase transformation potential heat of the samples were obtained by the DSC analysis software.

The FTIR (FTIR instrument, Thermo Scientific Nicolet iS5, USA) was used to analyze the chemical structure of the LA–MA/EG composite PCM. Turn on the FTIR under the condition of suitable indoor temperature and stable voltage. After the background collection and testing, the LA–MA binary eutectic mixture and the LA–MA/EG composite PCM samples were put into the samples for testing, respectively, with a testing resolution of 4 cm^{-1} and a frequency of 4000–400 cm^{-1}. Samples were scanned 16 times.

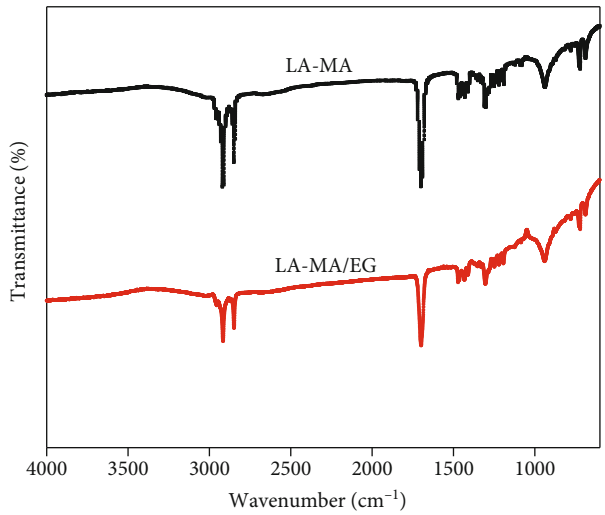

Figure 2: FTIR spectra of LA–MA and LA–MA/EG CPCMs.

Using the scanning electron microscope (SEM, Phenom LE, Phenom-World, Eindhoven, the Netherlands) to observe the LA–MA/EG microstructure, take a small amount of sample placed on the thermal conductive adhesive tape and put into SEM, within the range between 2000x and 6000x, and shot several samples. The LA–MA/EG composite PCMs for the thermal cycle were carried on, after several thermal cycles, repeated to test the thermal properties of the composite phase change materials by DSC. Heat storage and release experiments of LA–MA binary eutectic mixture and LA–MA/EG were carried out with the temperature range between 0 and 50°C, and the multiple intelligent temperature detector (YTJ–1638, Yuyao Yitai Instrument Factory, China) was used to record the temperature variation of the specimen during the whole cycle of thermal storage and release, and the data were recorded every 10 s.

The thermogravimetric analysis technique (TGA, TG 209F3, NETZSCH, Germany) was used to analyze the heat durability and stability of PCMs and CPCMs [43]. Under the nitrogen atmosphere, the weightlessness temperature and weightlessness range of the samples were tested from the room temperature to 500°C at a heating rate of 10°C/min. Finally, the temperature–mass change curve of the samples was obtained by using the analysis software. A thermoconductivity analyzer (DRL-III, Xiangtan Xiangxi Instrument Co., LTD., China) was used to measure the thermoconductivity of PCMs with an accuracy of ±3%.

3. Results and Discussion

3.1. Maximum Mass Ratio of LA–MA in the LA–MA/EG Composite PCMs. Six groups of LA–MA/EG composite PCMs were prepared with sample weight of 5 g and different content of LA–MA (from 90% to 95%), respectively, with uniform distribution in the filter paper center diameter of 30 mm test area. Heat the samples in the vacuum drying oven at 50°C for 30 min, cool to the room temperature and then

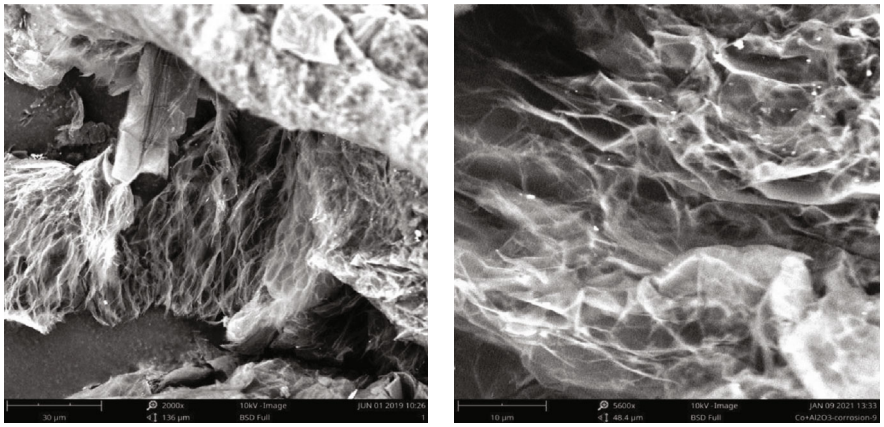

(a) (b)

Figure 3: SEM of (a) EG and (b) LA–MA/EG composite PCMs.

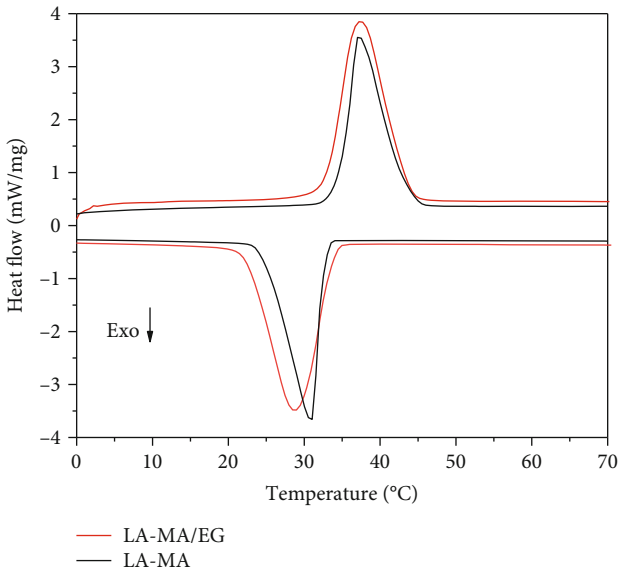

Figure 4: The DSC graphs of LA–MA PCM and LA–MA/EG CPCM.

Table 2: Heat performances of LA–MA PCM and LA–MA/EG CPCM.

PCM	Melting			Freezing		
	Onset temperature (°C)	Peak temperature (°C)	Latent heat (kJ/kg)	Onset temperature (°C)	Peak temperature (°C)	Latent heat (kJ/kg)
LA–MA	33.9	37.2	176.9	32.6	29.8	154.1
LA–MA/EG	33.4	37.4	171.1	33.8	28.7	152.3

brush off the sample, and observe the filter paper permeability, and the results were displayed in Figures 1(a) and 1(b). From Figure 1(a), there were no obvious traces of leakage around the materials of the six groups of samples. After brushing away the samples, observe (Figure 1(b)) that the samples with 94% and 95% LA–MA mass content were completely permeated around the material, which did not meet the conditions of preparation of the best ratio of composite PCMs. The leakage of 90%, 91%, 92%, and 93% samples was not obvious, but compared with other samples, both of the samples with 90% LA–MA mass content and 91% were dryness, pointed out that the proportion of LA–MA in LA–MA/EG was too small, and the latent heat of phase change materials was too low, which does not meet the essential condition of PCM. The sample with 92% LA–MA mass content had no leakage, and the sample with 93%

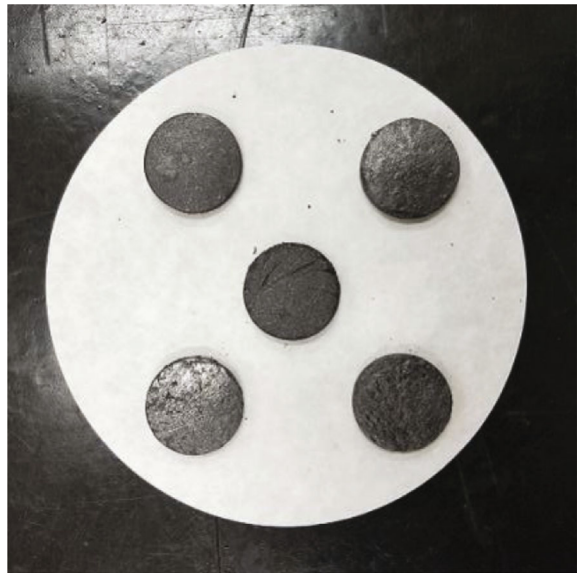

Figure 5: LA-MA/EG CPCM cylinder block with different stacking densities.

Table 3: Parameter of LA–MA/EG CPCMs with different stacking densities.

PCM	Mass (g)	Thickness (mm)	Surface area (mm^2)	Density ($kg{\cdot}m^3$)	Thermal conductivity (W/m·K)
PCM 1	1.9923	4.7	707	600.00	4.225
PCM 2	1.7336	4.8	707	510.84	4.293
PCM 3	1.1888	4.5	707	373.92	2.135
PCM 4	1.7633	5.1	707	489.38	3.430
PCM 5	1.3219	4.6	707	406.75	2.982

LA–MA mass content had some samples adsorbed in the test area, evidenced that the optimal ratio was approximate 92%–93%. The previous experimental steps were repeated and observed. The experimental results were displayed in Figures 1(c) and 1(d). From Figure 1(c), for further identifying the maximum mass ratio, four groups of LA–MA/EG composite PCM samples with 92.2%, 92.4%, 92.6%, and 92.8% LA–MA content were prepared again, and there were no leakages of the binary eutectic mixture solution around the samples. After brushing off the samples, it was observed in Figure 1(d) that the LA–MA mass content of 92.4%, 92.6%, and 92.8% of the samples remained on the filter paper to varying degrees, while the sample with 92.2% LA–MA mass content of the filter paper had no adsorption. Therefore, the maximum mass ratio of the binary eutectic mixture in LA–MA/EG was 92.2%.

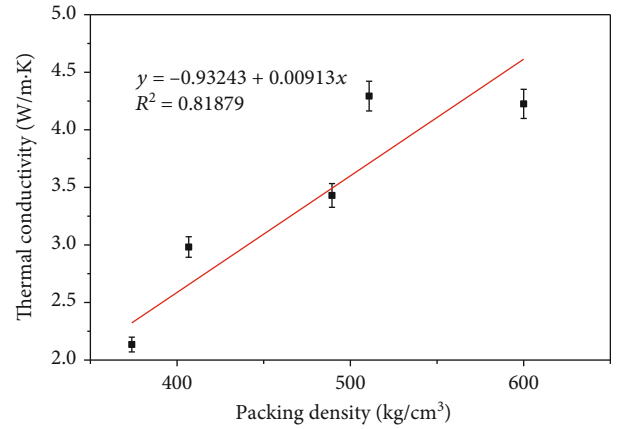

Figure 6: Thermal conductivities change with different stacking densities of LA–MA/EG CPCMs.

3.2. FTIR Analysis of the LA–MA/EG Composite PCMs. Fourier transform infrared spectrometer was used to characterize the chemical construction of the LA–MA binary eutectic mixture and LA–MA/EG. As shown in Figure 2, the absorption peak of C=O stretching vibration appeared in both the two spectral curves at 1689 cm^{-1}, and the absorption peak in the wavenumber range of 2960–2840 cm^{-1} was the stretching vibration absorption peak of hydroxyl O–H, which usually overlaps with C–H stretching vibration absorption peaks of the aliphatic group. It can be seen from Figure 2 that the spectral curves of LA–MA and LA–MA/EG were basically the same, and the position of the characteristic peaks corresponded to one. The results indicated that after adding EG, the LA–MA/EG composite PCMs did not produce new material and had no change in the structure. Between the LA–MA and EG, there was no chemical equation and depends on surface tension and capillary force.

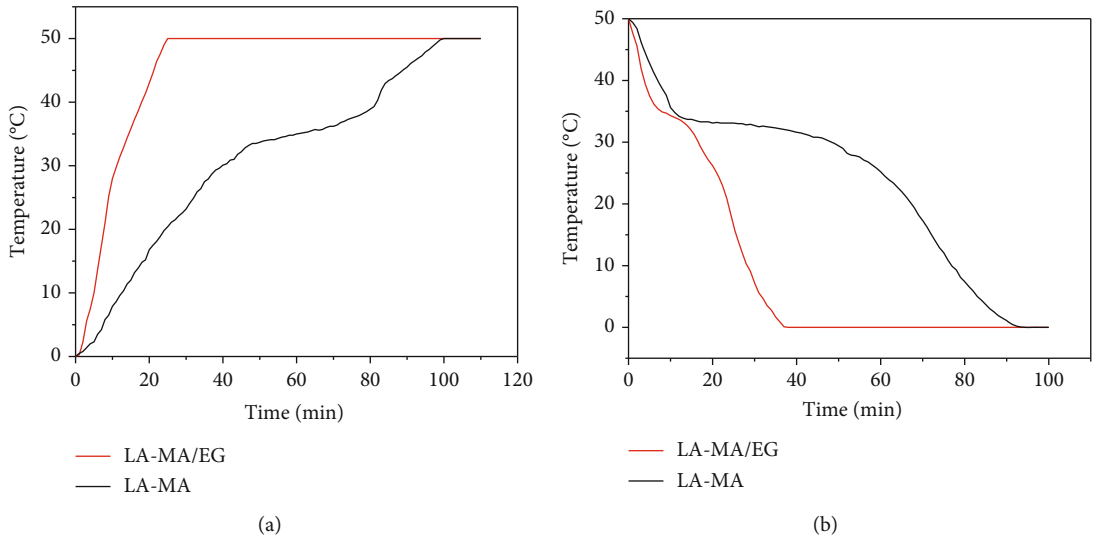

Figure 7: The curves of LA–MA PCM and LA–MA/EG CPCM (a) storage and (b) release heat.

3.3. Microstructure of the LA–MA/EG Composite PCMs. EG and LA–MA/EG composite PCM microstructure diagrams were shown in Figures 3(a) and 3(b), respectively, by SEM. According to Figure 3(a), EG was a network pore structure material, composed with graphite flake and plenty of irregular pores, and the stronger surface tension makes EG adsorb the LA–MA binary eutectic mixture much better. From Figure 3(b), it indicated that the LA–MA has been evenly absorbed in the pore structure of EG. The pores were filled with solution and not easy to leak. The results show that EG has a good adsorption effect, can provide a certain mechanical strength, and prevent leakage as a matrix material.

3.4. Thermal Properties of the LA–MA/EG Composite PCMs. The thermal performance of phase change energy storage materials was measured by DSC; Figure 4 shows the DSC curves of LA–MA and LA–MA/EG, and the thermal performance is shown in Table 2.

Table 2 displays that the fusing point temperature of the LA–MA was 33.9°C, the melting latent thermal was 176.9 J/g, the solidification point temperature was 32.6°C, and the freezing latent thermal was 154.1 J/g. The molten temperature point of LA–MA/EG was 33.4°C, the melting latent heat was 171.1 J/g, the freezing temperature point was 33.8°C, and the freezing latent thermal was 152.3 J/g. By comparison, the melting temperature of LA–MA/EG was marginally lesser than LA–MA, but the solidification temperature was a bit higher than LA–MA, which due to the addition of EG, it enhances the thermal conductivity of the prepared composite PCMs. The high thermoconductivity of the matrix material increases the heat transfer rate of PCMs [44] and leads to a lower phase transition temperature.

3.5. Thermal Conductivity and Heat Storage/Release Behavior of LA–MA/EG Composite PCM. In order to test the relationship between the coefficient of thermal conductivity and different densities of LA–MA/EG composite phase change materials at different bulk densities, in this experiment, 5 cakes of different weights were prepared by using a 3 × 3 cm cake membrane (shown in Figure 5), and then, their thermal conductivity was measured, and the results were displayed in Table 3 and Figure 6. When the packing density of PCMs was 600.00 kg/m^3, 510.84 kg/m^3, 373.93 kg/m^3, 489.38 kg/m^3, and 406.75 kg/m^3, respectively, the thermal conductivity of PCMs was 4.225 W/m·K, 4.293 W/m·K, 2.135 W/m·K, 3.430 W/m·K, and 2.982 W/m·K, respectively. At the sample density between 373.93 and 600.00 kg/m^3, the relationship between the packing density x (kg·m^3) of LA–MA/EG and the thermoconductivity y (W/m·K) was linear through fitting analysis. Formula (1) was obtained by fitting the data in Table 3.

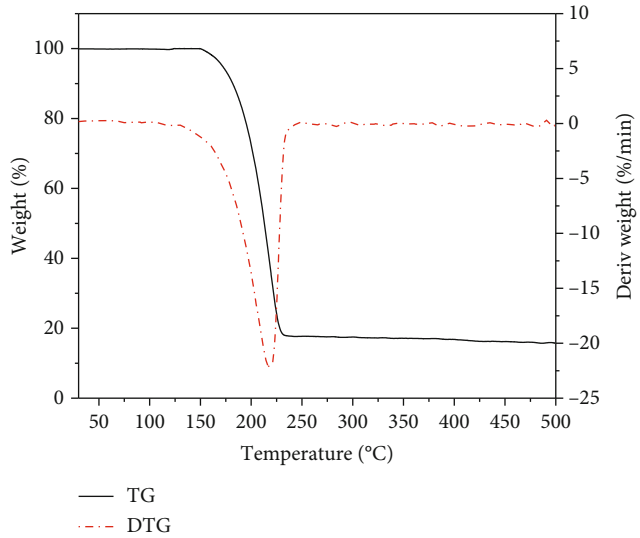

Figure 8: TG and DTG curves of LA–MA/EG CPCMs.

$$y = 0.00913x - 0.93243 \left(R^2 = 0.81879\right). \quad (1)$$

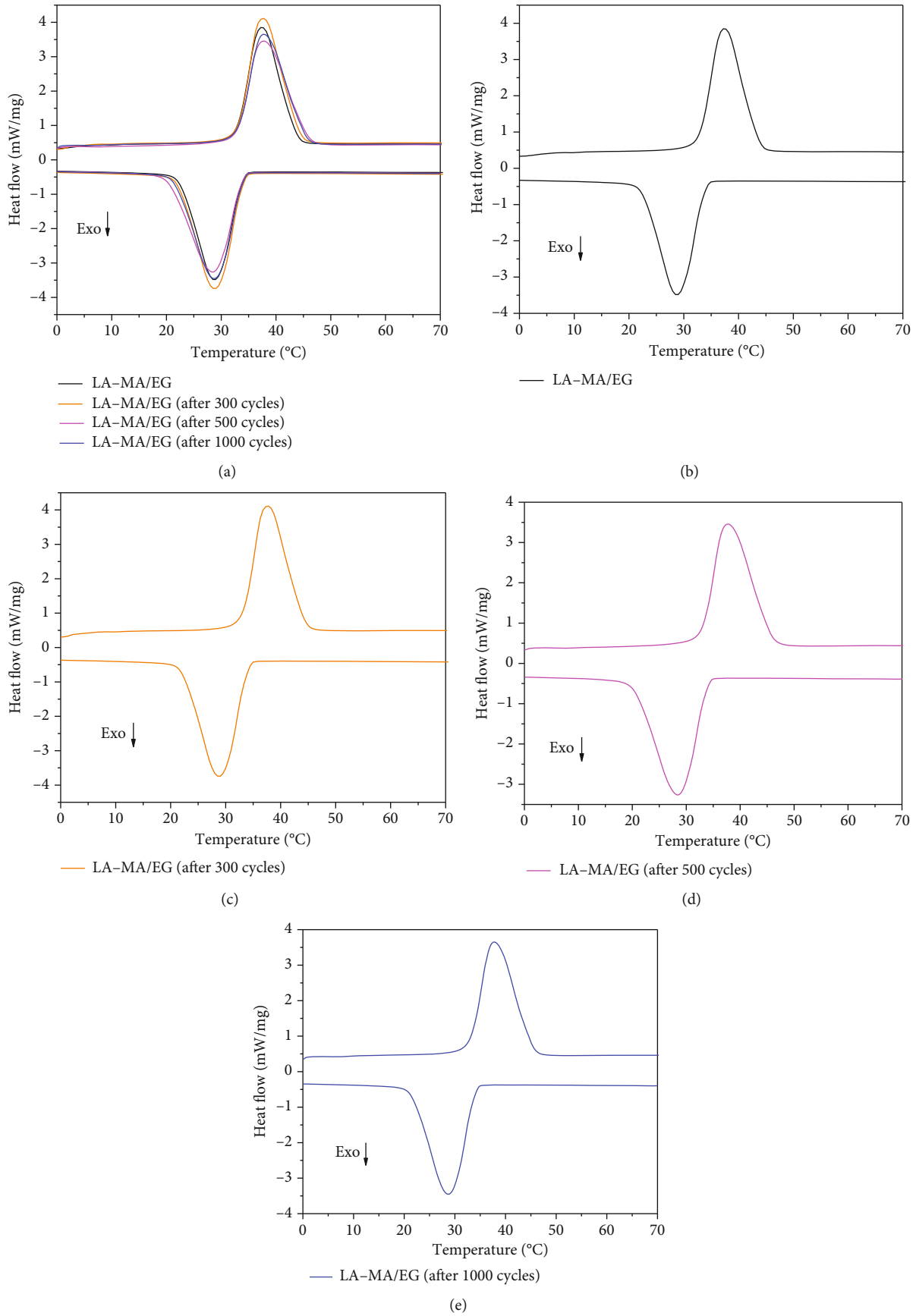

Figure 9: The DSC curves of LA–MA/EG CPCMs before and after thermal cycling.

The temperature probes were placed into the center of the beaker with the same volume of LA–MA and LA–MA/EG, respectively. Then, the beakers were put into the same constant temperature environment, and when the temperature of the materials were stable and reached the set value, begin the test. The temperature setting of the exothermic process was 0°C, and the endothermic process temperature was set as 50°C; the test results are shown in Figure 7. The heat absorption curves of the binary fatty acid and the composite PCM were shown in Figure 7(a), and it was obvious that LA–MA/EG composite PCM takes lesser time to reach the set temperature than LA–MA. The time required for LA–MA/EG heating from 0°C to 50°C was 25 min, while the heating of LA–MA to 50°C was taken 100 min. Figure 7(b) shows the exothermic curve. It only spent 37 min for the exothermic cooling of LA–MA/EG to reach 0°C, while the time required for the exothermic cooling of LA–MA to reach 0°C was 93 min. The results suggested that the thermoconductivity of LA–MA/EG was significantly improved compared with that of LA–MA, indicating that the multipore structure of EG optimized the thermoconductivity of the composite PCMs [45].

3.6. Thermal Stability and Reliability of LA–MA/EG Composite PCM. In terms of phase change materials, whether they still have good thermal stability and no volatilization after thermal cycles, which was to judge whether it can be applied in building energy efficiency standards, in this experiment, the thermal stability of LA–MA/EG was tested by thermogravimetry, and the sample test temperature was set from room temperature to 500°C which heated in a nitrogen atmosphere. The curves are shown in Figure 8. The LA–MA/EG composite phase change material begins to be weightless at the temperature of 150°C, and the residual quality of TG was 15.75%. After the first-order differential of the TG curve, it can be obtained that the maximum weight loss rate of LA–MA/EG reached 22.44%/min when the temperature was 219°C. The results have shown that at temperatures lower than 150°C, even if the fusion temperature of LA–MA was above, the LA–MA in LA–MA/EG would be protected from evaporation. Therefore, LA–MA/EG composite PCM has a capable thermostability in low-temperature utilization.

Thermal reliability is one of the important performance indexes to measure the service life of the CPCMs [46]. In order to test whether the LA–MA/EG still has favorable thermal stability and reliability after multiple thermocyclings, perform the DSC measurement of CPCMs after 300, 500, and 1000 thermal cycles. The DSC curves and heat performance were shown in Figure 9 and Table 4. From Figure 9, after 300, 500, and 1000 thermal cycles, the fusion temperatures of LA–MA/EG composite PCMs were 33.2°C, 33.0°C, and 33.1°C, and the freezing temperature of CPCM was 34.0°C, 33.8°C, and 33.9°C, separately. The latent heat of fusion and solidification of LA–MA/EG composite phase change material before cycling was decreased by 3.04%, 1.05%, 4.9%, 2.37%, 6.8%, and 3.21%, respectively. The phase transition temperature and latent heat of LA–MA/EG composite PCMs were obvious, which indicates that the CPCM has good thermal stability and reliability.

Table 4: Heat performances of LA–MA/EG CPCM.

Number of thermal cycling	Melting temperatures (°C)	Melting latent heat (kJ/kg)	Freezing temperatures (°C)	Freezing latent heat (kJ/kg)
0	33.4	171.1	33.8	152.3
300	33.2	165.9	34.0	150.7
500	33.0	162.7	33.8	148.7
1000	33.1	159.4	33.9	147.4

4. Conclusion

In this paper, the LA–MA binary eutectic mixture as PCM and EG as adsorption material, an LA–MA/EG composite PCM was prepared by physical adsorption method, and its thermal properties were characterized. The results showed that the mixture between the LA–MA and EG was physically blended without chemical reaction. The best mass ratio of LA–MA in LA–MA/EG was 92.2%. The phase transition temperature and potential heat of LA–MA/EG composite phase change materials were 33.4°C and 171.1 J/g, individually. The thermal cycling experiment shows that the thermal properties of LA–MA/EG composite phase change energy storage material would not change greatly after several thermal cycles, which displayed that the composite PCM has excellent thermal reliability. The thermoconductivity of LA–MA/EG was surveyed, which showed that the thermal conductivity of the PCMs was greatly improved due to the porous structure of EG, and the energy storage and release rate of LA–MA/EG were greatly improved. The TG experiment shows that LA–MA/EG has good thermal stability. In conclusion, as a composite PCM with remarkable performance, LA–MA/EG can be extensively used in low-temperature energy storage areas, for instance, solar energy utilization, condenser heat recovery in the household air conditioning, and energy efficiency in building.

Data Availability

The data availability of the manuscript can be found at https://figshare.com/s/8e0057712bcda7642808.

Conflicts of Interest

The authors declare that there are no conflicts of interest.

Acknowledgments

This research was funded by the Key R and D Project of Hunan Provincial (Grant No. 2018GK2074).

References

[1] A. Sarı and A. Karaipekli, "Preparation, thermal properties and thermal reliability of palmitic acid/expanded graphite composite as form-stable PCM for thermal energy storage," *Solar Energy Materials & Solar Cells*, vol. 93, no. 5, pp. 571–576, 2009.

[2] A. F. Regin, S. C. Solanki, and J. S. Saini, "Heat transfer characteristics of thermal energy storage system using PCM capsules: a review," *Renewable and Sustainable Energy Reviews*, vol. 12, no. 9, pp. 2438–2458, 2008.

[3] C. Liu, Y. Song, Z. Xu, J. Zhao, and Z. Rao, "Highly efficient thermal energy storage enabled by a hierarchical structured hypercrosslinked polymer/expanded graphite composite," *International Journal of Heat and Mass Transfer*, vol. 148, p. 119068, 2019.

[4] T. X. Li, J. H. Lee, R. Z. Wang, and Y. T. Kang, "Enhancement of heat transfer for thermal energy storage application using stearic acid nanocomposite with multi-walled carbon nanotubes," *Energy*, vol. 55, pp. 752–761, 2013.

[5] Sheikholeslami and Mohsen, "Numerical simulation for solidification in a LHTESS by means of nano-enhanced PCM," *Journal of the Taiwan Institute of Chemical Engineers*, vol. 86, pp. 25–41, 2018.

[6] Y. Yuan, Y. Yuan, N. Zhang, Y. du, and X. Cao, "Preparation and thermal characterization of capric–myristic–palmitic acid/expanded graphite composite as phase change material for energy storage," *Materials Letters*, vol. 125, pp. 154–157, 2014.

[7] H. Fei, L. Wang, Q. He, W. du, Q. Gu, and Y. Pan, "Preparation and properties of a composite phase change energy storage gypsum board based on capric acid-paraffin/expanded graphite," *ACS Omega*, vol. 6, no. 9, pp. 6144–6152, 2021.

[8] C. Liu, Y. Yuan, N. Zhang, X. Cao, and X. Yang, "A novel PCM of lauric-myristic-stearic acid/expanded graphite composite for thermal energy storage," *Materials Letters*, vol. 120, pp. 43–46, 2014.

[9] B. Yang, J. Liu, Y. Song, N. Wang, and H. Li, "Experimental study on the influence of preparation parameters on strengthening stability of phase change materials (PCMs)," *Renewable Energy*, vol. 146, pp. 1867–1878, 2020.

[10] M. Pomianowski, P. Heiselberg, and Y. Zhang, "Review of thermal energy storage technologies based on PCM application in buildings," *Energy and Buildings*, vol. 67, pp. 56–69, 2013.

[11] F. L. Liu, J. Q. Zhu, J. H. Liu, B. Ma, W. Zhou, and R. Li, "Preparation and properties of capric-stearic acid/White Carbon Black composite for thermal storage in building envelope," *Energy and Buildings*, vol. 158, pp. 1781–1789, 2018.

[12] D. Aydin, S. P. Casey, and S. Riffat, "The latest advancements on thermochemical heat storage systems," *Renewable and Sustainable Energy Reviews*, vol. 41, pp. 356–367, 2015.

[13] A. Shukla, D. Buddhi, and R. L. Sawhney, "Solar water heaters with phase change material thermal energy storage medium: a review," *Renewable and Sustainable Energy Reviews*, vol. 13, no. 8, pp. 2119–2125, 2009.

[14] R. Elarem, T. Alqahtani, S. Mellouli et al., "Numerical study of an Evacuated Tube Solar Collector incorporating a Nano-PCM as a latent heat storage system," *Case Studies in Thermal Engineering*, vol. 24, p. 100859, 2021.

[15] G. Y. Fang, T. Fang, and L. Cao, "Preparation, thermal properties and applications of shape-stabilized thermal energy storage materials," *Renewable and Sustainable Energy Reviews*, vol. 40, pp. 237–259, 2014.

[16] B. Gin and M. M. Farid, "The use of PCM panels to improve storage condition of frozen food," *Journal of Food Engineering*, vol. 100, no. 2, pp. 372–376, 2010.

[17] H. Fei, W. du, Q. J. Gu, L. Wang, Q. He, and Y. Pan, "The Phase Change Characteristics of Capric Acid-based Binary Low Eutectic Mixtures Adsorbed in Expanded Graphite," *Energy and Fuels*, vol. 34, no. 11, pp. 14893–14901, 2020.

[18] Q. H. Yu, F. Tchuenbou-Magaia, B. al-Duri, Z. Zhang, Y. Ding, and Y. Li, "Thermo-mechanical analysis of microcapsules containing phase change materials for cold storage," *Applied Energy*, vol. 211, pp. 1190–1202, 2018.

[19] C. R. Raj, S. Suresh, V. K. Singh, R. R. Bhavsar, M. Chandrasekar, and V. Archita, "Life cycle assessment of nanoalloy enhanced layered perovskite solid-solid phase change material till 10000 thermal cycles for energy storage applications," *Journal of Energy Storage*, vol. 35, p. 102220, 2021.

[20] G. Y. Wang, D. S. Ha, and K. G. Wang, "A scalable environmental thermal energy harvester based on solid/liquid phase-change materials," *Applied Energy*, vol. 250, pp. 1468–1480, 2019.

[21] S. Riffat, "Phase change material developments: a review," *International Journal of Ambient Energy*, vol. 36, no. 3, pp. 102–115, 2015.

[22] A. Wang, M. W. Hu, D. K. Tao, and J. Wang, "Analysis and Application of Phase Change Materials on Energy Saving in Buildings," *Advanced Materials Research*, vol. 411, pp. 523–526, 2011.

[23] N. Şahan and H. Paksoy, "Investigating thermal properties of using nano-tubular Zno powder in paraffin as phase change material composite for thermal energy storage," *Composites Part B: Engineering*, vol. 126, pp. 88–93, 2017.

[24] B. T. Tang, L. J. Wang, Y. J. Xu, J. Xiu, and S. Zhang, "Hexadecanol/phase change polyurethane composite as form-stable phase change material for thermal energy storage," *Solar Energy Materials and Solar Cells*, vol. 144, pp. 1–6, 2016.

[25] A. Sar, "Eutectic mixtures of some fatty acids for latent heat storage: Thermal properties and thermal reliability with respect to thermal cycling," *Energy Conversion and Management*, vol. 47, no. 9-10, pp. 1207–1221, 2006.

[26] L. J. Wang and D. Meng, "Fatty acid eutectic/polymethyl methacrylate composite as form-stable phase change material for thermal energy storage," *Applied Energy*, vol. 87, no. 8, pp. 2660–2665, 2010.

[27] S. F. Wu, T. Yan, Z. H. Kuai, and W. Pan, "Thermal conductivity enhancement on phase change materials for thermal energy storage: A review," *Energy Storage Materials*, vol. 25, pp. 251–295, 2020.

[28] R. S. R. da Silva, S. S. Oishi, E. C. Botelho, and N. G. Ferreira, "Carbon foam composites based on expanded graphite for electrochemical application," *Diamond and Related Materials*, vol. 103, p. 107730, 2020.

[29] Z. G. Zhang, G. Shao, and X. M. Fang, "Study on paraffin/expanded graphite composite phase change thermal energy storage material," *Energy Conversion and Management*, vol. 47, no. 3, pp. 303–310, 2006.

[30] J. H. Jia and L. Zhu, "Influence of the aerogel/expanded perlite composite as thermal insulation aggregate on the cement-based materials: preparation, property, and microstructure," *Construction and Building Materials*, vol. 273, p. 121728, 2021.

[31] X. W. Fu, Z. M. Liu, B. Wu, J. Wang, and J. Lei, "Preparation and thermal properties of stearic acid/diatomite composites as form-stable phase change materials for thermal energy storage via direct impregnation method," *Journal of Thermal Analysis and Calorimetry*, vol. 123, no. 2, pp. 1173–1181, 2016.

[32] T. Y. Wang, S. F. Wang, R. L. Luo, C. Zhu, T. Akiyama, and Z. Zhang, "Microencapsulation of phase change materials with binary cores and calcium carbonate shell for thermal energy storage," *Applied Energy*, vol. 171, pp. 113–119, 2016.

[33] Y. P. Wu and T. Wang, "Preparation and characterization of hydrated salts/silica composite as shape- stabilized phase change material via sol-gel process," *Thermochimica Acta*, vol. 591, pp. 10–15, 2014.

[34] A. Sar, A. Karaipekli, and C. Alkan, "Preparation, characterization and thermal properties of lauric acid/expanded perlite as novel form-stable composite phase change material," *Chemical Engineering Journal*, vol. 155, no. 3, pp. 899–904, 2009.

[35] H. Zhang, X. Gao, C. Chen, T. Xu, Y. Fang, and Z. Zhang, "A capric-palmitic-stearic acid ternary eutectic mixture/expanded graphite composite phase change material for thermal energy storage," *Composites Part A: Applied Science and Manufacturing*, vol. 87, pp. 138–145, 2016.

[36] D. Y. Zhou, J. W. Yuan, Y. H. Zhou, and Y. Liu, "Preparation and Properties of Capric–Myristic Acid/Expanded Graphite Composite Phase Change Materials for Latent Heat Thermal Energy Storage," *Energies*, vol. 13, no. 10, p. 2462, 2020.

[37] X. Huang, Y. D. Cui, B. N. Zhang, G. Q. Yin, and G. Z. Feng, "Preparation and Properties of Capric-Lauric-Palmitic Acid Eutectic Mixtures/Expanded Graphite Composite as Phase Change Materials for Energy Storage," *Advanced Materials Research*, vol. 1028, pp. 40–45, 2014.

[38] J. F. Luo, H. W. Yin, W. Y. Li et al., "Numerical and experimental study on the heat transfer properties of the composite paraffin/expanded graphite phase change material," *International Journal of Heat and Mass Transfer*, vol. 84, pp. 237–244, 2015.

[39] D. Zhou, Y. Zhou, J. Yuan, and Y. Liu, "Palmitic Acid-Stearic Acid/Expanded Graphite as Form-Stable Composite Phase-Change Material for Latent Heat Thermal Energy Storage," *Journal of Nanomaterials*, vol. 2020, 9 pages, 2020.

[40] X. Yang, Y. Yuan, N. Zhang, X. Cao, and C. Liu, "Preparation and properties of myristic-palmitic-stearic acid/expanded graphite composites as phase change materials for energy storage," *Solar Energy*, vol. 99, pp. 259–266, 2014.

[41] Y. Yuan, Y. Yuan, N. Zhang, Y. du, and X. Cao, "Preparation and thermal characterization of capric-myristic-palmitic acid/expanded graphite composite as phase change material for energy storage," *Materials Letters*, vol. 125, no. 1, pp. 154–157, 2014.

[42] H. Zhu, P. Zhang, Z. Meng, and M. Li, "Thermal Characterization of Lauric–Stearic Acid/Expanded Graphite Eutectic Mixture as Phase Change Materials," *Journal of Nanoscience and Nanotechnology*, vol. 15, no. 4, pp. 3288–3294, 2015.

[43] Y. Wang, H. Zheng, H. X. Feng, and D. Y. Zhang, "Effect of preparation methods on the structure and thermal properties of stearic acid/activated montmorillonite phase change materials," *Energy and Buildings*, vol. 47, pp. 467–473, 2012.

[44] M. Li and J. Shi, "Review on micropore grade inorganic porous medium based form stable composite phase change materials: preparation, performance improvement and effects on the properties of cement mortar," *Construction and Building Materials*, vol. 194, pp. 287–310, 2019.

[45] R. A. Mahdi, H. A. Mohammed, K. M. Munisamy, and N. H. Saeid, "Review of convection heat transfer and fluid flow in porous media with nanofluid," *Renewable & Sustainable Energy Reviews*, vol. 41, pp. 715–734, 2015.

[46] Q. Y. Yan, C. Liu, J. Zhang, S. Liu, and X. Sun, "Research on proportion and thermal storage property of the shape stabilized fatty acid," *Journal of Physics Conference Series*, vol. 1074, no. 1, p. 012156, 2018.